**LASER DEMONSTRATION AND PERFORMANCE CHARACTERIZATION OF OPTICALLY PUMPED ALKALI LASER SYSTEMS**

DISSERTATION

Clifford V. Sulham, Major, USAF

AFIT/DS/ENP/10-S06

**DEPARTMENT OF THE AIR FORCE**
**AIR UNIVERSITY**

# AIR FORCE INSTITUTE OF TECHNOLOGY

**Wright-Patterson Air Force Base, Ohio**

APPROVED FOR PUBLIC RELEASE; DISTRIBUTION UNLIMITED

AFIT/DS/ENP/10-S06

LASER DEMONSTRATION AND PERFORMANCE CHARACTERIZATION OF
OPTICALLY PUMPED ALKALI LASER SYSTEMS

DISSERTATION

Presented to the Faculty

Graduate School of Engineering and Management

Air Force Institute of Technology

Air University

Air Education and Training Command

In Partial Fulfillment of the Requirements for the

Degree of Doctor of Philosophy

Clifford V. Sulham, BS, MS

Major, USAF

September 2010

APPROVED FOR PUBLIC RELEASE; DISTRIBUTION UNLIMITED

AFIT/DS/ENP/10-S06

LASER DEMONSTRATION AND PERFORMANCE CHARACTERIZATION OF
OPTICALLY PUMPED ALKALI LASER SYSTEMS

Clifford V. Sulham, BS, MS
Major, USAF

Approved:

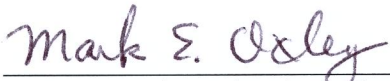_____          8 Sep 10
Glen P. Perram, PhD (Chairman)              Date

_____          8 Sep 10
Lt Col Jeremy C. Holtgrave (Member)         Date

_____          8 Sep 10
Mark E. Oxley, PhD (Member)                 Date

Accepted:

_____          10 Sep 2010
M. U. Thomas                                Date
Dean, Graduate School of Engineering
   and Management

AFIT/DS/ENP/10-S06

**Abstract**


Diode Pumped Alkali Lasers (DPALs) offer a promising approach for high power lasers in military applications that will not suffer from the long logistical trails of chemical lasers or the thermal management issues of diode pumped solid state lasers. This research focuses on characterizing a DPAL-type system to gain a better understanding of using this type of laser as a directed energy weapon. A rubidium laser operating at 795 nm is optically pumped by a pulsed titanium sapphire laser to investigate the dynamics of DPALs at pump intensities between 1.3 and 45 kW/cm$^2$. Linear scaling as high as 32 times threshold is observed, with no evidence of second order kinetics. Comparison of laser characteristics with a quasi-two level analytic model suggests performance near the ideal steady-state limit, disregarding the mode mis-match. Additionally, the peak power scales linearly as high as 1 kW, suggesting aperture scaling to a few cm$^2$ is sufficient to achieve tactical level laser powers. The temporal dynamics of the 100 ns pump and rubidium laser pulses are presented, and the continually evolving laser efficiency provides insight into the bottlenecking of the rubidium atoms in the $^2P_{3/2}$ state. Lastly, multiple excited states of rubidium and cesium were accessed through two photon absorption in the red, yielding a blue and an IR photon through amplified stimulated emission. Threshold is modest at 0.3 mJ/pulse, and slope efficiencies increase dramatically with alkali concentrations and peak at 0.4%, with considerable opportunity for improvement. This versatile system might find applications for IR countermeasures or underwater communications.

iv

## Acknowledgments

I would like to express my sincere appreciation to my faculty advisor, Dr. Glen Perram, for his guidance and support throughout the course of this effort.  The insight and experience he provided was certainly appreciated.  I would also like to thank Greg and Mike, for all of their help getting equipment and for teaching me the right way to use the equipment I had.  I certainly would not have been able to complete my work on time without their countless hours of assistance.  In addition, I would be remise to not thank both Tony and Wade at the center of excellence at Kirtland AFB for their assistance during data collection at their facility, as well as the high energy laser joint technology office for providing the funding for not only my travel, but for most of the equipment I required in both New Mexico and at AFIT.  Finally I need to thank my wife and children, for supporting me throughout the course of this program.  I would not have been able to return to AFIT, and without a doubt wouldn't have successfully completed the degree without their support.  They put up with countless late nights of work, and didn't complain when I was required to come in to work on the weekends.  Thanks guys, I couldn't have done it without you.

Clifford V. Sulham

# Table of Contents

## List of Figures

## List of Tables

# LASER DEMONSTRATION AND PERFORMANCE CHARACTERIZATION OF OPTICALLY PUMPED ALKALI LASER SYSTEMS

## I. Introduction

**Alkali Lasers**

Although optically pumped alkali lasers were originally proposed long ago, they have only recently been demonstrated as laboratory systems. The first alkali laser pumped on the $D_2$ line and lased on the $D_1$ line was demonstrated by Krupke et al. in 2003 using rubidium as the gain medium[11]. It was quickly followed by many others with varying types of pump sources and using different alkali atoms. The interest in the alkali laser systems stems in part from the small quantum defect between the pumped level and the laser level as shown in Table 1 as well as the large optical cross section in the alkalis and their well known collisional mixing rates. In addition, the $D_2$ pump transitions for potassium, rubidium, and cesium are well matched with existing laser diodes.

The term Diode Pumped Alkali Laser (DPAL) was coined by Beach [4], and is taken to represent any three level alkali laser system which is optically pumped and uses the alkali vapor as the gain medium. The alkali atoms are pumped from the $^2S_{1/2}$ ground

state to the $^2P_{3/2}$ second excited state. This transition from the $^2S_{1/2}$ to the $^2P_{3/2}$ is commonly referred to as the alkali's $D_2$ line.

**Table 1. Alkali $D_1$ and $D_2$ transition wavelengths and fine structure splitting [5]**

| Alkali | $D_1$ (laser) (nm) | $D_2$ (pump) (nm) | $\Delta E$ ($^2P_{3/2} - {}^2P_{1/2}$) (cm$^{-1}$) |
|--------|--------------------|--------------------|------------------------------------------------------|
| Li | 670.98 | 670.96 | 0.444 |
| Na | 589.76 | 589.16 | 17.2 |
| K | 770.11 | 766.70 | 57.7 |
| Rb | 794.98 | 780.23 | 237 |
| Cs | 894.59 | 852.35 | 554 |

Once in the excited $^2P_{3/2}$ state, the alkali atoms are collisionally relaxed to the $^2P_{1/2}$ state. Lasing occurs between the $^2P_{1/2}$ state and the ground state $^2S_{1/2}$ on the $D_1$ line. An example of this is shown in Figure 1 from Krupke's original paper for the rubidium transitions.

In addition to the alkali vapor gain medium in the laser cell, other gases must be added to increase the efficiency of the system. A buffer gas is needed to pressure broaden the absorption line of the alkali atoms to effectively match the line width of the pump source employed.
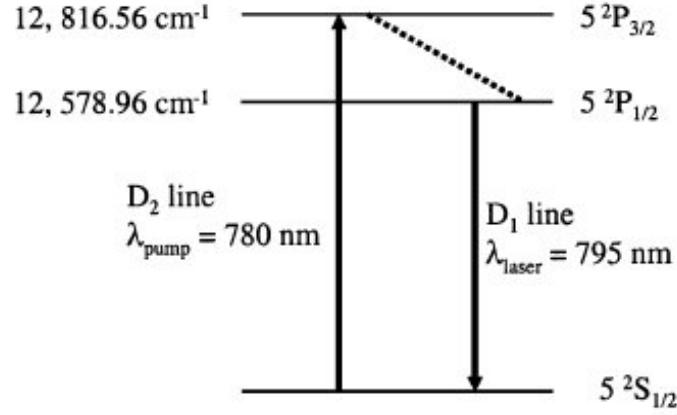
**Figure 1.  Energy levels accessed in a rubidium DPAL [11].**

A comparison of a typical narrowbanded diode pump source with a sub atmospheric

pressure broadened absorption line is shown in Figure 2.  Also, a spin-orbit relaxing gas

must be present to provide the mechanism to rapidly collisionally relax the alkali atoms

from the $^2P_{3/2}$ state to the $^2P_{1/2}$ state.
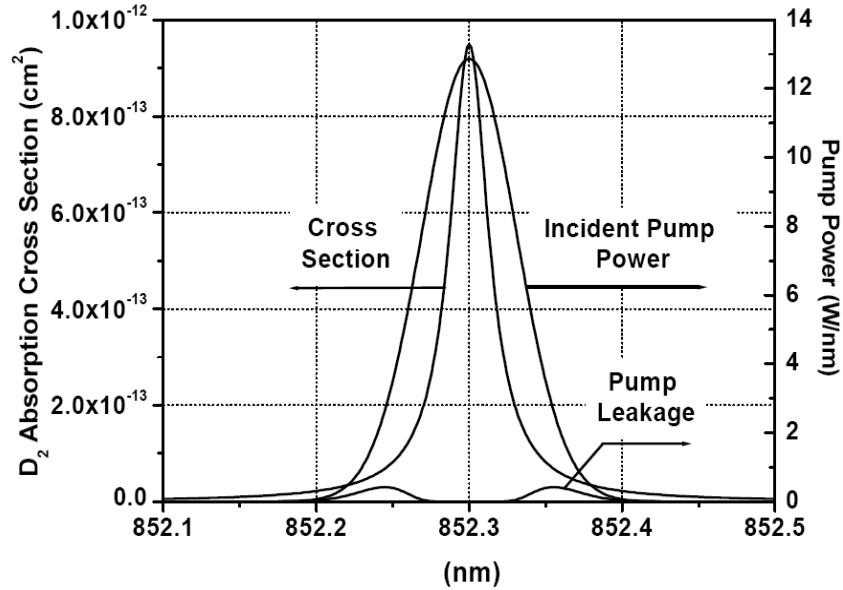


**Figure 2.  Spectral bandwidth of a pump laser and simulated D$_2$ absorption
lineshape [5].**

The energy transfer rate of the fine split $^2$P states is referred to as the spin orbit coupling rate, and must be significantly faster than the radiative lifetime of the $^2$P$_{3/2}$ state, which is on the order of 25 ns for rubidium. In addition this rate should also be faster than the absorption rate, $R_{absorption}$, which is roughly,

$$R_{absorption} = \frac{I}{I_{SAT}} \frac{1}{\tau_R} \qquad (1)$$

where $I$ is the pump intensity, $I_{SAT}$ is the saturation intensity, and $\tau_R$ is the radiative lifetime. When the spin orbit rate is faster than $R_{absorption}$ the system can be analytically approximated by the quasi-two level model. If the spin orbit coupling rate is not much faster than the absorption rate, then the alkali atoms begin bottlenecking in the $^2$P$_{3/2}$ state and laser performance is degraded.

There are two approaches to effectively matching the pump spectral linewidth to the alkali's absorption linewidth. The first is to use existing laser diodes as pump sources. This requires pressures of several atmospheres to sufficiently broaden the absorption line. Second, the existing laser diode technology can be improved to narrow the linewidths of the diodes by using volume Bragg gratings. Multi-atmosphere DPALs have been successfully demonstrated by researchers at the Lawrence Livermore National Laboratory, but these elevated pressures may add complexity to an operational system. The Center for Research and Education in Optics and Lasers (CREOL) at the University of Central Florida has pursued the second matching technique. Using volume Bragg gratings, they have recently narrowbanded diodes at the rubidium D$_2$ wavelength to 10

GHz with diode stacks capable of producing ~250 W of power enabling pressure broadening with sub atmospheric pressures.

Although DPALs are a promising new area of research for the Air Force, conducting research for high power laser applications is not new. In fact, a great deal of research has previously been accomplished on both the COIL and on Diode Pumped Solid State Lasers (DPSSLs) by Air Force researchers. The COIL uses a chemical reaction between basic hydrogen peroxide and chlorine gases. This chemical reaction produces an excited state of oxygen $O_2\left(a^1\Delta\right)$, which is used to pump atomic iodine to its first excited state for lasing through the process shown in equation 2 [35].

$$O_2\left(a^1\Delta\right)+I\left(^2P_{3/2}\right)\leftrightarrow O_2\left(X^3\Sigma\right)+I\left(^2P_{1/2}\right) \tag{2}$$
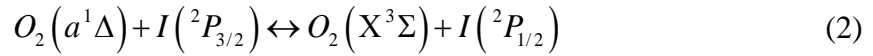
The chemical reaction that produces the excited oxygen is [35].

$$Cl_2\left(g\right)+H_2O_2\left(l\right)+2KOH\left(l\right)\rightarrow O_2\left(a^1\Delta\right)+2KCl+2H_2O \tag{3}$$
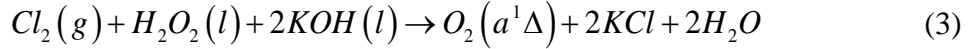
Although capable of producing powers on the order of a megawatt, there are several drawbacks to employing this type of laser in an operational system. First is the logistical trail required to transport the necessary chemicals to the battlefield. Second, is the laser firing time would be limited by the amount of chemicals that could be carried aboard the aircraft. However, even with these limitations it is important to note that COIL is a highly efficient laser system and has recently been integrated onto multiple airframes and has successfully performed testing in both a tactical mode on the advanced tactical laser (ATL) and in strategic applications on board the airborne laser (ABL). The ATL was tested in a tactical role in June 2009, and used a 100 kW class COIL device integrated onto a USAF C-130 aircraft. During several laser shots, the ATL engaged various targets

5

on the ground. More recently, the COIL was demonstrated onboard the ABL aircraft as a 1 MW class laser to be used in the strategic role of ballistic missile intercept. In February 2010, the ABL destroyed boosting missiles on two occasions demonstrating the feasibility of this type of weapon system.

In an effort to eliminate the logistical trail and limited magazine depth of COIL, research into DPSSLs has been underway for many years. The tremendous advantage to DPSSLs is their ability to be electrically pumped with laser diodes, effectively producing an unlimited amount of laser shots while the aircraft is in flight. Unfortunately, DPSSLs also have problems that must be addressed for high power applications. Since the gain medium is a solid, transport of waste heat out of the gain medium is difficult, and as the solid state material temperature increases, second order effects begin affecting laser beam quality. And to be an effective weapon system, a laser must have both high power and good beam quality. Recent demonstrations by Boeing have yielded a DPSSL capable of producing a 100 kW laser with an acceptable beam quality, and future beam quality improvements should result in an operationally viable laser system. However, with DPSSLs there is no clear path to achieving the megawatt class laser required for strategic military applications.

The possibility of an electrically pumped gas phase laser is what has driven the current Air Force and Department of Defense research into the DPAL arena. This type of laser system removes the limitations of both the COIL and DPSSLs while incorporating the positive aspects of each. Although still very early on in the development stages, DPALs exhibit tremendous potential in achieving 100 kW and even 1 MW class lasers which may be integrated onto aircraft.

The first DPAL laser was demonstrated only four years before this research effort began, and because it is such a promising technology, a large amount of research has been conducted by both the Department of Defense and the Department of Energy. In the seven years since the first rubidium laser produced 30 mW, DPALs have been demonstrated with potassium and cesium, and power outputs as high as 145 W have been reported with efficiencies only limited by volume mismatch of the pump laser and the alkali laser [11,53,30]. Although many demonstrations have been performed using alkali vapors as a gain medium, almost all of these systems have focused on increasing the power out of the laser and not necessarily fully characterizing the laser's performance. In fact, most DPAL experiments deviate very little from the operating conditions used for the initial demonstration by Krupke et al. This research effort will characterize the performance of rubidium lasers for a better understanding of the implications of using different spot sizes (mode overlap), buffer gases, and output couplers to gain the knowledge necessary to scale these systems to higher powers which will be useful for military applications. While heat loading has been observed previously, no work has been done to quantify the amount of heat buildup, or even to determine what effects occur during cell heating which degrade laser performance. An important aspect of this research for the DPAL community will be the characterization of laser degradation during heat buildup in the cell.

**Quasi-two Level Performance**

The first portion of the present work has demonstrated an optically pumped rubidium laser operating at multiple alkali concentrations and with two different output

couplers. The pump intensity reached a value 18 times the laser threshold value. The experimentally determined laser efficiency under the varying operating conditions is compared to an analytic quasi two level model which incorporates an assumption that the spin orbit rate is infinitely fast. The resulting data and analysis were accepted for publication in Optics Communications in Jun 2010, and are presented in Chapter III [30].

**Three-level Model and Temporal Dynamics**

Continuing on the path of laser characterization, another demonstration of a rubidium laser with varying buffer gas types and concentrations as well as a wider range of alkali concentrations and output couplers was performed. Pump intensities as high as 32 times threshold were achieved minimizing the initial losses required to reach threshold. Even with these high pump intensities, the data exhibited no non-linear behavior and maintained linear slope efficiencies. In general, DPAL results are not interpreted in light of existing modeling efforts. The present research compares collected pulsed alkali laser data to an existing frequency dependent three-level model. The comparison of the data to the model is performed on not only the rubidium laser power but also on the temporal pulse shapes of the laser output. In fact, no previous work has been reported on the temporal dynamics of pulsed DPAL systems, the data is always reported as an average throughout the pulse. The results of this present research were accepted for publication at the American Institute of Aeronautics and Astronautics Plasmadynamics and Lasers conference in June 2010. Expanded analysis of this data will be submitted to Applied Physics B, and is presented in Chapter IV.

**Two Photon Absorption**

Lastly, an innovative technique for producing both blue and infrared stimulated emission spots using two photon absorption in an alkali vapor was achieved in both rubidium and cesium.  All transitions in this three-level laser system are optical resulting in no thermal loading on the system.  The possibility of a laser similar to DPALs capable of lasing in the blue or the IR is very exciting to the high power laser community as well as the IR countermeasures community.  A high power laser operating in the blue versus the red, can be focused to a smaller spot as a result of its shorter wavelength resulting in greater damage given similar power levels.  Additionally, an IR laser capable of operating over a wide range of lines in the near to mid IR bands could be used in an IR countermeasures application.  The results of this research were published in the Journal of Applied Physics B: Lasers and Optics and are presented in Chapter V [29].

## II. Background

**Alkali Data**

In theory, any of the alkali's listed in Table 1 can be used in a three-level laser system to create a DPAL system. However, for practical applications, potassium, rubidium and cesium are the most useful due to the close energy spacing of the $^2P_{3/2}$ and $^2P_{1/2}$ states of lithium and sodium. Only rubidium and cesium were employed during the present research, and information on these elements is presented below. Tables 2, 3, 4, and 5 list many of the physical parameters for the rubidium and cesium $D_1$ and $D_2$ transitions. While Figures 3, 4, 5, and 6 show the hyperfine splitting of the two alkali's $D_1$ and $D_2$ transitions.

Employing alkali metal vapor as the gain medium for DPALs is benefited by the characterization of the elements that has been done previously. The transition optical properties in Tables 2-4 reflect many of the well characterized values that are of interest when designing a laser system. In fact, the alkali metal properties are so well known that the United States time standard is based on a cesium frequency.

Similarly, the splitting of the fine structure into the hyperfine components is extremely well known for both rubidium and cesium. While cesium has a single isotope to consider, both $^{85}$Rb and $^{87}$Rb are present in its natural isotopic abundance at 72.16% and 27.84% respectively [17]. The transition properties and hyperfine splitting are similar for the two isotopes of rubidium and only the $^{87}$Rb data is presented below.

10

**Table 2. Rubidium D$_1$ ($5^2S_{1/2}$ – $5^2P_{1/2}$) transition optical properties [27]**

| Property | Symbol | Value |
|---|---|---|
| Frequency | $\upsilon_o$ | 377.107 463 380(11) THz |
| Energy | $h\,\upsilon_o$ | 1.559 591 016(38) eV |
| Wavelength | $\lambda$ | 794.767 119(24) nm |
| Lifetime | $\tau$ | 27.679(27) ns |
| Decay Rate | $\Gamma$ | 36.129(35) x $10^6\,s^{-1}$ |
| Natural Line Width (FWHM) | $\upsilon_{Natural}$ | 5.7500(56) MHz |
| Absorption Oscillator Strength | $f$ | 0.342 31(97) |
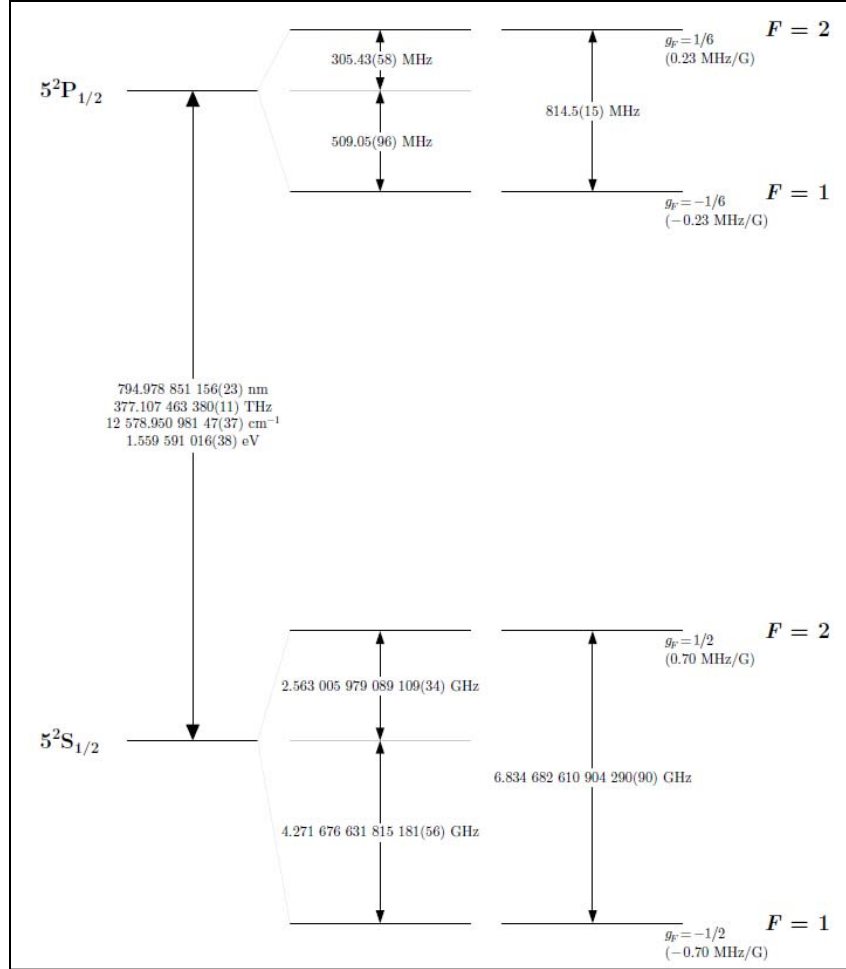


**Figure 3.  Rubidium D$_1$ ($5^2S_{1/2}$ – $5^2P_{1/2}$) hyperfine energy level splitting [27] .**

**Table 3. Rubidium D₂ (5²S₁/₂ – 5²P₃/₂) transition optical properties [27]**

| Property | Symbol | Value |
|----------|--------|-------|
| Frequency | $\upsilon_o$ | 384.230 484 468(62) THz |
| Energy | $h\,\upsilon_o$ | 1.589 049 462(38) eV |
| Wavelength | $\lambda$ | 780.241 209 686(77) nm |
| Lifetime | $\tau$ | 26.2348(77) ns |
| Decay Rate | $\Gamma$ | 38.117(11) x 10⁶ s⁻¹ |
| Natural Line Width (FWHM) | $\upsilon_{Natural}$ | 6.0666(18) MHz |
| Absorption Oscillator Strength | $f$ | 0.695 77(29) |
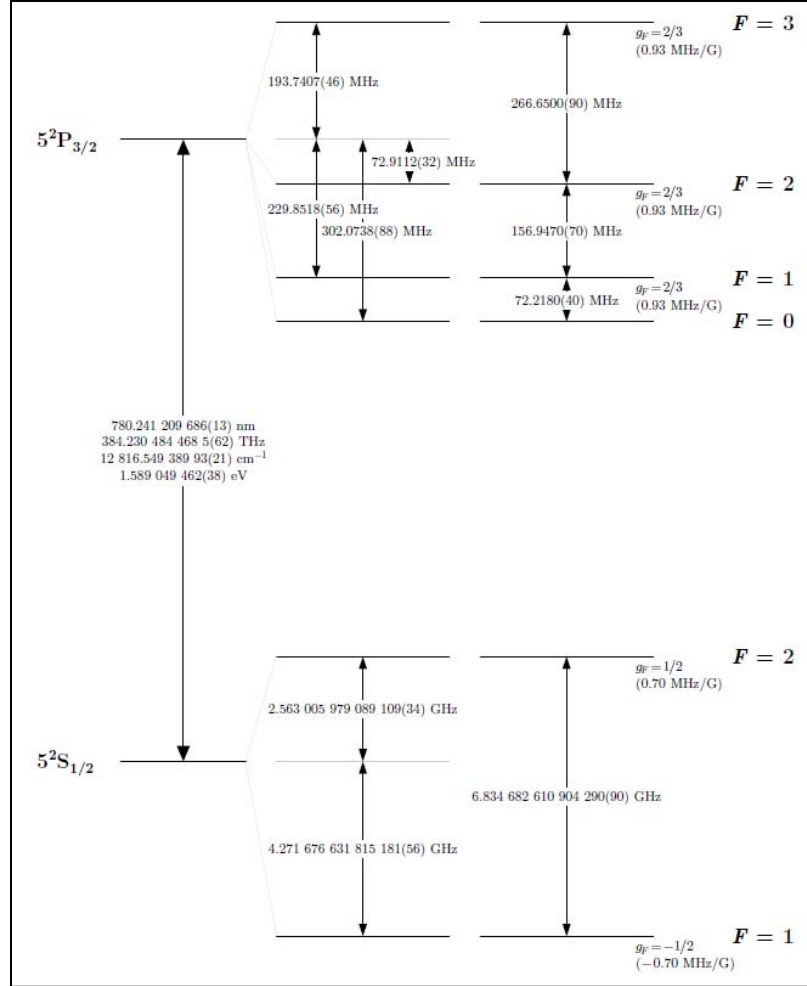


**Figure 4. Rubidium D₂ (5²S₁/₂ – 5²P₃/₂) hyperfine energy level splitting [27].**

12

**Table 4. Cesium D$_1$ ($6^2$S$_{1/2}$ – $6^2$P$_{1/2}$) transition optical properties [28]**

| Property | Symbol | Value |
|---|---|---|
| Frequency | $\upsilon_o$ | 335.116 048 807(41) THz |
| Energy | $h\,\upsilon_o$ | 1.385 928 495 (34) eV |
| Wavelength | $\lambda$ | 894.592 959 86(10) nm |
| Lifetime | $\tau$ | 34.791(90) ns |
| Decay Rate | $\Gamma$ | 28.743(75) x $10^6$ s$^{-1}$ |
| Natural Line Width (FWHM) | $\upsilon_{Natural}$ | 4.575(12) MHz |
| Absorption Oscillator Strength | $f$ | 0.3449(26) |
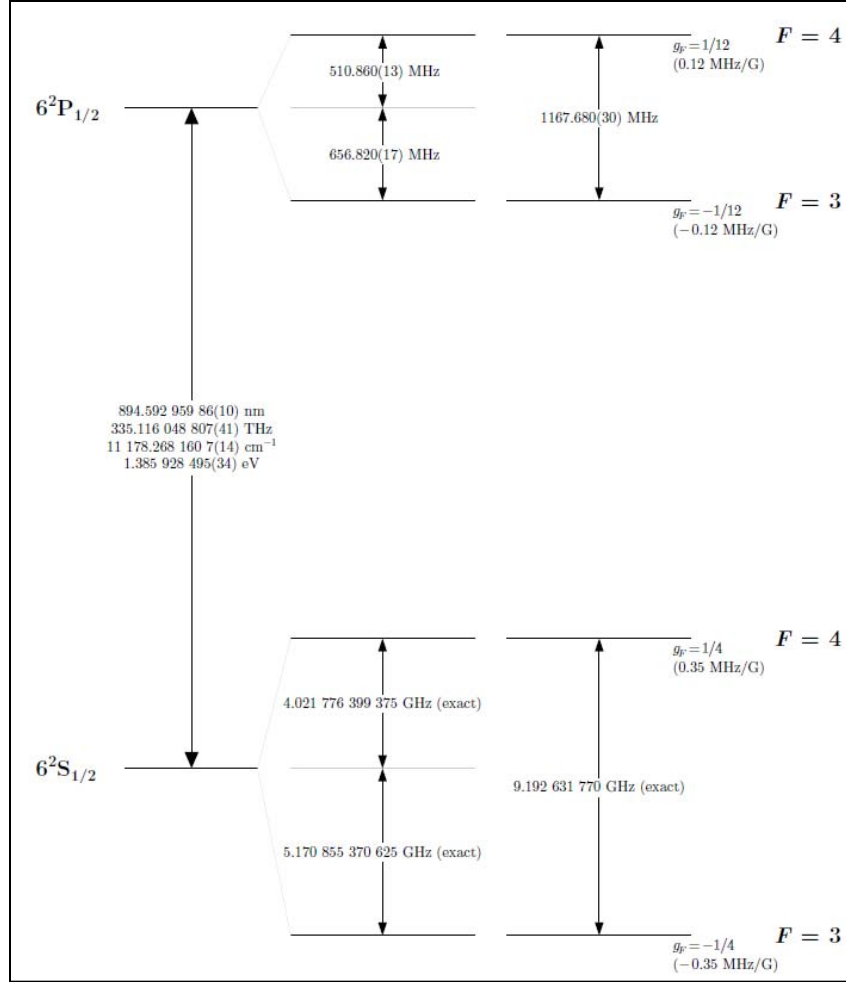


**Figure 5.  Cesium D$_1$ ($6^2$S$_{1/2}$ – $6^2$P$_{1/2}$) hyperfine energy level splitting [28].**

13

**Table 5. Cesium $D_2$ ($6^2S_{1/2} - 6^2P_{3/2}$) transition optical properties [28]**

| Property | Symbol | Value |
|---|---|---|
| Frequency | $\upsilon_o$ | 351.725 718 50(11) THz |
| Energy | $h\,\upsilon_o$ | 1.454 620 563(35) eV |
| Wavelength | $\lambda$ | 852.347 275 82(27) nm |
| Lifetime | $\tau$ | 30.405(77) ns |
| Decay Rate | $\Gamma$ | 32.889(84) x $10^6$ $s^{-1}$ |
| Natural Line Width (FWHM) | $\upsilon_{Natural}$ | 5.234(13) MHz |
| Absorption Oscillator Strength | $f$ | 0.7164(25) |
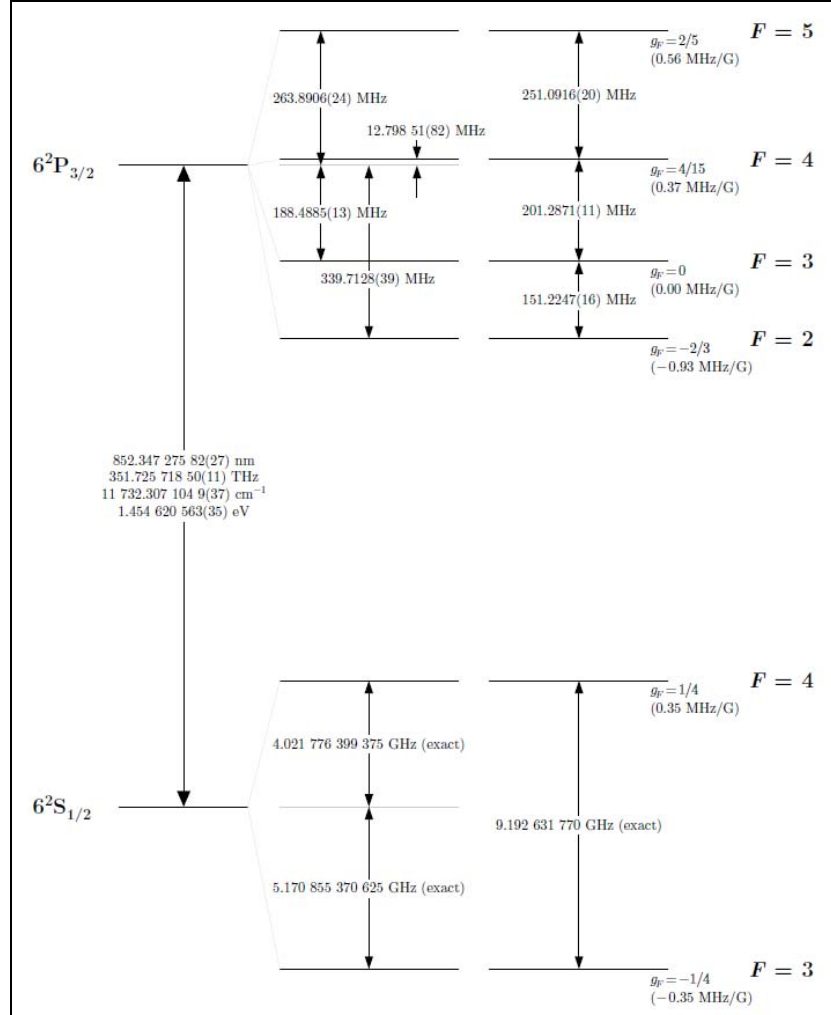


**Figure 6. Cesium $D_2$ ($6^2S_{1/2} - 6^2P_{3/2}$) hyperfine energy level splitting [28].**

14

Alkali lasers rely on heating the metal until the vapor pressure creates a number density high enough to produce gain. The temperatures typically used for rubidium and cesium lasers are between 100°C and 120°C. The vapor pressure curves are well known for these alkali metals [27, 28]. The vapor pressure equations for the liquid phase of rubidium and cesium are shown in equation 4 and 5 respectively, where $P_v$ is the vapor pressure in Torr and $T$, is the temperature in Kelvin. The alkali number densities from the vapor pressure curves are shown in Figure 7.

$$\log_{10} P_v = 2.881 + 4.312 - \frac{4040}{T} \qquad 312 < \mathrm{T} < 550 \qquad (4)$$

$$\log_{10} P_v = 2.881 + 4.165 - \frac{3830}{T} \qquad 302 < \mathrm{T} < 550 \qquad (5)$$
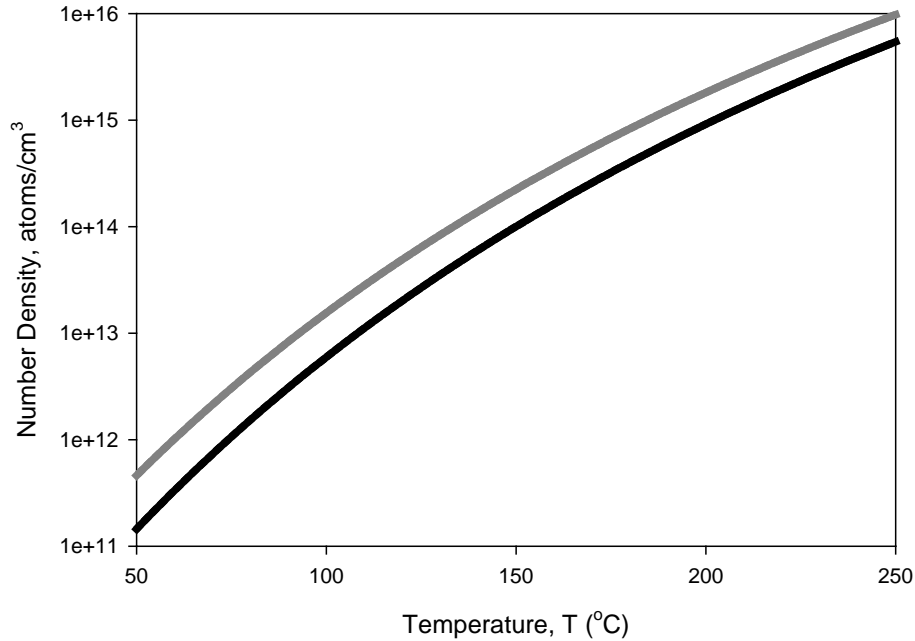


**Figure 7.  Vapor pressure curves of rubidium (▮) and cesium(▮) [27, 28]**

15

Even with the recent advancements in narrowbanding of diode stacks, DPAL systems still required pressure broadening of the absorption line.  In addition to the pressure broadening gas, an additional gas is required to provide the coupling between the spin orbit split $^2P_{3/2}$ and $^2P_{1/2}$ states.  For rubidium, both the pressure broadening rates, reported in MHz/Torr, and the collisional cross section, reported in $cm^2$, are well known for the gases most commonly used in DPALs.  The cross sections and pressure broadening rates for methane, ethane, and helium are shown in Table 6.

**Table 6. Rubidium spin orbit coupling cross sections and pressure broadening rates [22, 23, 36, 38]**

| Buffer Gas | Cross Section $\sigma_{P_{3/2} \to P_{1/2}} \left( \times 10^{-16} cm^2 \right)$ | Pressure Broadening Rate, $D_2$ line (MHz/Torr) |
|---|---|---|
| Methane | $41.0 \pm 5$ | $26.2 \pm 0.6$ |
| Ethane | $77.0 \pm 7.7$ | $28.1 \pm 0.7$ |
| Helium | $0.5$ | $20.0 \pm 0.14$ |

**Previous Laser Demonstrations**

Since their first demonstration in 2003 [11], a significant amount of research has been performed using one of the alkalis as the gain medium in a gas phase laser.  To date, potassium, rubidium, and cesium have successfully been lased.  Primarily, ethane, methane, and helium, or some combination of them, have been used for both spin orbit relaxation and for pressure broadening of the $D_2$ absorption line.  Initially, surrogate pump sources were used instead of diodes, but recently both surrogate and diode stacks have been incorporated into DPALs.  Most researchers working on DPAL systems report

16

their results in power or energy per pulse.  However, laser performance depends upon the

intensity of the pump source and not its power, so it is important to analyze the number or

times above threshold that an experiment achieves.  Since DPAL systems must be

bleached to begin lasing, the threshold value is large compared to other laser systems and

for this initial loss to be negligible, or to achieve a high total efficiency, the laser must

operate at many times the threshold value.  Throughout this document the term bleached

will imply the pump transition is saturated in the presence of lasing.  A summary of the

previous work accomplished on DPAL systems is presented in Table 7**.**

**Table 7. Relevent alkali laser demonstrations**

| Year | Alkali | Pulsed CW | Buffer Gas | Power/Energy Achieved | | Slope Eff. | Times above Threshold | Reference |
|------|--------|-----------|------------|----------------------|--|------------|----------------------|-----------|
| 2003 | Rb | CW | $C_2H_6$ / He | 0.03 W | | 0.54 | 1.4 | [11] |
| 2004 | Cs | CW | $C_2H_6$ / He | 0.23 W | | 0.34 | 2.3 | [5] |
| 2005 | Rb | Pulsed | $C_2H_6$ / He | 0.80 W | 80 mJ | | 4.0 | [16] |
| 2006 | Rb | CW | $C_2H_6$ / He | 0.40 W | | 0.32 | 1.9 | [18] |
| 2006 | Cs | Pulsed | $C_2H_6$ / He | 1.50 W | | 0.06 | 2.8 | [33] |
| 2006 | Cs | Pulsed | $C_2H_6$ / He | .013 W | 13 µJ | 0.02 | 1.6 | [34] |
| 2006 | Cs | CW | $C_2H_6$ | 0.38 W | | 0.81 | 5.5 | [42] |
| 2006 | K | CW | $C_2H_6$ | 0.01 W | | 0.2 | 1.1 | [43] |
| 2007 | Rb | CW/chopped | $C_2H_6$ / He | 0.02 W | | | 10.0 | [12] |
| 2007 | Rb | CW | $^3$He | 0.34 W | | 0.21 | 4.1 | [36] |
| 2007 | Rb | CW | $^4$He | 0.12 W | | | 4.5 | [37] |
| 2007 | Cs | CW | $C_2H_6$ | 10.00 W | | 0.68 | 6.4 | [45] |
| 2007 | K | CW | He | 0.04 W | | 0.19 | 1.2 | [44] |
| 2008 | Cs | CW/chopped | $C_2H_6$ / He | 48.00 W | | 0.52 | 12.0 | [40] |
| 2008 | Rb | CW | $C_2H_6$ | 17.00 W | | 0.53 | 6.3 | [41] |
| 2008 | Rb | CW | $C_2H_6$ | 8.00 W | | 0.60 | 4.5 | [46] |
| 2009 | K | Pulsed | He | .090 W | 9 mJ | | 8.0 | [54] |
| 2010 | Rb | CW | $CH_4$ / He | 145.00 W | | 0.28 | 7.0 | [53] |
| 2010 | Rb | Pulsed | $CH_4$ | 1.00 W | 100 µJ | 0.30 | 32.0 | [30] |

**Soot Deposition on Windows**

Several researchers have demonstrated alkali cell window degradation at

temperatures above 120$^o$C [16, 45].  When temperatures are maintained below this level,

the deposits on the windows do not occur, even when the laser was operated for several hours.  They suggest that the reason for the contamination on the cell windows is due to a chemical reaction between the ethane and the alkali.  The reaction appears to require both elevated temperatures and the interaction of the laser light.  The chemical reaction appears to produce both an alkali hydrate in the form of a white powder, and carbon deposits in the form of soot.  An example of the cell window contamination reported by Zhadanov et al. is shown in Figure 8.
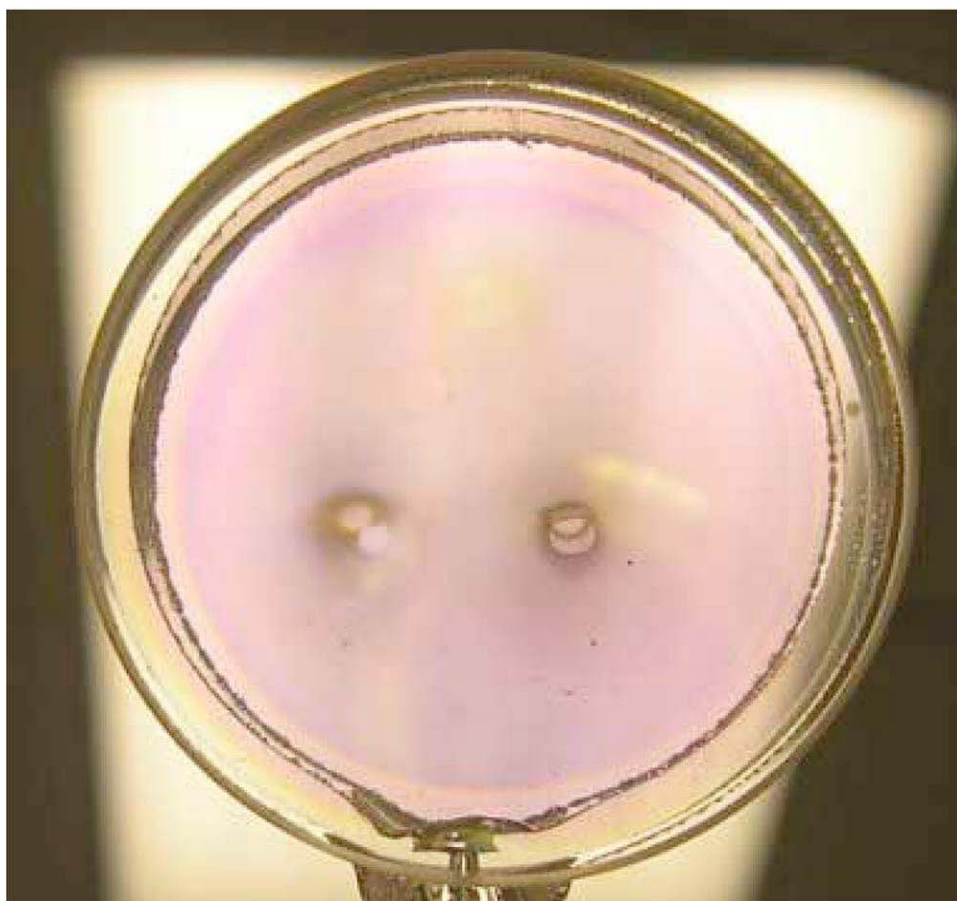


**Figure 8.  Soot deposition on alkali cell windows [45].**

**Output Coupler Effects**

        Given the high gain produced by the alkali atoms, a minimal amount of feedback

is required to keep the gain above the round trip cavity losses.  Typical output coupler

reflectivities are around 20% reflective.[5, 46, 54]  However, the optimum output coupler

has been shown to reach as high as 40% reflective.[18]  The slope efficiency dependence

on output coupler reflectivity for multiple concentrations of ethane was reported by

Perschbacher et al. and is shown in Figure 9.
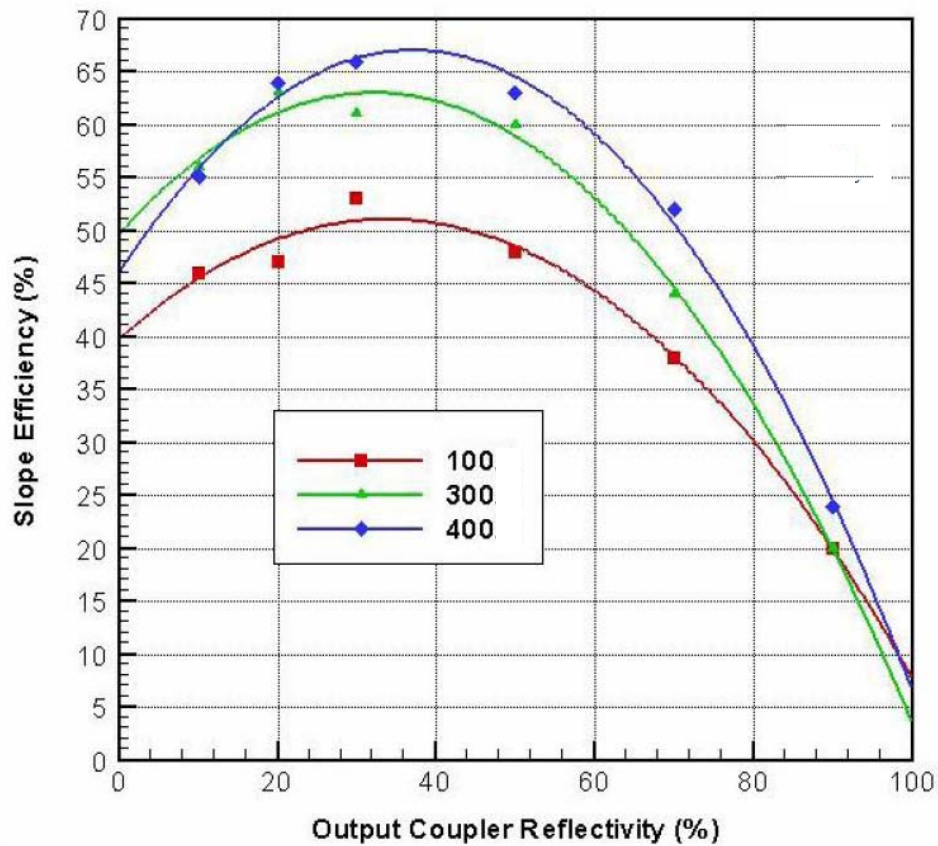


**Figure 9.  Laser performance dependence on output coupling reflectivity while employing 100, 300, or 400 Torr of ethane [18].**

**High Power CW Issues**

While employing a laser diode array capable of producing 100 W of pump power,

Zhdanov et al. observed a decrease in laser performance at high pump powers exhibited

as a roll over in the laser output power [40]. However, when a chopper was placed into

their experimental setup with a duty cycle of 10%, the laser output power was linear.

Zhdanov proposed that the roll over while operating the laser under CW conditions was a

result of thermal effects due to the heat generated through the cesium's quantum defect.

They further hypothesize that this increase in temperature can result in thermal lensing

within the laser cavity which could change the laser configuration by increasing losses

within the cavity. To date, no research has been done to test this hypothesis. The data

presented by Zhdanov et al. comparing CW to pulsed operation is shown in Figure 10.
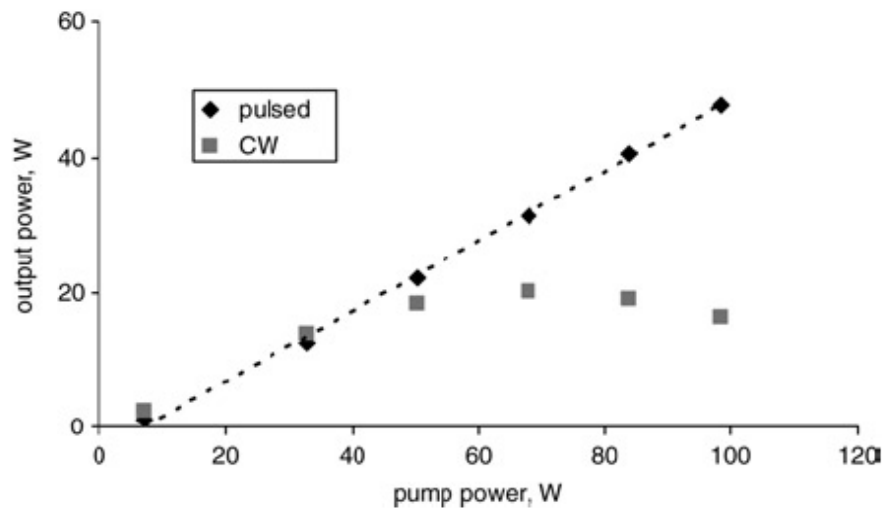


**Figure 10. Laser performance for a CW (□) system, 100% duty cycle, and the same pump source in a chopped mode (♦), 10% duty cycle[40]**

**Status of DPAL Models**

Several modeling efforts have been undertaken in an attempt to accurately represent a DPAL. Beach et al. developed the first CW model only one year after the first rubidium laser demonstration [5]. Their model has been compared to several sets of laser performance data from several researchers and accurately models the data under standard DPAL conditions. Similarly, the Aerosoft corporation, under contract to the Directed Energy directorate of the Air Force Research Laboratory has undertaken an extensive high power CW modeling effort for DPALs, and their initial results appear very promising [14]. Lastly AFIT has developed two models for DPALs. The first is a quantitative model that assumes the laser is operating in the quasi-two level limit, and is compared to experimental data in Chapter III [8]. The second AFIT model is for a pulsed DPAL, which presents more of a challenge than the previous CW systems [54]. For a pulsed system, the assumption of operating at steady state cannot be made, and the differential equations that describe the laser operation can not be set to zero, and as a result they must be solved numerically. The comparison of the pulsed model to data collected during this effort is presented in Chapter IV.

### III. A Pulsed, Optically-Pumped Rubidium Laser at High Pump Intensity

**Introduction**

The Diode Pumped Alkali Laser (DPAL) system employs diode bars to optically excite the first $^2P_{3/2}$ state of the alkali metals via strong absorption on the $D_2$ transition followed by collisional relaxation to the spin orbit split $^2P_{1/2}$ state and lasing to the ground state on the $D_1$ transition [11, 5]. The three-level laser exhibits a high threshold for pump intensity, ~ 1 kW/cm$^2$, as the gain volume must be fully bleached to achieve lasing.[22,42,43,8] Indeed, analytic modeling establishes a pump threshold that depends directly on the alkali atom concentration and cavity losses.[8] Early laser demonstrations achieved slope efficiencies as high as 81%,[42] but were limited to pump intensities of 1.5 - 6 times threshold.[11,5,22,42,7,18,46] More recently, pump intensities have been scaled to 10-14 times threshold.[54,40] In particular, the cesium laser pumped by four laser diode arrays achieved linear scaling to a peak power of 100 W, or ~ 14 times threshold, if the pump duration was limited to 0.1 s.[40]

Ideal DPAL performance is achieved when spin-orbit relaxation is much faster than the excitation rate. Under these conditions, a quasi-two level analytic model has been developed where the output intensity above threshold scales linearly with input intensity.[8] Most experiments have illustrated the attainment of this limit where bottlenecking, resulting from insufficient spin-orbit relaxer concentration, is avoided. Sublinear performance has been observed at higher heat loading.[40] However, the cause is not well understood and might also be attributable to lower on-axis concentrations.[48]

DPAL performance would be degraded if energy pooling or nonlinear excitation processes removed population from the three lowest atomic states. Atomic emission has been observed from numerous higher lying states when the pump intensity and alkali concentration is sufficiently high [10,3]. For pulsed excitation at 15 mJ in an 8 ns pulse and rubidium concentrations of $> 10^{16}$ atoms/cm$^3$ (T > 543 K), emission from more than 30 highly excited states has been observed.[20] Furthermore, ionization of the alkali atoms is achievable when the alkali number density is high and might catastrophically degrade laser performance.[3] The limit for linear intensity scaling in the DPAL system is unknown and is a key issue addressed in the present work. By scaling to many times above threshold, the overall system efficiency may be significantly improved by reducing the initial loss to bleach the sample.

The dependence of threshold and slope efficiency on cavity losses has been observed in a number of experiments [5,18,46,36], while the total output power dependence on temperature has been observed and modeled [42,7,46,49]. In particular, Wu et al. [36] characterized the dependence of threshold and slope efficiency on output mirror reflectivity for a Rb – He laser. However, the dependence of threshold and slope efficiency on alkali concentration has not been quantitatively evaluated in the context of the recently reported analytic model.[8] Since threshold and slope efficiency depend critically on the number of absorbed photons, they present an opportunity to evaluate the character of the bleached wave under lasing conditions. In the present work we seek to place threshold and efficiency observations in context of the recently developed analytic model.[8] In particular, the effective value for the $D_2$ absorption cross-section for broadband optical excitation in the presence of lasing is examined.

**Experimental Setup**

      A frequency doubled Nd:YAG (Quantronix Eagle) laser pumped, cryogenically cooled Ti:Sapphire (KML) laser was used as the excitation source for the Rb laser, as illustrated in Figure 11.
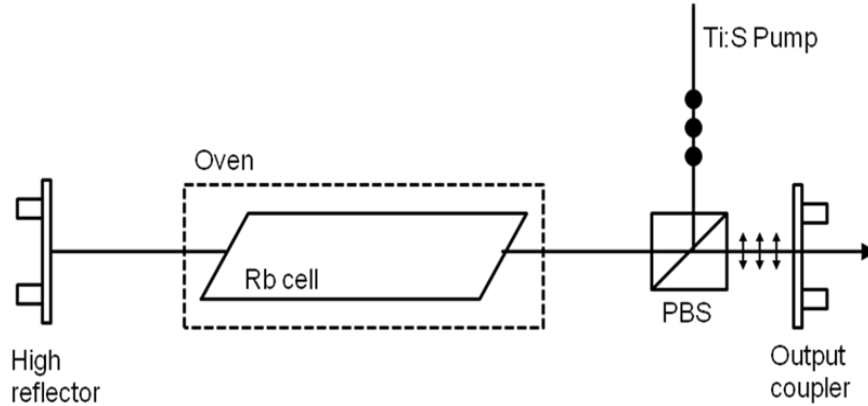


**Figure 11.  Optically pumped rubidium laser apparatus.**

The Ti:Sapphire laser produced 100 ns pulses of 1.89 mJ/pulse and 10 kHz for an average power of 18.9 W. The energy delivered to the alkali cell was varied from 0 - 0.2 mJ/pulse by rotating the linear polarization of the pump beam with a half wave plate relative to the polarizing beam splitter.  For one set of experiments, a Photonics Industries DLM-100 laser was used to pumped the same cryo-cooled Ti:Sapphire.  In this configuration, incident laser energy was scaled by 50% more to achieve 0.3 mJ/pulse.

      The glass rubidium cell was 12.7 cm long by 2.54 cm wide with Brewster angle quartz widows.  The cell was housed in an aluminum oven with independent control of the temperatures of the gain volume and the alkali stem attached to the bottom of the cell. The alkali source was typically maintained at 373 - 393K, corresponding to Rb vapor

pressures of 0.8 - 2.0 x $10^{13}$ atoms/cm$^3$, inferred by cell temperature, while the gain volume was generally 3 C higher.  The cell was filled with 550 Torr of methane at room temperature (1.8 x $10^{19}$ molecules/cm$^3$) and sealed before installation in the heater block. The methane serves both as a collision partner for relaxation between the pumped and upper laser level spin-orbit split states, and to collisionally broaden the D$_2$ pump transition.

The spectral width of the pump sources was measured by a Yokogawa AQ6370 optical spectrum analyzer as 34.5 GHz.  The source is spectrally broad relative to the Rb D$_2$ absorption feature. The broadening rate for methane on the Rb D$_2$ line is 26.2 MHz/Torr at 394K,[22] establishing a Lorentzian linewidth (FWHM) of 18.5 GHz.  The full hyperfine splitting and isotopic variance has been modeled previously, and reduces the absorption cross-section at line center compared to a single Lorentzian approximation by less than 15% for the current experimental conditions.[19]  A comparison of the pump spectral bandwidth and absorption feature is provided in Figure 12.

The Rb laser cavity was formed by a concave high reflector of 1.0 m radius of curvature and a flat output coupler of either 23% or 32% reflectivity, separated by 0.4 m, as illustrated in Figure 3. The alkali cell was located at 16 cm to 28.7 cm from the output coupler.  The TEM$_{00}$ Gaussian beam for this resonator exhibits a waist at the output coupler of 0.23 mm.  Note that the mirror diameters of 5 cm and alkali cell diameter of 2.5 cm are not represented to scale in Figure 13.  Location of laser spot measurements in relation to alkali cell position are shown in Figure 13.
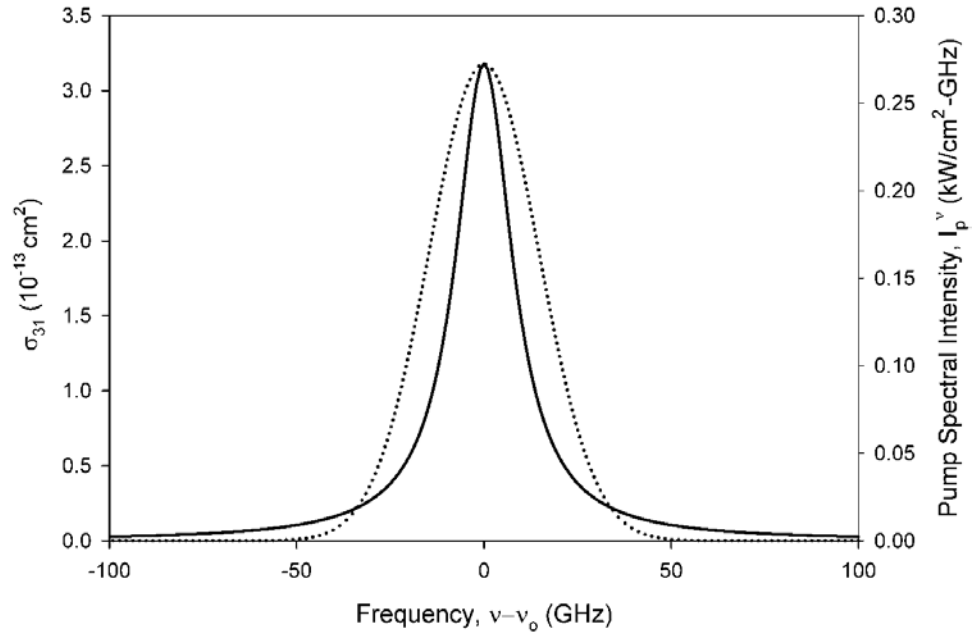
**Figure 12. Spectral bandwidth of: (…) pump laser and (___) simulated $D_2$ absorption lineshape.**
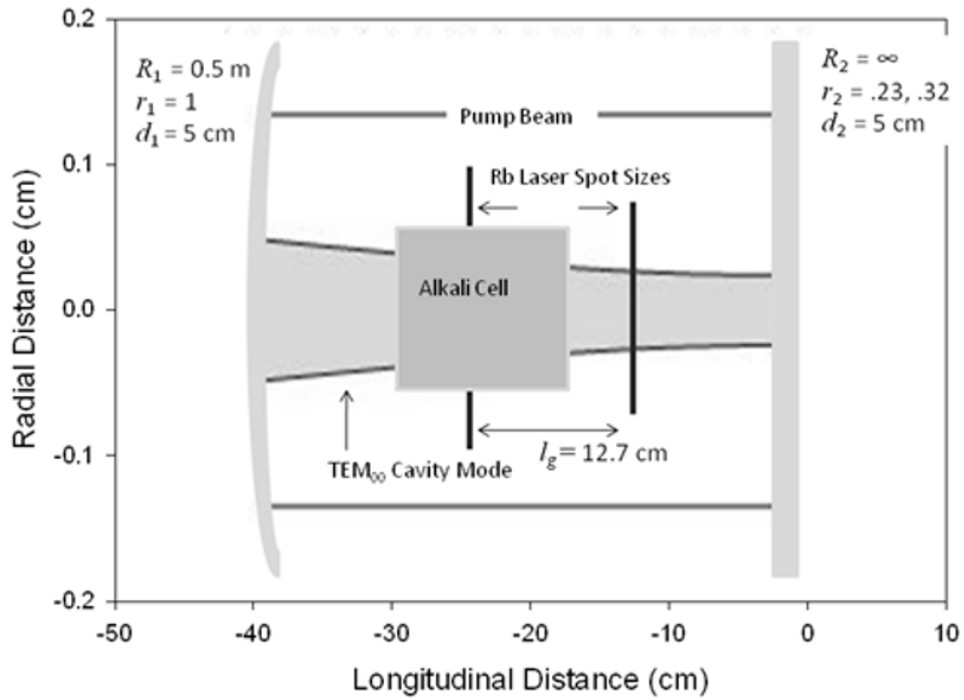


**Figure 13. Laser cavity geometry and beam spot sizes.**

Average pump power was recorded between the beam splitter and the gain volume using an OPHIR model L30A-SH-V1 power meter.  The Rb laser power was recorded with the same power meter after transmission through a 795 nm filter to block any residual pump power which leaked through the polarizing beam splitter. The pump laser wavelength was centered on the $D_2$ absorption feature by maximizing the ratio of the $D_1$ to $D_2$ line fluorescence from a separate reference cell using an Ocean Optics USB4000 spectrometer.  The spot sizes of the pump and laser beams were observed at several distances using a Newport LBP-HR beam profiler.  The temporal character of the pump and laser beams were simultaneously recorded and averaged over 20 pulses with two New Focus model 1621 nanosecond rise-time photodiodes and an Agilent MSO6104A 1GHz oscilloscope.

**Results**

### Characterization of Pump and Laser Intensity

The three-level DPAL system requires bleaching of the pump transition, which depends critically on pump intensity.  To determine the spatial characteristics of the pump and laser beams, and define the spatial mode overlap, the spot sizes of both beams were recorded.  For the pump beam, the spots were measured at 2.54 and 50 cm in front of the gain medium, with the vertical distribution at 2.54 cm illustrated in Figure 14. At this distance, the beam is nearly circular with radii of 1.26 mm vertically and 1.1 mm horizontally and highly collimated within the resonator.  The Rb laser beam profiles were observed at 10 cm and 22.7 cm externally from the output coupler.  At 10 cm the beam

was observed as 1.62 (V) x 1.47 (H) mm with the horizontal distribution shown in Figure 14.

At 22.7 cm, the beam was larger; 2.35 x 2.00 mm. Assuming the beam is symmetrical about the flat output coupler, the size of the laser beam inside the resonator is illustrated in Figure 13. Note that the measured laser spot sizes are considerably larger than the $TEM_{00}$ cavity mode. The pumped volume of 0.57 $cm^3$ is larger than the laser beam volume of 0.32 $cm^3$, suggesting a mode overlap of $\eta_{mode} \cong 0.56$. While higher mode overlaps have been achieved for cw pumps, $\eta_{mode} = 0.6 - 0.8$,[5,42,18,54,47] the current configuration is comparable to most other demonstrations and sufficient to well characterize scaling performance.

The temporal nature of the pump and laser intensities is illustrated in Figure 15. The pump pulse duration (FWHM) is very nearly 100 ns, with a Gaussian shape marginally skewed to early times. For a pump energy of 0.2 mJ/pulse, the corresponding incident pump intensity is 46.5 $kW/cm^2$. Of course, this intensity is averaged both spatially and temporally across the pulse. The laser output pulse is also shown in Figure 15, illustrating a quasi steady response to the pump intensity. Indeed, a simplified model of the system based on longitudinally average number density and cw excitation [8] will be compared to the present results.
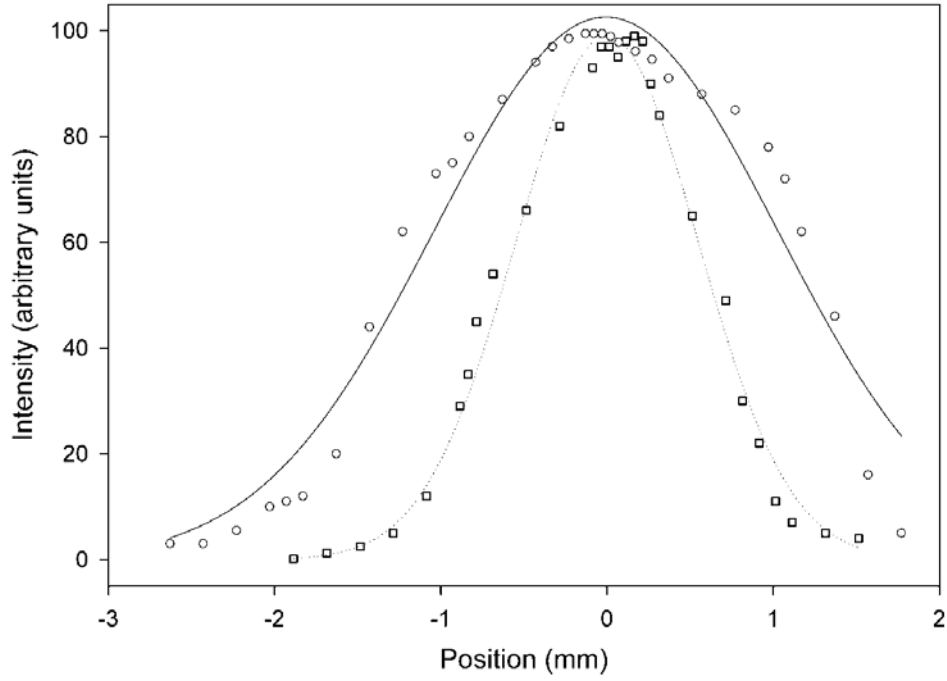
**Figure 14.  Measured beam spot sizes: (○) vertical distribution of pump laser beam at 2.54 cm in front of the gain medium and (□) horizontal distribution of the Rb laser at 10 cm from the output coupler.**
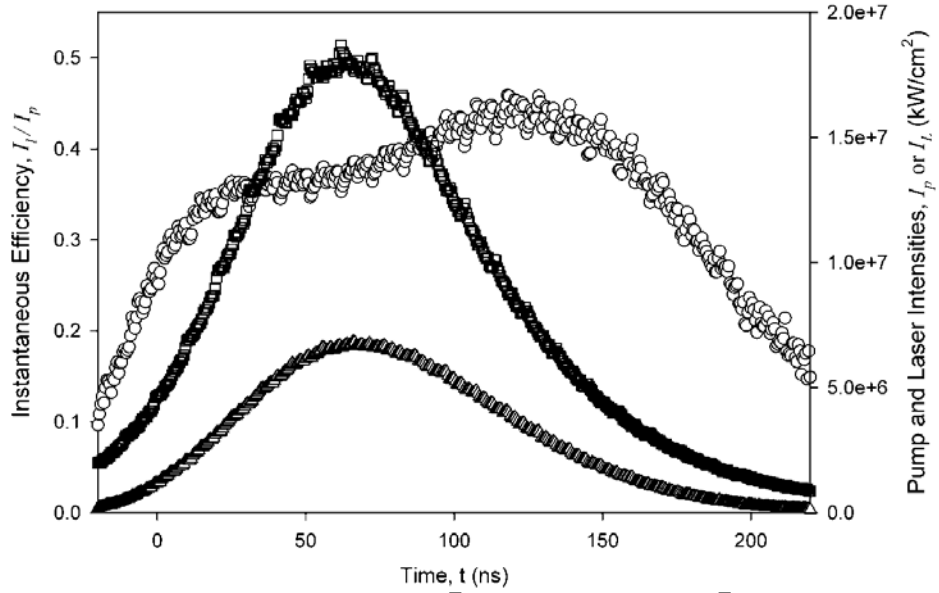


**Figure 15.  Temporal shapes for the (□) pump laser and (□) Rb laser intensities. The instantaneous laser efficiency (○) is defined by the ratio of the Rb and pump intensities.**

**Slope Efficiency and Threshold Performance**

The rubidium laser output intensity as a function of pump intensity for several cell temperatures between 379 – 393 K and the two output coupler reflectivities of 23% and 32% is provided in Figure 16 and Figure 17.

Threshold varies from 9.6 - 16.6 µJ/pulse corresponding to the fairly high intensities required to bleach the sample (1.3 - 2.2 kW/cm$^2$). The experiments corresponding to the data collections shown in Figures 16-17 were pumped with intensities up to 20 times the threshold values. For another set of experiments, a DLM-100 pump laser with higher input intensity was employed and scaling to 32.8 times threshold was achieved. Figure 18 illustrates these conditions with a threshold of 9.15 µJ/pulse and a maximum output energy of 69.5 µJ/pulse. Linear scaling to 32.8 times threshold is demonstrated, suggesting no second order kinetic or optical processes that degrade DPAL performance in this region. At these pump intensities the overall efficiency loss due to threshold values is 3%.

The slope efficiencies of 0.39 - 0.49 depend on both alkali concentration and out-coupling fraction, as seen in Figure 19.
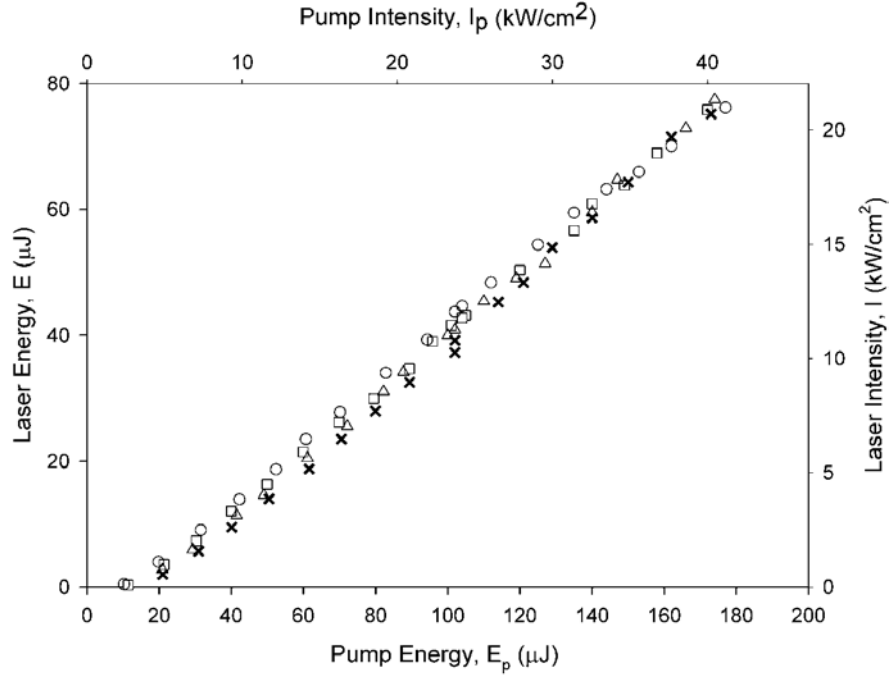
**Figure 16. Rb laser output energy per pulse as a function of input laser energy for the 32% output coupler and cell temperatures of (X) 393 K, (□) 390 K, (△) 387 K, and (○) 382 K.**
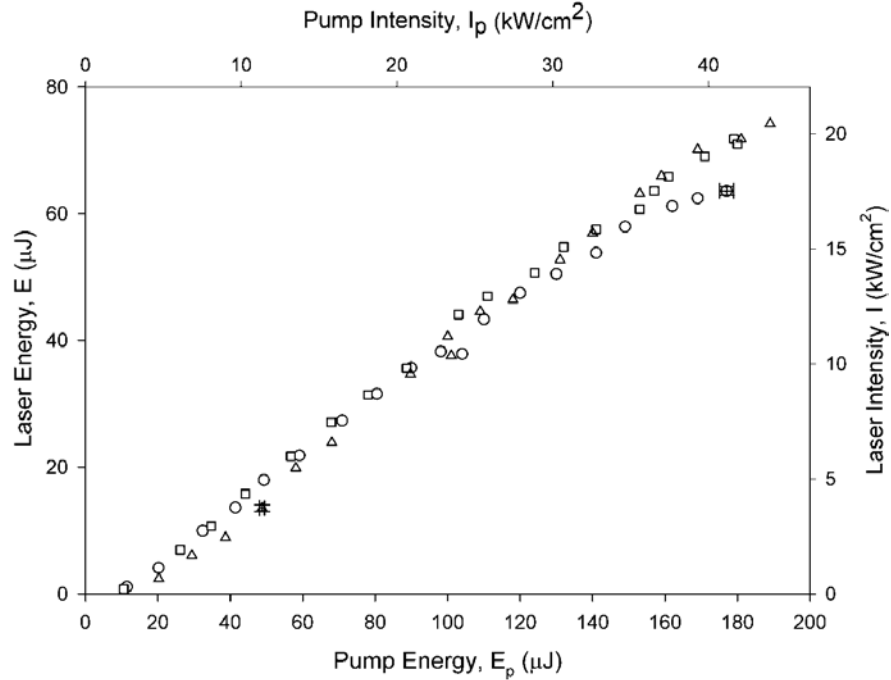


**Figure 17. Rb laser output energy per pulse as a function of input laser energy for the 23% output coupler and cell temperatures of (□) 384 K, (△) 382 K, and (○) 379 K.**

31
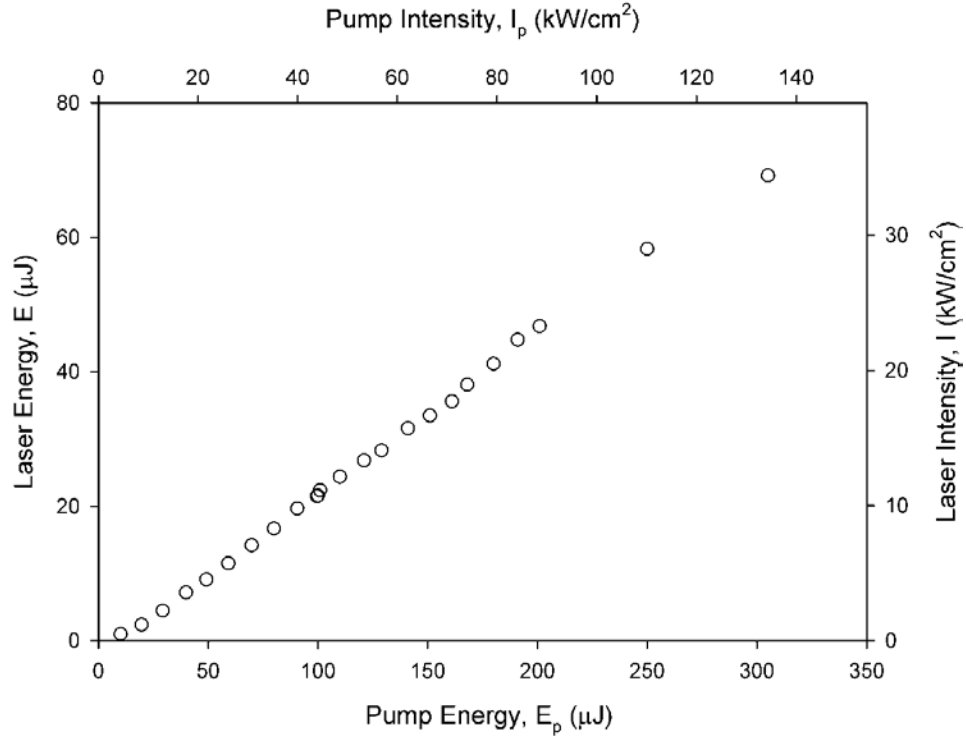
**Figure 18. Scaling of Rb laser to 32.8 times threshold for a 20% output coupler and 373 K cell filled with 200 Torr helium and 300 Torr ethane.**
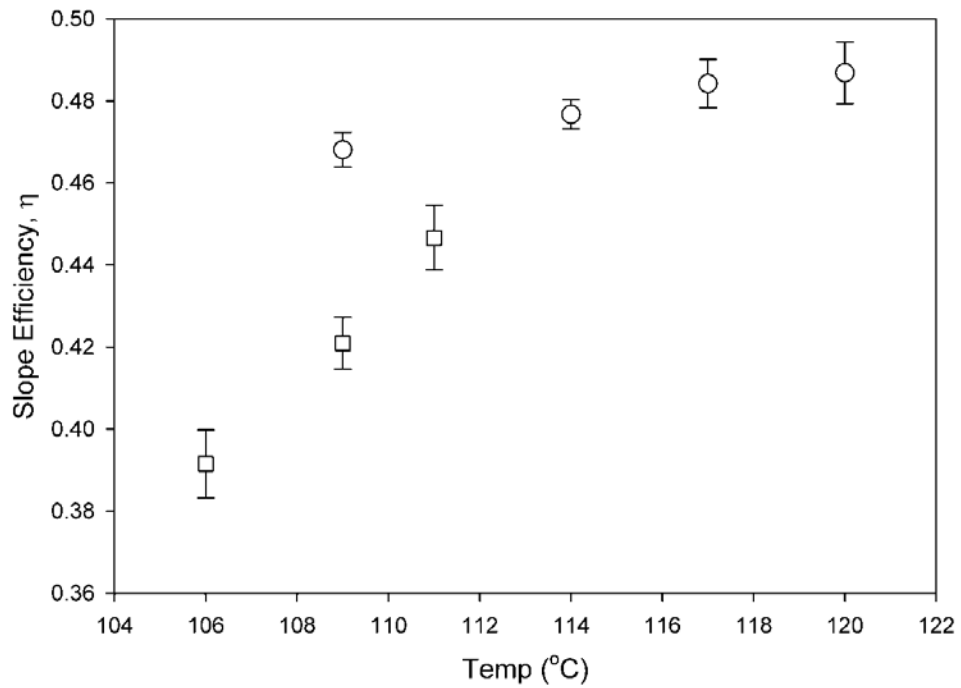


**Figure 19. Slope efficiency for (○) 32% output coupler and (▢) 23% output coupler.**

Despite the cluster of similar results in Figure 16 and Figure 17, a significant dependence on gain cell temperatures and resonator conditions is observed.  Note that the slope efficiency for the 32% output coupler appears to approach a limiting value near 50%. This limit is just below the product of the quantum efficiency, $\eta_{qe} = 0.98$, and the mode overlap, $\eta_{mode} = 0.56$.  With higher output coupling (lower reflectivity), the slope efficiency is somewhat reduced.  A nonlinear response at high pump intensities is observed in the 379 K data in Figure 17.  The curvature in the data is a result of laser output power being limited by concentrations of either alkali or spin-orbit gas.  Future experiments will attempt to determine whether an increase in spin orbit gas or alkali concentration will eliminate the curvature under similar conditions.

**Discussion**

Interpretation of the present results is aided by the recently reported analytical model for DPAL systems by Hager et al.[8]  The quasi-two level limit for narrow band, cw excitation represents ideal performance and the output intensity, $I_{lase}$,  is predicted as:

$$I_{lase} = \eta_{slope} \left( I_{Pin} - I_{th} \right)$$
(6)

where  $I_{Pin}$  is the pump intensity and $I_{th}$ is the pump intensity to reach lasing threshold. The slope efficiency is developed as:

$$\eta_{slope} = \eta_{qe}\eta_{mode} \left( \frac{1-r}{rt} \right) \left[ \frac{\left(1 - e^{2g_{31}l_g}\right)}{\left(e^{g_{th}l_g} - 1\right)\left(t^2 e^{g_{th}l_g} + 1\right)} \right]$$
(7)

where

$r$ = output coupler mirror reflectivity (23% or 32%)

33

$t$ = polarizing beam splitter window transmission (~95%)

$g_{th}$ = threshold gain (loss) coefficient = - $ln(rt^4)/2l_c$

$l_g$ = gain length = 12.7 cm

$l_c$ = cavity length = 40 cm

      The absorption in the presence of lasing is dependent on both alkali concentration

and cavity losses:

$$g_{31} = -\sigma_{31}n \left[ \frac{\left(1-e^{-\theta}\right) - \frac{g_{th}}{\sigma_{21}n}\left(1+3e^{-\theta}\right)}{\left(1+e^{-\theta}\right)} \right] \tag{8}$$

where

$\sigma_{13} = 2\sigma_{31}$ = cross-section for absorption on the pump, $D_2$, transition

$\sigma_{21}$ = cross-section for stimulated emission on lasing, $D_1$, transition

$n$ = total Rb concentration

$\theta = \Delta E_{32}/kT$

$\Delta E_{32}$ = spin orbit splitting $=237\ cm^{-1}$

$k$ = Boltzmann's constant

      In the quasi-two level limit, the population ratio in the pumped, $n_3$, state relative

to the population in the upper laser level, $n_2$, is determined by the detail balance ratio

$n_3/n_2 = 2e^{-\theta} = 0.82$ near $T = 373\ K$.

      The slope efficiencies reported in Figure 19 can be recast in terms of the fraction

of the incident photons absorbed. An analytic model for DPAL performance [8] based on

the quasi-two level approximation, where very fast spin-orbit relaxation rate produces a

statistical distribution between the pumped and upper laser levels, predicts the absorbance

on the pump transition, $A$, as:

$$A \equiv \ln\left(1 - \frac{\eta_{slope}}{\eta_o}\right) = -2\sigma_{13}l_g n\left(\frac{1-e^{-\theta}}{1+e^{-\theta}}\right) + 2g_{th}\frac{\sigma_{13}}{\sigma_{21}}l_g\left(\frac{1+3e^{-\theta}}{1+e^{-\theta}}\right)$$
(9)

Where the limiting value of the slope efficiency is defined as

$$\eta_o = \eta_{qe}\eta_{mode}\left(\frac{\left(\frac{1-r}{rt}\right)}{\left(e^{g_{th}l_g}-1\right)\left(t^2 e^{g_{th}l_g}+1\right)}\right) = 0.46 - 0.49$$
.
(10)

Figure 20 illustrates the linear dependence of absorbance on alkali concentration. The

rubidium concentrations are predicted from the Rb finger wall temperature using the

known vapor pressure curves.[2] At T=382 K the concentration is 1.05 x $10^{13}$ atoms/cm$^3$.

The error bounds for the absorbance grow dramatically as the slope efficiency approaches

the limiting value $\eta_o$. By constraining the data for both output couplers to share a

common slope and constraining $\eta_o = 0.49$, the effective absorption cross-section of

$4.5 \pm 0.5$ x $10^{-14}$ cm$^2$ is obtained. This absorption cross-section is about 7 times less than

predicted by the Lorentzian profile in Figure 12.
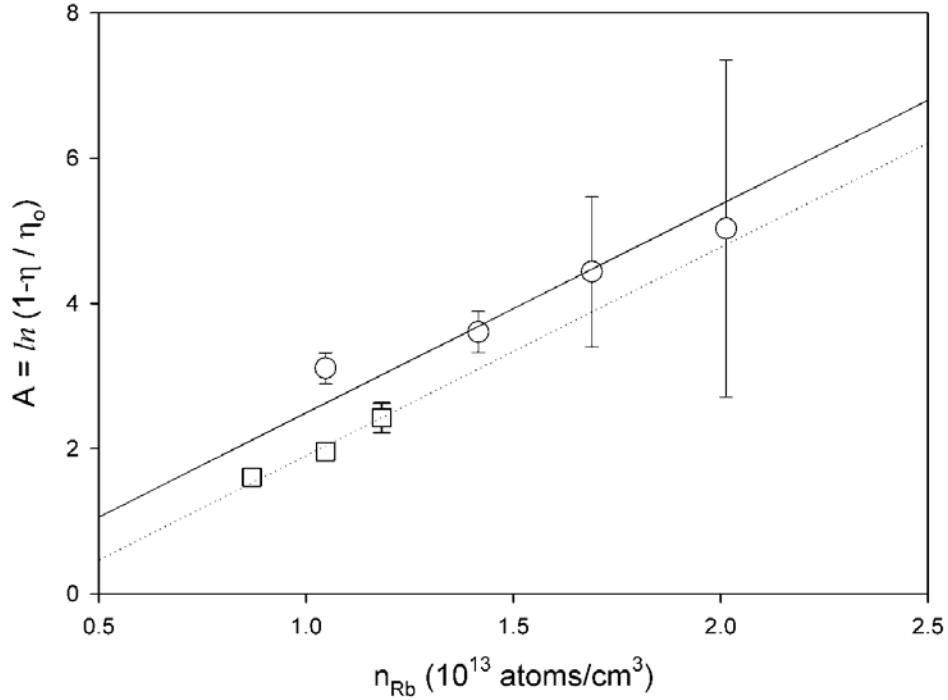
**Figure 20. Slope efficiency reinterpreted as absorbance for (○) 32% output coupler and (□) 23% output coupler.**

Several factors may contribute to this discrepancy. First, the broadband nature of the pump source must be averaged across the absorption feature. For the spectral shapes presented in Figure 12, the average cross-section is reduced by a factor of two from the peak. However, the averaging would be significantly modified by bleaching in the presence of lasing and a thorough analysis of the absorbance under broadband excitation for the DPAL system is required. Secondly, the measured wall temperature may over-estimate the vapor pressure. Indeed, a 10 C variance in temperature would lead to a factor of two change in vapor pressure.[2] Third, the temporal dynamics of this pulsed system produces a temporally evolving efficiency, as shown in Figure 15. Finally,

localized heating within the pumped volume could produce decreased concentrations of both alkali and spin-orbit relaxer on axis, leading to reduced output energy.

The two intercepts in Figure 20 yield threshold gains of $g_{th}$ = 0.004 and 0.010 cm$^{-1}$ for the 32% and 23% output couplers, respectively. These threshold values are less than the expected values of 0.014 – 0.018 cm$^{-1}$ for no transmission losses, $t = 1$. Although the absolute values of the thresholds deviate from the predicted values, the difference for both the predicted and measured values are similar. Threshold is more directly evaluated in Figure 21, where the dependence on alkali concentration is predicted as:[8]

$$I_{th} = I_{ref}\left(\frac{n}{n_o} + \frac{g_{th}}{\sigma_{21}n_o}\right) \qquad (11)$$

where the reference intensity is related to the spontaneous emission and fraction of observed photons as:

$$I_{ref} = \left[\left(\frac{h\nu_p}{\tau}\right)l_g n_o\right]\left(\frac{1+2e^{-\theta}}{2\left(1+e^{-2\theta}\right)}\right)\left(\frac{1}{1-e^{2g_{31}l_g}}\right) = 0.78 - 0.97 \; kW/cm^2 \qquad (12)$$

and

$\tau$ = averaged radiative lifetime for the $^2P_{3/2,1/2}$ manifold = 27 ns

$n_o$ = reference Rb concentration = 1 x 10$^{13}$ atoms/cm$^3$

$h\nu_p$ = pump photon energy = 1.6 eV

A plot of the observed thresholds as a function of Rb concentration is shown in Figure 21.
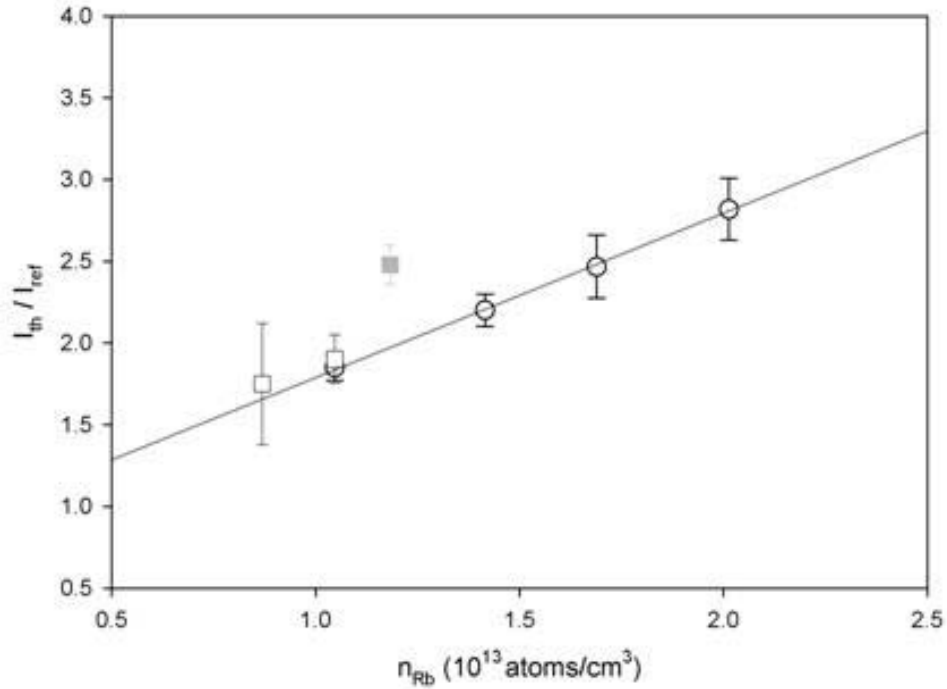
**Figure 21.** **Threshold pump intensities for (○) 32% output coupler and (□) 23% output coupler.**

The shaded data point in Figure 21 was from a data collection set with very high

uncertainty associated with the threshold value, and was excluded while interpreting the

data. To achieve a unit slope, the reference intensity must be reduced by 67%. This

result is consistent with a reduction of the on-axis Rb concentration (reduced effective

absorption cross-section) observed from the analysis of the slope efficiencies. The

common intercept of the 32% output coupler data in Figure 21 is consistent with a

threshold of $g_{th} = 0.066$ cm$^{-1}$, corresponding to a transmission loss at each surface of the

beam splitter of $t = 0.89$. There is insufficient data to determine $g_{th}$ for the 23% output

coupler.

**Conclusions**

Scaling of pump intensity for pulsed laser excitation of a rubidium $D_2$ laser to 32.8 times threshold has been achieved while maintaining a linear response in output intensity. Threshold losses are reduced to ~ 3%, a significant improvement from previously achieved threshold losses of 7 – 50%. No evidence for second order kinetics is evident and near ideal performance is achieved, with the exception of mode overlap. That is, no deviation from linear scaling with pump intensity is observed. Beam spot sizes are critical to assessing laser performance and reports of power scaling without intensity information are often difficult to evaluate.

Slope efficiency, expressed as absorbance, scales linearly with alkali concentration. The quasi-two level analytic model accurately represents the data; however the effective cross-section is 7 times smaller than anticipated. We recommend several efforts to resolve this discrepancy: (1) the development of a pulsed laser model that includes the effects of broad band excitation similar to the CW model presented by Beach et al.[5], (2) measurements of the alkali concentration within the pumped volume, and (3) examination of the temporal dynamics with resolution sufficient to examine the bleaching dynamics. The DPAL system continues to perform near the ideal limit, even for the scaled conditions currently presented.

## IV. Temporal Dynamics of an Optically Pumped Pulsed Alkali Laser at High Pump Intensity

### Introduction

The Diode Pumped Alkali Laser (DPAL) system originally demonstrated by Krupke is a three level laser pumped by diode bars on an alkali's $D_2$ transition, exciting the first $^2P_{3/2}$ state of the alkali atom [11, 5]. Collisional relaxation to the $^2P_{1/2}$ state is accomplished with a spin orbit relaxing gas such as ethane or methane, while pressure broadening of the absorption line has routinely been accomplished with He. The excited alkali atom then lases on the $D_1$ line back to the ground state. Terminating the laser level at the ground state requires the gain volume to be fully bleached before achieving an inversion between the $^2P_{1/2}$ and $^2S_{1/2}$ states, resulting in threshold values of ~1 kW/cm$^2$ [16, 42, 18, 43, 8].

Early laser demonstrations achieved laser output powers of 1-3 W in both rubidium and cesium with slope efficiencies as high as 82% [16, 42, 18]. These early demonstrations also reported problems with soot deposition on the gain volume windows due to an interaction between the ethane or methane when temperatures were over 393 K driving research into carbon free spin orbit relaxing gases [44]. Alkali lasers using He$^4$ or He$^3$ as the spin orbit relaxer and pressure broadening gas have been demonstrated with both rubidium and potassium [44, 36, 52]. More recently cw output powers as high as 145 W with in-band slope efficiencies of 28% have been reported [53]. Additionally, our recent work with a similar laser system achieved linear performance while pumping 32.8 times the threshold value [30].

Achieving optimum performance in a DPAL device requires the spin orbit relaxation rate be much faster than the pump excitation rate. Most reported DPALs experiments have been operated under these conditions. The most notable exception is a high power experiment that exhibited a linear slope efficiency when the pump duration was 0.1 s, yet under CW conditions, output power was drastically reduced [40]. While the cause of this degradation is unknown, lower alkali and spin orbit gas concentrations driven by on axis heating of the gain volume would exhibit a similar behavior [48].

A three-level model for DPAL performance has been developed [8] extending the early model by Beach et al.[5] and applied to a broadband, pulsed potassium laser [54]. Most prior DPAL demonstrations have not been extensively characterized to benchmark the model. Recently, the model was validated with respect to the scaling of alkali concentration for a Rb laser [30]. In the present work we show the model is capable of predicting the temporal dynamics of the laser at high pump intensity and poor spin-orbit relaxation conditions with a single set of device parameters. The characterization of slope efficiency and threshold is accomplished with the results from a single pulse and reveal the effects of bottlenecking.

We also observe the Rb laser performance is dramatically improved with the addition of helium, even when the pressure broadening rate is held constant and the spin-orbit relaxation rate is reduced. These results are quantitatively interpreted as improved thermal transport when helium is present.

**Experimental Setup**

       A frequency doubled Nd:YAG laser (Photonics Industries DML-100 or a Quantronix Eagle) pumped cryogenically cooled KML Ti:Sapphire laser was the excitation source for a rubidium laser, as illustrated in Figure 22.
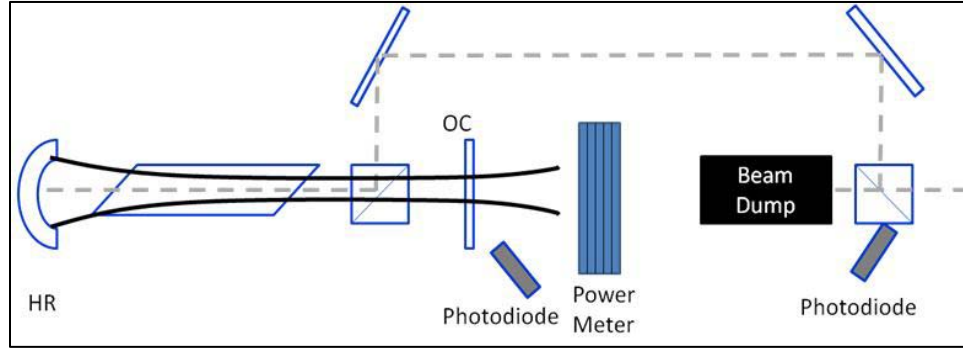


**Figure 22.  Experimental setup.**

       The Ti:Sapphire laser produced ~100 ns pulses, at a 10 kHz repetition rate with an average power of up to 20 W.  The power delivered to the alkali cell was adjusted by rotating the polarization of the pump beam with a half wave plate relative to the polarizing beam splitter in the laser cavity and was varied between threshold ($< 100$ mW) and 3.5 W, or $0 - 0.35$ mJ/pulse. The spectral widths of the Ti:Sapphire when pumped by the DML-100 and Nd:YAG were measured with a Yokogawa AQ6370 optical spectrum analyzer as 44-54 GHz and 34.5 GHz respectively, and were spectrally broad compared to the pressure broadened absorption features which varied between 11.8 GHz and 15.7 GHz.  The bandwidth while incorporating the DML-100 pump source is shown in Figure 23.
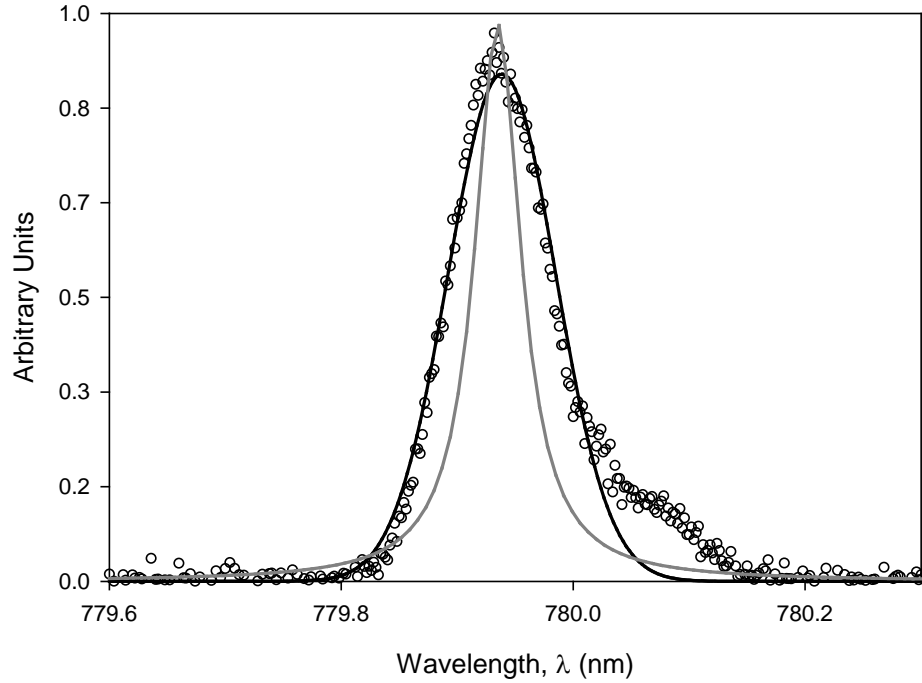
**Figure 23.  Bandwidth of (○) Ti:Sapphire pump when DML-100 green pump source was used with  ~ 42 GHz wide (-) Gaussian and a (-) Lorentzian with a typical pressure broadened absorption line.**

A 12.7 cm long Brewster angled glass cell 2.5 cm in diameter contained the rubidium vapor and was housed in an aluminum oven to provide temperature control. The glass cell contained a rubidium stem attached to the bottom which housed the rubidium and was independently heated from the oven.  The temperature of the stem drove the number density of the alkali in the gain volume, which was held at a temperature $3^{o}$C higher than the stem to prevent rubidium condensation on the quartz windows.  The stem temperature was varied between $80^{o}$C and $120^{o}$C.  To explore the DPALs model robustness, the types and concentrations of both spin orbit relaxing gases and pressure broadening gases were varied.  Either ethane or methane was used as both the spin orbit gas and pressure broadening gas with pressures between 450 Torr and

43

600 Torr.  A combination of ethane and helium was used with a helium pressure of 200 Torr to provide some pressure broadening and methane pressures of either 300 Torr or 450 Torr to both pressure-broaden the absorption line and spin orbit couple the $^2P_{3/2}$ and $^2P_{1/2}$ states.

The rubidium laser cavity was 0.4 m long and was formed by a high reflector with a 0.5 m radius of curvature and a flat output coupler with either, 20%, 23%, 32%, 50%, or 70% reflectivity.  Pump beam spot sizes were recorded with a Newport LBP-HR beam profiler just before the laser cavity for the DML-100 and Nd:YAG were 0.09 cm and 0.11 cm respectively.  The alkali laser beam spot sizes were recorded for both experimental setups at several locations and as expected diverged after the output coupler mirror and were used to estimate the pump and laser mode overlap.

The pump laser wavelength was centered on the $^2S_{1/2} - {}^2P_{3/2}$ (780 nm) transition by maximizing the ratio of the 780 nm and 795 nm ($^2P_{1/2} - {}^2S_{1/2}$) fluorescence from a separate rubidium vapor cell at $80^{\circ}$C using an Ocean Optics USB4000 spectrometer.  The average pump power was recorded with a Ophir model L30A-SH-V1 power meter between the polarizing beam splitter and the rubidium cell.  When pumping with the Nd:YAG laser, output power was recorded with the same power meter just after the output coupler and when pumping with the DLM-100 a second L30A-SH-V1 power meter was used in a similar location.  Finally, the temporal characteristics of both the pump and alkali laser beams were simultaneously recorded on an Agilent 1 GHz oscilloscope using two New Focus model 1621 silicon nanosecond photodetectors with a 1 ns risetime.

## Results

### Dependence of Laser Power on Alkali Concentrations

Laser output power as a function of pump input power was recorded with pump powers, $P_{in}$, between threshold and 2 W in 100 mW increments. Thirty different sets of conditions varying either temperature, $T$, output coupler reflectivity, $R_{oc}$, or type and concentration of buffer gases, $P_{Ethane}$ or $P_{He}$ were examined.  In some cases, pump powers above 2 W were used in increments of 500 mW and reached as high as 3.5 W.  Laser performance for several cell temperatures is shown in Figure 24, where $P_{Ethane} = 450$ Torr filled at room temperature and $R_{oc} = 20\%$.
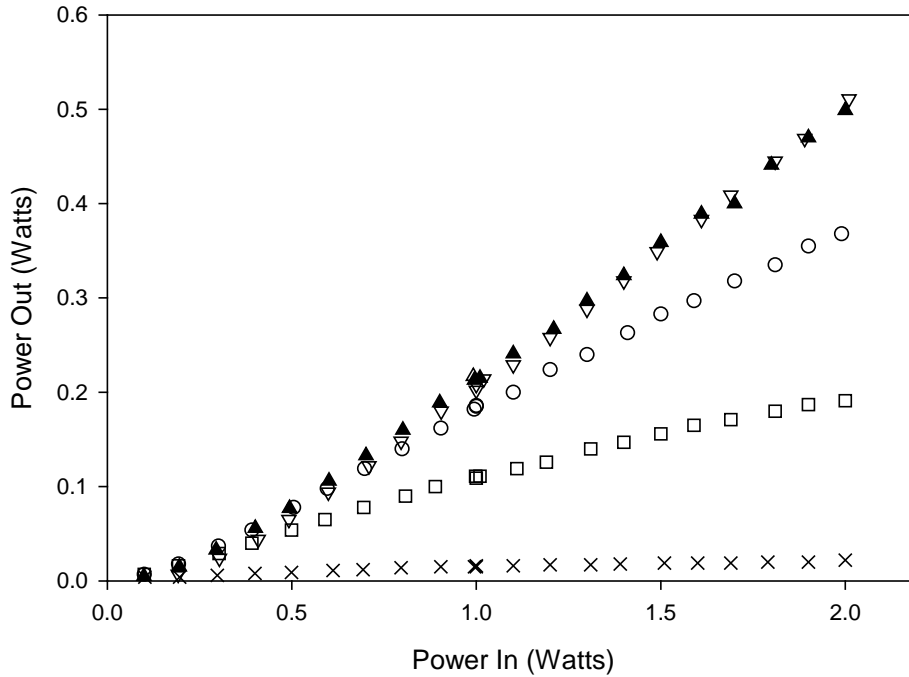


**Figure 24.  Dependence of output power on input power with $P_{Ethane}$=450Torr and $R_{oc}$=20%.  Cell temperatures of (X) 80$^{o}$C, (□) 90$^{o}$C, (○) 100$^{o}$C, (▲) 110$^{o}$C, and (▽) 120$^{o}$C are reported.**

The temperatures of the rubidium finger shown in Figure 24 range from $80^{\circ}C$ to $120^{\circ}C$ in steps of $10^{\circ}C$ resulting in rubidium number densities, $N_{Rb}$, of between $1.5 - 20$ x$10^{12}$ atoms/cm$^3$. Similar results were seen with different values of $R_{oc}$ and $P_{Ethane}$. At the highest temperatures laser performance was degraded near threshold and exhibited curvature in the data which will be discussed in later sections. In all cases when $R_{oc} =$ 20%, at $T=110^{\circ}C$ the rubidium laser reached its asymptotic limit and increasing the temperature further no longer improved slope efficiency and instead degraded performance at lower powers as a result of the threshold value increasing.

**Laser Dynamics**

The temporal profiles of the pump pulse and the rubidium laser pulse were collected at every power setting for all of the various conditions of temperature, output coupler reflectivity, and spin orbit and pressure broadening gas combinations. Representative pulse shapes for both the pump and laser are shown in Figure 25. To effectively compare the pulse shapes of the pump and laser pulse, each was normalized to the energy per pulse derived from the average power measurements. The Rb laser pulse does follow the pump pulse with a FWHM duration of 97 ns. The shape of the pump pulse deviates sufficiently from a Gaussian to justify the use of a six parameter Pearson IV equation shown below,

$$P(T) = a + b\left(1 + \left(\frac{\left(t - \frac{d \times f}{2 \times e} - c\right)}{d}\right)^2\right)^{-e} \times \frac{Exp\left(-f\left(ArcTan\left(\frac{\left(t - \frac{d \times f}{2 \times e} - c\right)}{d}\right) + ArcTan\left(\frac{f}{2 \times e}\right)\right)\right)}{\left(\frac{1 + f^2}{4 \times e^2}\right)^{-e}} \quad (13)$$

For a typical pump pulse, the fit parameters are on the order of, $a = -4.2 \times 10^{-4}$, $b = 5.1 \times 10^{-2}$, $c = 5.5 \times 10^{-8}$, $d = 8.1 \times 10^{-8}$, $e = 2.9$, and $f = -2.1$. At the maximum pump power employed, the system operated with a peak intensity of 32.8 times threshold. The laser pulse reaches threshold at 180 ns with 111 kW of peak power and stays above threshold until 408 ns.
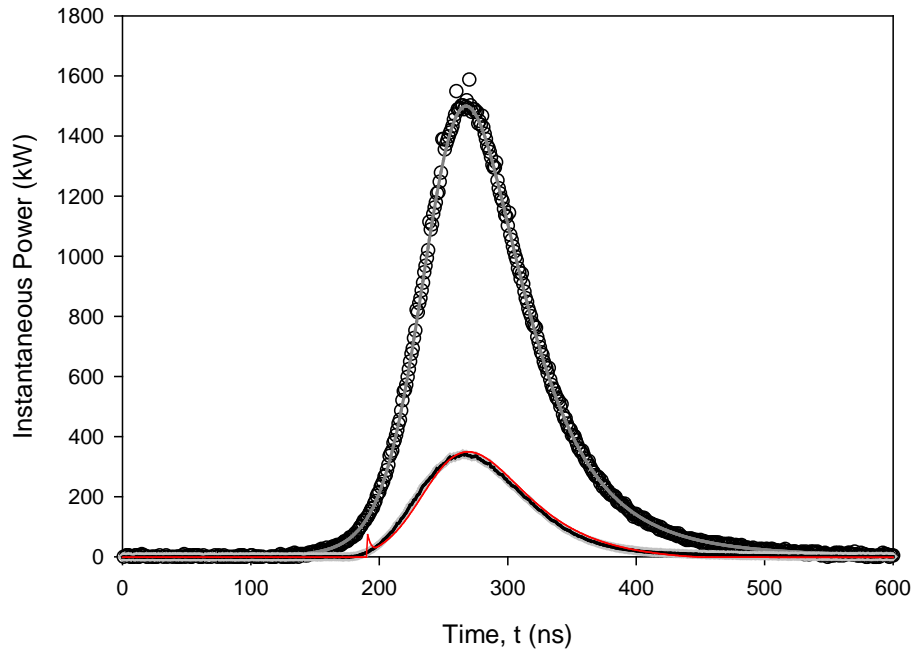


**Figure 25. Temporal profiles of the (○) pump and (▫) laser pulses with $P_{Ethane}$=450 Torr and $P_{He}$=0 Torr and $R_{oc}$=20%, $T$=100°C and $P_{in}$=2 W (0.2 mJ/pulse). Model temporal profiles of (-) pump, (-) laser convolved with detector response, and (-) laser with no convolution**

The pump pulse in the model closely matches the collected pump pulse shape. The output laser pulse calculated from the model is overlaid with the measured laser pulse in Figure 25. Although the model matches the data very well, there is a noticeable deviation between the model and the data in the wings. Initially, the model exhibits a

47

bump which corresponds to the predicted relaxation oscillations, and at the end of the pulse, the model exhibits a faster decay. Both of these deviations are likely due to uncertainty in the detector response function which was not measured.

The instantaneous efficiency, $P_l/P_p$, provides a measure of the temporally changing laser efficiency. Figure 26 demonstrates the temporal dependence of the laser efficiency during the lifecycle of the pump pulse.
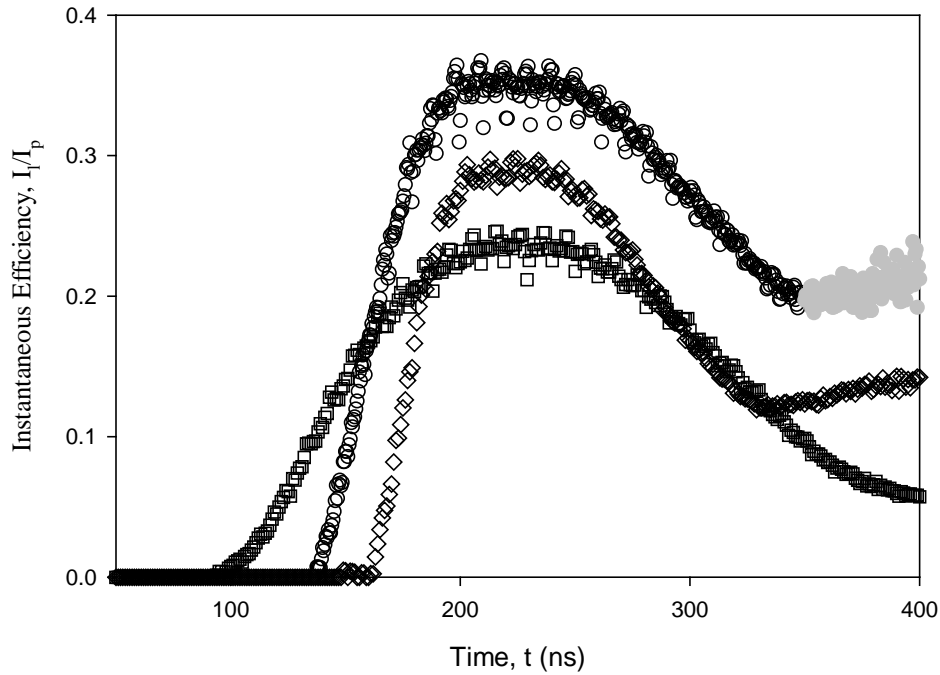


**Figure 26.** (○) **Instantaneous efficiency of the rubidium laser during the lifetime of the pulse pump and (▯) values when the pump is below threshold with $P_{Ethane}$=300 Torr and $P_{He}$=200 Torr and $R_{oc}$=20%, $T$=120°C and $P_{in}$=3.5 W (0.35 mJ/pulse). (▯) 92 ns pump pulse at 150 µJ/pulse, (▯) 166 ns pump pulse at 160 µJ/pulse.**

As the laser pulse turns on, $I_l/I_p$ quickly increases to a limit of 0.353. This is in good agreement with the slope efficiency measurement from a linear fit to the power in vs. power out data set under these conditions of 0.35. The tail end of the $I_l/I_p$ plot does

48

not immediately return to a value of zero and produces numerical artifacts when the pump laser has dropped below the threshold value.  Although the efficiency changes during the lifetime of the pulse, it is clear from Figure 26 that the laser is operating in a quasi steady state regime under these conditions.   Additionally, Figure 26 demonstrates instantaneous efficiency for two pulses which had nearly identical energies per pulse, 0.15 and 0.16 µJ, with varying temporal widths, 92 and 166 ns.  The different pump pulse shape results in a decrease in efficiency with the long pulse.

Just as several of the power in vs. power out plots in Figure 24 deviate from the asymptotic limit of slope efficiency by curving away, the instantaneous efficiency similarly deviates from the limiting value at the highest pulse intensities.  Figure 27 demonstrates the instantaneous efficiencies for several input pump powers, with $P_{Ethane} =$ 600 Torr and $T = 100^{o}C$.  Under these conditions, the efficiency only reaches 23%, less than 35% shown in Figure 26, since the temperature is lower resulting in a lower alkali number density and reducing output power.  At $P_{in} = 2$ W, $I_l/I_p$ reaches a plateau around 0.23, and when $P_{in} = 3$ W, the $I_l/I_p$ plots decrease to 0.18 at the center of the pulse.
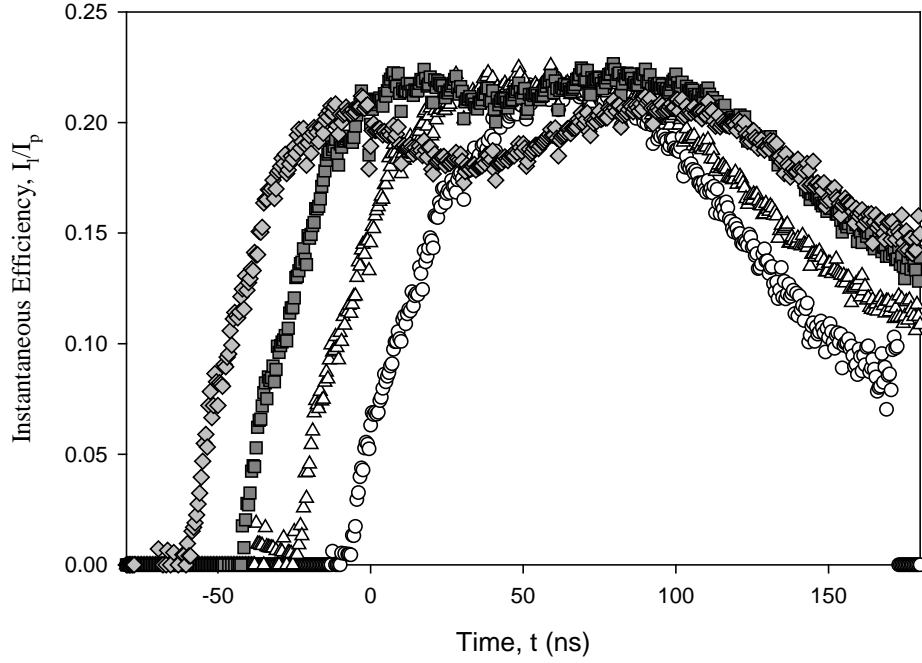
**Figure 27. Instantaneous efficiencies with** $P_{in}$ = (○) **0.5 W,** (□) **1 W,** (△) **2 W, and** (◇) **3 W. Cell conditions of** $T$=100°C, $R_{oc}$=20%, **and** $P_{Ethane}$=600 Torr.

### Three Level Analytic Model

A three-level analytic DPAL model has recently been developed [8] and applied to pulsed potassium[54] and quasi cw rubidium [30] laser demonstrations. This model is adequate to describe all the output laser dynamics observed for the broad range of gain cell conditions in the present study, as discussed below. Application of the model to gain cells with helium buffer gases requires a modification to the alkali concentration and is further interpreted as a thermal effect.

The model uses longitudinally averaged number densities to predict cw or temporally evolving output intensities, including conditions where the spin-orbit relaxation rate limits performance. Determining the number of absorbed pump photons

via the longitudinally averaged pump intensity, $\Omega(t)$, requires the solution of a

transcendental equation:

$$\Omega(t) = \left( \frac{I_P(t)}{\sigma_{31}(n_3(t) - 2n_1(t))l_g} \right) \left( Exp\left( \sigma_{31}(n_3(t) - 2n_1(t))l_g \right) - 1 \right) t_p \left( 1 + t_p^2 r_P Exp\left( \sigma_{31}(n_3(t) - 2n_1(t))l_g \right) \right) \tag{14}$$

Where the populations in the ground $^2S_{1/2}$ state, $n_1(t)$, pumped $^2P_{3/2}$ state, $n_3(t)$, and

upper laser $^2P_{1/2}$, $n_2(t)$, are implicitly a function of the pump intensity and specified by

the standard laser rate equations:

$$\frac{dn_1}{dt} = \sigma_{31}(n_3 - 2n_1)\frac{\Omega}{hv_p} + \sigma_{21}(n_2 - n_1)\frac{\Psi}{hv_L} + n_2\Gamma_{21} + n_3\Gamma_{31} \tag{15}$$

$$\frac{dn_2}{dt} = -\sigma_{21}(n_2 - n_1)\frac{\Psi}{hv_L} + \gamma_{mix}(n_3 - 2Exp(-\theta)n_2) - n_2\Gamma_{21} \tag{16}$$

$$\frac{dn_3}{dt} = -\sigma_{31}(n_3 - 2n_1)\frac{\Omega}{hv_p} - \gamma_{mix}(n_3 - 2Exp(-\theta)n_2) - n_3\Gamma_{31} \tag{17}$$

The material and cavity parameters are defined as:

$t_p$ = window transmission loss per pass
$r_p$ = mirror reflectivity at the pump wavelength
$l_g$ = gain length = 12.7 cm
$I_p$ = incident pump intensity
$\sigma_{31}$ = stimulated emission cross-section for the pump transition
$\sigma_{21}$ = stimulated emission cross-section for the lasing transition
$\Gamma_{21} = 3.61 \times 10^7 \text{ s}^{-1}$ (assumes no quenching)
$\Gamma_{31} = 3.81 \times 10^7 \text{ s}^{-1}$ (assumes no quenching)
$\gamma_{mix}$ = spin-orbit mixing rate = 4.56-9.14 $\times 10^9 \text{ s}^{-1}$ (depending on gas mixture)
$\theta = \frac{\Delta E_{21}}{kT} = 0.91$ at T=376K
$n$ = rubidium concentration = $n_1 + n_2 + n_3 = 0.15 - 2.01 \times 10^{13}$ atoms/cm$^3$

The average intracavity DPAL laser intensity, $\Psi$, is amplified via stimulated emission

from the spontaneous noise and limited by output coupling and cavity losses:[9]

$$\frac{d\Psi}{dt} = 0 = \left( rT^4 Exp\left[ \left( \sigma_{21}\left( n_2(t) - n_1(t) \right) 2l_g \right) \right] - 1 \right)\frac{\Psi}{\tau_{RT}} + \frac{n_2 c^2 \sigma_{21} h\nu_L}{l_g} \tag{18}$$

where

$r =$ output coupler reflectivity
$t =$ transmission loss at the laser wavelength
$\tau_{RT} = 2l_g / c = 2.5$ ns

For broadband excitation, the spectral dependence of the average pump intensity must be

averaged with the absorption lineshape:[8]

$$\Omega = \left( \frac{I_P(t)}{\sigma_{31}\left( n_3 - 2n_1 \right) l_g} \right) \int_{-\infty}^{\infty} f_{Pump}(\nu)\left( 1 - Exp\left( \sigma_{31}(\nu)\left( n_3 - 2n_1 \right) 2l_g \right) \right) t_p \left( 1 + t_p^2 r_P Exp\left( \sigma_{31}(\nu)\left( n_3 - 2n_1 \right) l_g \right) \right) d\nu \tag{19}$$

where

$f(\nu) =$ pump laser lineshape with Gaussian width (FWHM), $\Delta\nu_P = 34 - 54$ GHz
$\sigma_{31}(\nu) = \left( g(\nu)/g(\nu_o) \right)\sigma_{31}$
$g(\nu) =$ sum of Voight lineshapes for hyperfine split D2 line [19] with linewidth, $\Delta\nu_a$

At cell pressures near 1 atmosphere, the absorption lineshape may be approximated by a

single Lorentzian with an error of less the 7% [19]. For the current buffer gas

compositions and pressures, the absorption linewidth is $\Delta\nu_a = 44\text{-}54$ GHz. Figure 23

illustrates the pump laser and absorption lineshapes used in the modeling. A comparison

of the model with the laser output pulse is provided in Figure 25.

The output laser pulse from the model was convolved with a 10ns wide detector response

function to incorporate the effects of the detector on the measured laser pulses.

The model input parameters that are adjusted when attempting to match the observed data are the frequency bandwidth of the pump laser, $\Delta \nu_P$, the alkali number density, $n_{Rb}$, transmission through the polarizing beam splitter, $t$, mode overlap between the pump and laser, $\eta_{mode}$, and the beam waist of the pump, $\omega_o$. From experimental measurements, approximate values for all of these parameters are known, and only small deviations are required to match the model with the experimental data. The expected values for all of these parameters along with the values used in the model are shown in Table 8.

**Table 8.   Laser performance parameters (no helium).**

| Parameter | Symbol | Expected Value | Modeled Value |
|---|---|---|---|
| Frequency bandwidth | $\Delta \nu \left( \text{GHz} \right)$ | 44-54 | 100 |
| Alkali number density | $n$ | Derived from cell temperature, $T$ | $T \pm 3^\circ \text{C}$ |
| Transmission through PBS | $t$ | 0.96 | 0.99 |
| Mode overlap | $\eta_{mode}$ | 0.58 | 0.405 |
| Pump beam waist | $\omega_o \left( \text{cm} \right)$ | .085 | .095 |

**Instantaneous Efficiency**

An alternative approach to analyze the temporal profiles involves correlating the pump profiles and laser profiles at each instant. Analyzing the data in this way provides a slope efficiency curve which increases as the pump power grows, and then decreases as the pump power returns to zero. Analyzing a single set of pulse shapes allows rubidium

laser performance measurements from threshold through the peak power in the pulse.

Figure 28 compares the instantaneous slope efficiencies of the collected data to the model

for the following conditions: $P_{Ethane} = 450$Torr, $R_{oc} = 20\%$, $T = 100^{\circ}$C, and $P_{in} = 1.99$W.
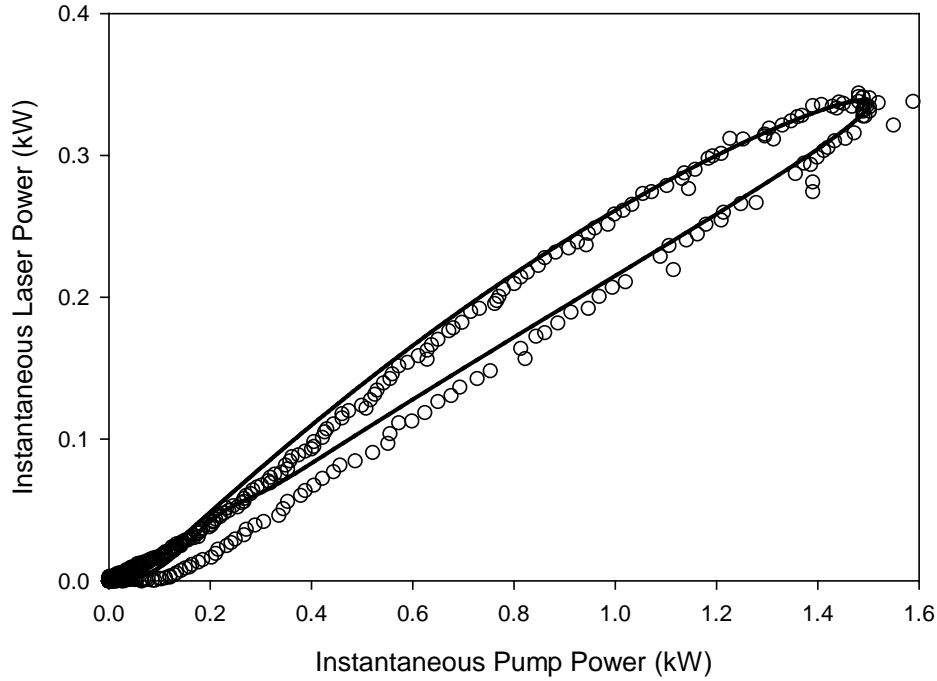


**Figure 28.  Instantaneous laser power vs. pump power for the model (-) and data (○).**

Note that in both the model and the data, the slope efficiency curves do not return to zero

along their initial paths.  This is due to the cavity photon buildup time,  ~7 ns, which

results in a delay between transferring pump energy into laser energy.  When a 5 ns

photon buildup is incorporated to the pump pulse, the slope efficiency curve returns to

the origin along its initial path as shown in Figure 29.
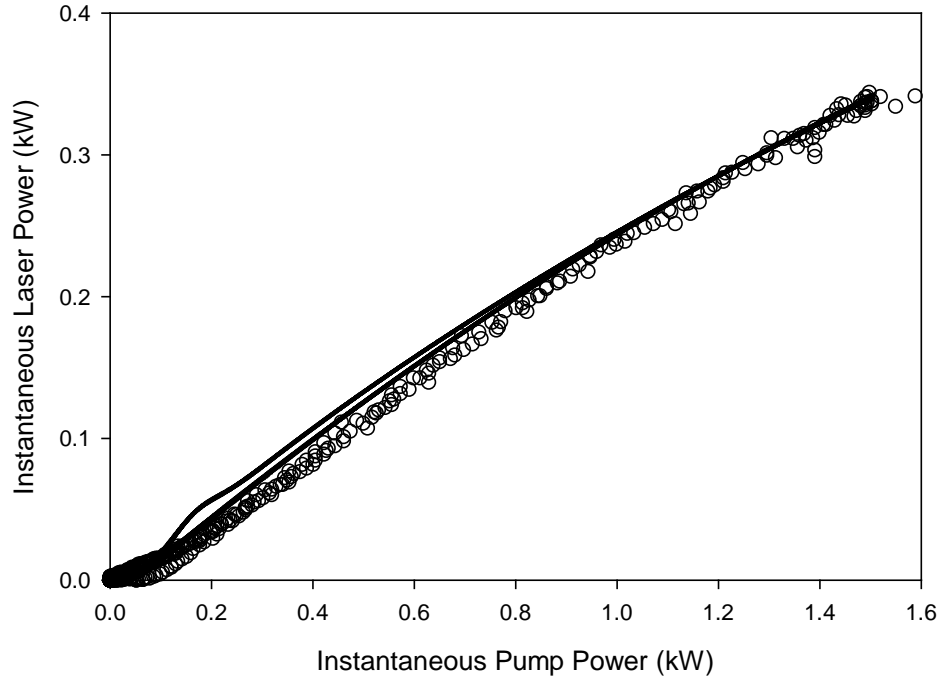
**Figure 29. Instantaneous laser power vs. pump power for the model (-) and data (○), with a 5 ns delay of the pump pulse.**

Figure 30 demonstrates the instantaneous laser power as a function of instantaneous pump power for identical conditions at two different average input pump powers, and the lower power data is consistent with the initial higher power data. Since the lower power case is consistent with the higher power, the three-level model must only be validated with the highest powers collected.
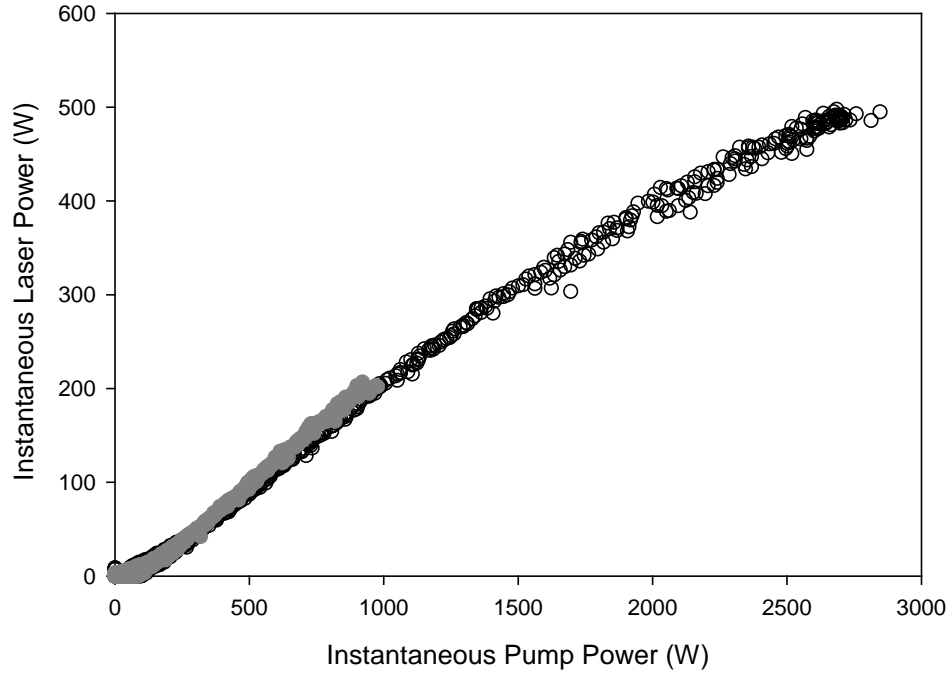
**Figure 30.  Instantaneous laser power vs. pump power with (●)1 W and (○)3 W of average pump power.**

Figure 31 compares the experimentally determined instantaneous slope efficiencies to the predicted model results using the parameters presented in Table 8with four sets of operating conditions varying cell temperature, ethane pressure, and output coupler reflectivity.  For all four conditions presented, the model performs reasonably well.  For the 90°C data case, the model begins to diverge from the collected data.  We believe this is a result of the model variable parameters masking the thermal loading that is occurring in the gain medium, so that at low alkali concentrations the ability of the parameters to account for thermal loading is decreased.
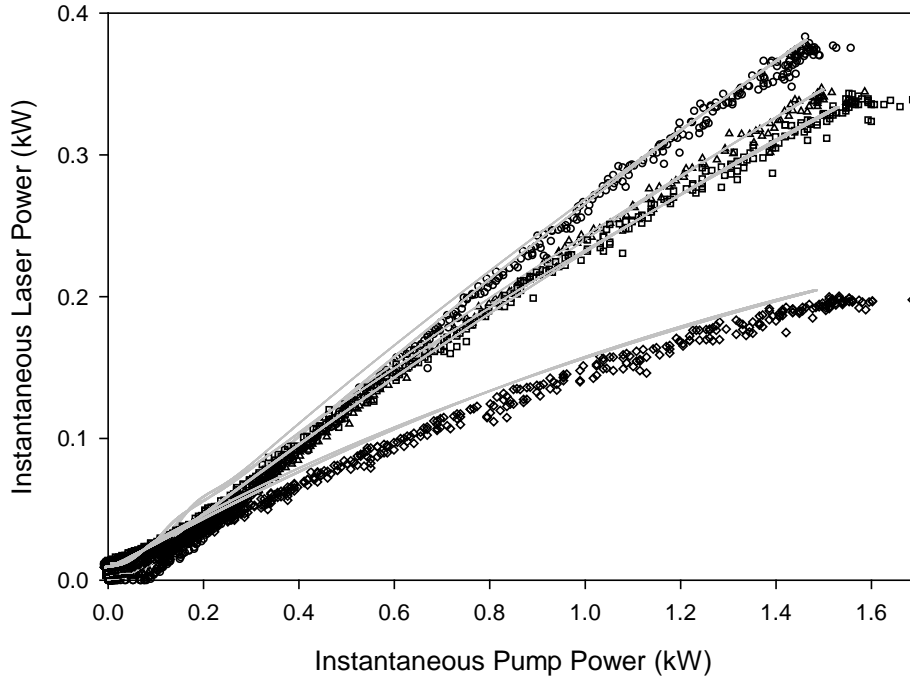
**Figure 31.  Instantaneous laser power vs. pump power data compared to model results ($\square$) for the following conditions,  ($\circ$) $P_{Ethane}$ = 600 Torr, $R_{oc}$=20%, $T$=100$^o$C, ($\square$) $P_{Ethane}$ = 450 Torr, $R_{oc}$=20%, $T$=100$^o$C,  ($\square$) $P_{Ethane}$ = 450 Torr, $R_{oc}$=50%, $T$=100$^o$C,  ($\square$) $P_{Ethane}$ = 600 Torr, $R_{oc}$=20%, $T$=90$^o$C.  All cases used the same model fit parameters from Table 8.**

### Laser performance increase with helium

Four sets of conditions were analyzed to determine buffer gas effects on laser performance using the DML-100 pump laser.  The four combinations of spin orbit and pressure broadening gases are provided in Table 9.

**Table 9. Buffer gas pressures, pressure broadened absorption line, and efficiencies for data presented in Figure 31.**

| | #1(○) | #2(●) | #3(☐) | #4(☐) |
|---|---|---|---|---|
| $P_{He}$ *(Torr)* | 200 | 0 | 200 | 0 |
| $P_{Ethane}$ *(Torr)* | 300 | 450 | 450 | 600 |
| $\Delta \nu_a$ (GHz) | 11.9 | 11.8 | 15.8 | 15.7 |
| $\eta_{peak}$    $T = 120^o C$ | .331 | .297 | .329 | .318 |
| $\eta_{peak}$    $T = 100^o C$ | .239 | .202 | .247 | .208 |

The pressure broadening rates for $C_2H_6$ and He for the $D_2$ line of rubidium are 26.2 and 20.0 MHz/Torr respectively [38, 22]. The resulting homogenous linewidth is ~12 GHz with both $P_{Ethane}$=450 Torr only and the combination of $P_{Ethane}$=300 Torr and $P_{He}$=200 Torr. Similarly, a linewidth of ~16 GHz resulted with the other two sets of buffer gases. With all four buffer gas settings, alkali stem temperatures of 90$^o$C, 100$^o$C, and 120$^o$C were utilized. Yielding $n$ = 0.31-2.01 x10$^{13}$ atoms/cm$^3$. The average output power as a function of pump power is shown in Figure 32 and 33 for T=120 and 100 C respectively. The corresponding instantaneous efficiencies for the highest pump powers are shown in Figure 34.
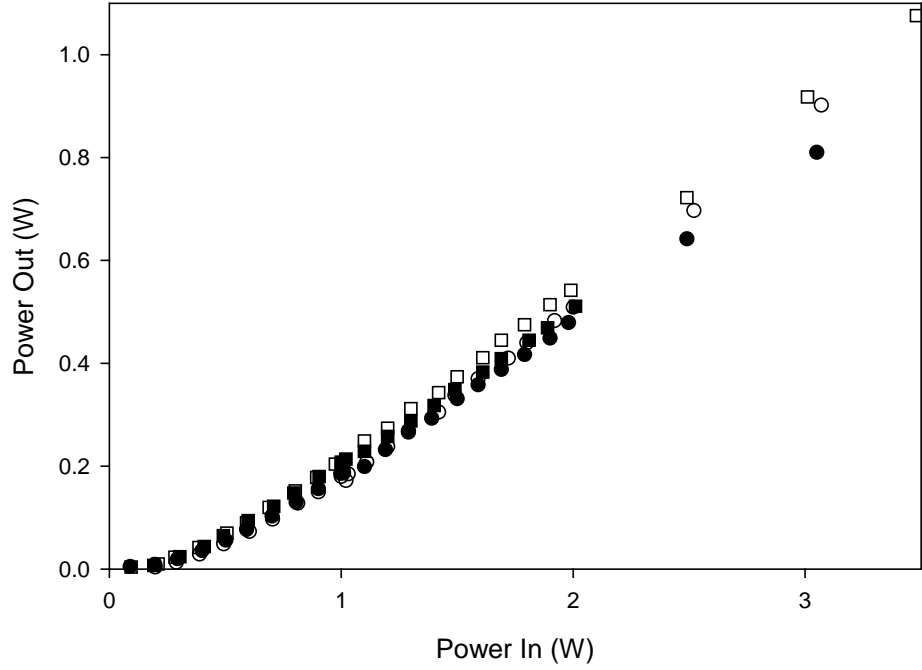
**Figure 32.  Output vs input power at *T*=120C and *R$_{oc}$*=20%.  Buffer gases of (○)300 Torr C$_2$H$_6$ / 200 Torr He, (□)450 Torr C$_2$H$_6$ / 200 Torr He, (●)450 Torr C$_2$H$_6$, and (□)600 Torr C$_2$H$_6$ are shown.**
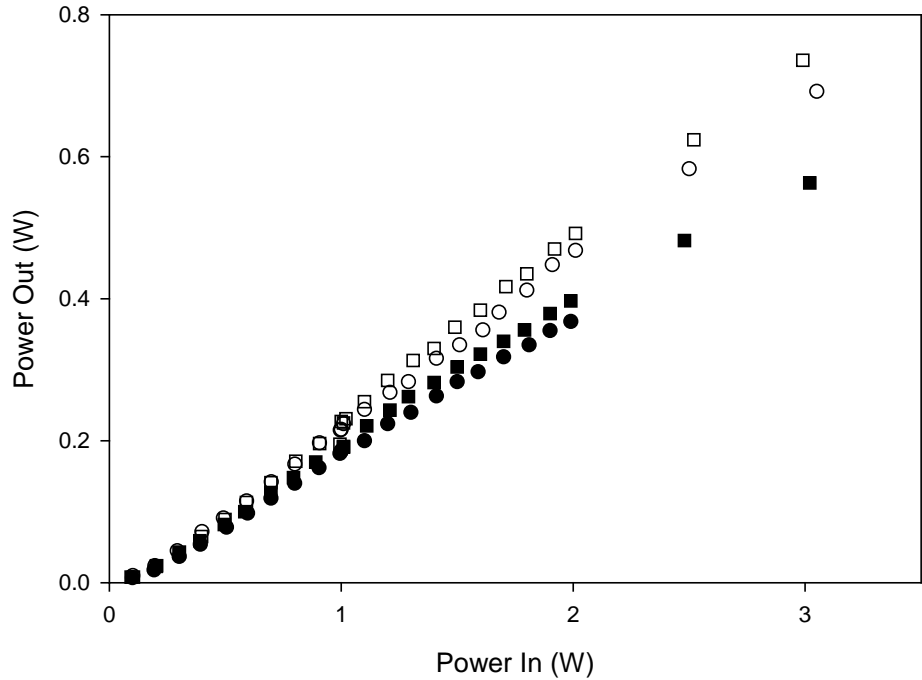


**Figure 33.  Dependence of output power on input power at *T*=100C and *R$_{oc}$*=20%. Buffer gases of (○) 300 Torr C$_2$H$_6$ / 200 Torr He, (□) 450 Torr C$_2$H$_6$ / 200 Torr He, (●) 450 Torr C$_2$H$_6$, and (□) 600 Torr C$_2$H$_6$ are shown.**

Several general observations regarding the rubidium laser performance can be summarized by comparing Figures 31-32. First, output power is less sensitive to buffer gas pressure at elevated alkali concentrations. The system can process more pump photons per second even for a given spin-orbit relaxation rate due to high number of cycling atoms. At lower alkali concentrations, the system bottlenecks due to slow spin orbit relaxation and the output power is sensitive to relaxation rate. Second, for the cases where the broadening and spin-orbit rates are higher (more ethane), the efficiency is improved. The increased cycling rate improves performance more than the minimal decrease in effective absorption cross-section. Third, curvature near threshold conditions is readily evident. Given a spatially distributed pump beam, approximated by a Gaussian, the gain volume is bleached on line center allowing lasing to begin. As pump intensity is increased, the entire pump beam begins to bleach through the gain volume, resulting in an increase of laser power. Fourth, for conditions with the same broadening, but slower spin-orbit relaxation (increased helium) the efficiency increases. This surprising result cannot be described by the present modeling without accounting for thermal effects.

In an attempt to use the three level model [14] to quantify the on axis temperature increase, the model parameters were chosen to provide good agreement with the 300 Torr ethane and 200 Torr helium data, shown in Table 10.

The instantaneous slope efficiency plots for both the data and model are shown in Figure 34 for both the 300 Torr $C_2H_6$ / 200 Torr He combination and 450 Torr $C_2H_6$ alone.

**Table 10. Laser performance parameters (with helium).**

| Parameter | Symbol | Expected Value | Modeled Value |
|---|---|---|---|
| Frequency bandwidth | $\Delta \nu \left( \text{GHz} \right)$ | 44-54 | 100 |
| Alkali number density | $n$ | Derived from cell temperature, $T$ | $T \pm 3^{\circ}\text{C}$ |
| Transmission through PBS | $t$ | 0.96 | 0.99 |
| Mode overlap | $\eta_{\text{mode}}$ | 0.58 | 0.525 |
| Pump beam waist | $\omega_o \left( \text{cm} \right)$ | .085 | .125 |
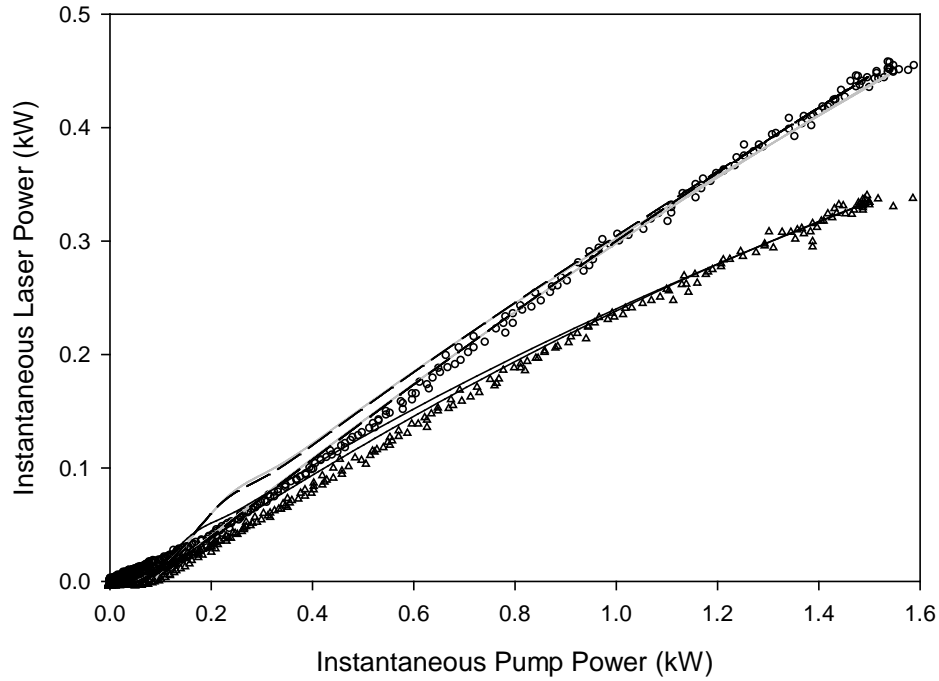


**Figure 34. Instantaneous slope efficiency data compared to model with $T$=100C and $R_{oc}$=20%. Collected data with buffer gases of (○) 300 Torr C$_2$H$_6$ / 200 Torr He, and (△) 450 Torr C$_2$H$_6$ are shown, as well as model results for (—) 300 Torr C$_2$H$_6$ / 200 Torr He, and (--) 450 Torr C$_2$H$_6$, additionally model results for (—) 450 Torr C$_2$H$_6$ incorporating a 62.5% decrease in concentrations of alkali number density and spin orbit gas.**

To achieve agreement between the data and model using the same parameters for the 450 Torr ethane case, the spin orbit coupling rate and the number density of alkali atoms were decreased by 62.5% and the results are shown in Figure 34.  A decrease in number density of this amount results from a density gradient from a temperature increase of $226^{\circ}$C.

A simple heat diffusion model presented by Zhu et al. can also quantify the temperature increase [48].  The steady state heat conductive equation is,

$$\frac{d^2T}{dr^2} + \frac{1}{r}\frac{dT}{dr} + \frac{1}{2T}\left(\frac{dT}{dr}\right)^2 + \frac{q_v}{\kappa} = 0 \tag{20}$$

Where $\kappa$ is the thermal conductivity, and $q_v$ is the heat power deposited in the volume given by,

$$q_v = \frac{2\alpha\eta P e^{-2r^2/w_p^2} e^{-\alpha(z+L/2)}}{\pi w_o^2} \tag{21}$$

when $r < w_p$ and $q_v = 0$ everywhere else.  $\alpha = 0.12$ is an approximation to the exponential absorption coefficient, $\eta = 0.68$ is the heat conversion coefficient, $z$ is the linear position along the cell, and $w_o = 0.08$ is the pump beam radius.  The radial temperature profile for a cell filled with helium and one filled with ethane is $224^{\circ}$C, shown in Figure 35, demonstrating excellent agreement between the heat diffusion model, and the estimated temperature difference attained from the three-level model.
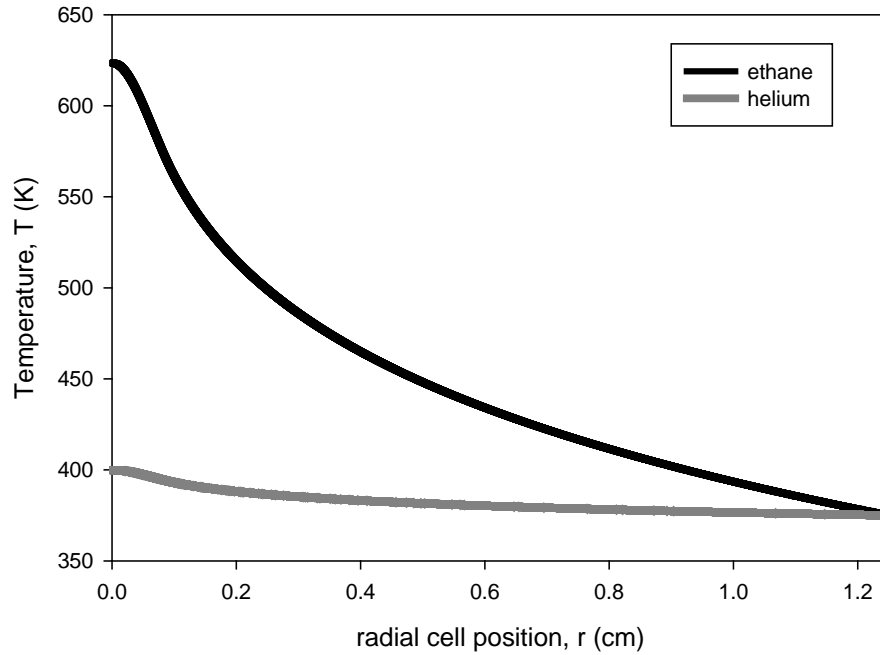
**Figure 35. Buffer gas temperature from heat conduction model, with ethane (●) and helium(●) in the cell.**

**Conclusions**

The temporal pulse shapes of an alkali laser and their behavior under spin orbit and alkali number density limiting conditions have been demonstrated. All laser performance reductions attributed to concentrations of buffer gas or alkali can be reversed by increasing those concentrations, implying no evidence of second order kinetics. The three level DPAL model has accurately represented the collected temporal pulse shape data when only ethane or methane are in the gain medium. However, the model does not predict the increase in laser performance with the addition of helium, potentially due to a reduction in the amount of on-axis heating. The three level model indicated an on axis temperature increase of $226\,^{\circ}\mathrm{C}$ is sufficient to explain the increase in

laser performance between ethane only and ethane helium mixtures.  The temperature

increase is in good agreement with a simple thermal diffusion model under the

experimental conditions.

# V. Blue and Infrared Stimulated Emission from Alkali Vapors Pumped Through
# Two-Photon Absorption

## Introduction

A new class of diode pumped lasers based on excitation of the $D_2$ line and subsequent lasing on the $D_1$ line in alkali atoms is receiving considerable attention.[11] Diode pumped alkali lasers (DPAL) have been demonstrated at 17 W with 53% slope efficiency in rubidium and 48 W (quasi-cw) with 52% efficiency in cesium.[40,41] The lasers typically require: (1) high buffer gas pressures, ~ 1 atmosphere, to match the width of the absorption profile to the spectral lineshape of the diode pump source, and (2) a collision partner such as ethane at pressures of several hundred Torr to relax the population in the pumped $^2P_{3/2}$ state to the upper laser $^2P_{1/2}$ state. The alkali atoms provide high absorption even at low concentration and a single atom may rapidly cycle under intense pump conditions, suggesting high power operation from a small gain volume.

A similar approach has been attempted using multiple lasers to sequentially pump excited states of rubidium and cesium with the goal of lasing in the blue on the $(n+1)^2P_{3/2, 1/2} \rightarrow (n)^2S_{1/2}$ transitions.[4,24] Two low power cw diode lasers, one tuned to the $D_2$ line in cesium $6\,^2S_{1/2} \rightarrow 6\,^2P_{3/2}$ at 852 nm, and the other to the $6\,^2P_{3/2} \rightarrow 6\,^2D_{5/2}$ transition at 917 nm yields a ~ 4 μW blue beam at 455 nm on the $7\,^2P_{3/2} \rightarrow 6\,^2S_{1/2}$ transition.[24] Cascade through the infrared $6\,^2D_{5/2} \rightarrow 7\,^2P_{3/2}$ at 15.1 μm presumably completes the pump cycle. Such a source might find application for laser

communications through water,[21]  however, the two wavelength pump requirement

adds complexity to the system.

Lasing without inversion (LWI) has been demonstrated in rubidium via both a V-

type and sequential double resonance processes.[51,15,50,1]  In the sequential double

resonance experiment, two 20 mW lasers at 780 and 776 nm produce a blue beam with

power up to 40 μW by coherently coupling the 5S state with the 5P and 5D states.

Detuning the 780 nm pump from the F" = 3 → F'=4 resonance by about 2 GHz allows for

higher alkali concentration and maximizes the conversion efficiency at about 0.1%.[15]

A collimated infrared field at 5.5 μm arising from the $5\,^2D_{5/2} \rightarrow 6\,^2P_{3/2}$ transition is

affected only marginally by the blue beam, but the blue field occurs only when the

infrared field is present.[50]  Most recently, four wave mixing as the mechanism

responsible for the blue light generation and the required phase matching conditions has

been presented.[1]

The infrared transitions are more easily inverted.  Continuous-wave lasing

without a resonator was demonstrated in 1981 for both Rb and Cs at 1.3 – 3.1 μm by

pumping in the blue on the second resonances, Rb $5\,^2S_{1/2} \rightarrow 6\,^2P_{3/2,1/2}$ and Cs $6\,^2S_{1/2} \rightarrow 7$

$^2P_{3/2,1/2}$.[25]  Lasing on 16 different IR lines was observed. The infrared gain-length

product was about 30 and the beam divergence was about 10 mrad.[25]

Another type of infrared alkali atom laser has been demonstrated based on energy

transfer for optically excited alkali dimers.[32,26]  For example, broadband absorption to

repulsive electronic states in the $Cs_2$ yields prompt dissociation and the production of the

Cs $5\,^2D_{5/2,\,3/2}$ states. Lasing has been achieved at 3.01 and 3. 49 μm on the $5\,^2D_{5/2} \rightarrow 6$

$^2P_{3/2}$ and $5\,^2D_{3/2} \rightarrow 6\,^2P_{1/2}$ transitions, respectively.[26]  Narrow band absorption at the

same pump wavelength, 584.5 nm, can produce the highly excited 9 $^2D_{5/2}$ state.

Subsequent laser emission can be achieved at 2.43 – 8.66 μm.[26]  This system requires

high alkali temperatures, ~ 500°C, to generate sufficient alkali dimer concentrations.

The present work generates a blue beam using a single red laser tuned to the two photon

absorption excitation of the (n) or (n+1) $^2D_{3/2, \, 5/2}$ and (n+2) or (n+3) $^2S_{1/2}$ states in Rb

(n=5) and Cs (n=6), respectively.  Indeed, lasing is simultaneously achieved in the mid

infrared and blue after excitation in the red via the processes illustrated in Figure 36. The

system operates at low pressure without collisional energy transfer offering minimal heat

load and requires only a single near infrared pump source.  Conversion efficiency in the

blue is similar or better than the prior double resonance experiments. Several mid infrared

lasing transitions in the 2-5 μm atmospheric transmission window are also available.
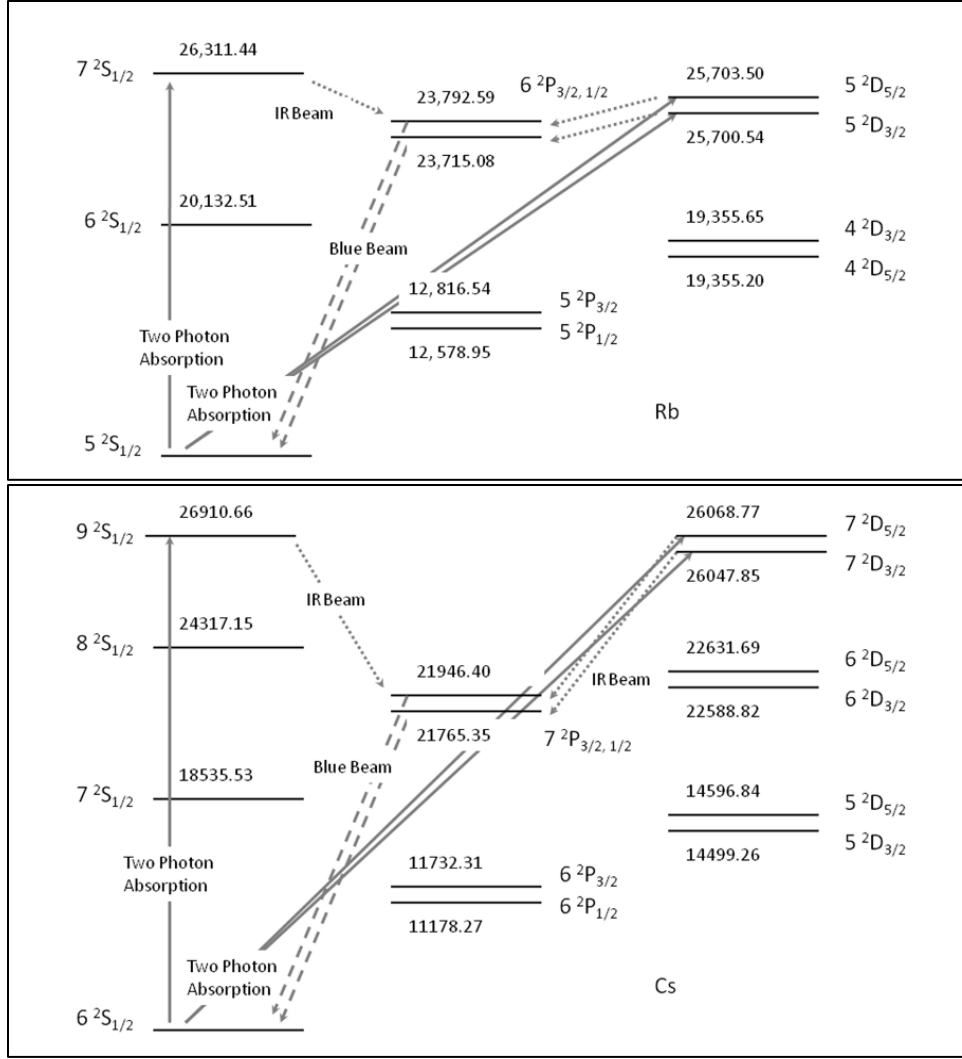
**Figure 36. Energy level diagram and lasing mechanism for (a) Rb and (b) Cs systems.**

## Experimental Apparatus

A schematic diagram of the laser apparatus is provided in Figure 37.
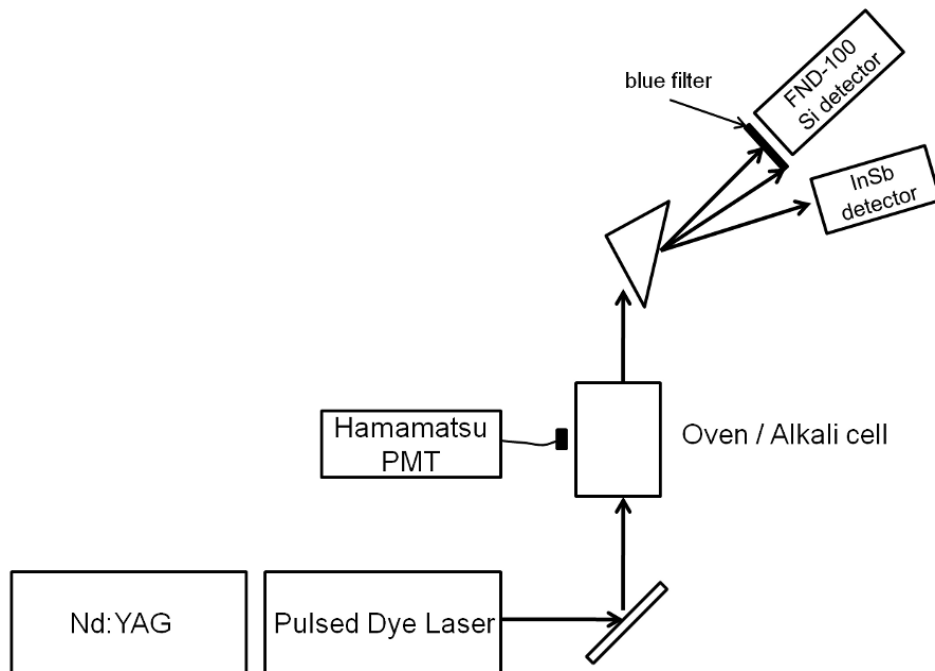
**Figure 37.  Laser apparatus.**

A Spectra Physics Nd:YAG pumped Sirah dye laser with LDS-765 dye provided a
tunable pump source from 745 – 785 nm with up to 100 mJ in 4 ns pulses at 10 Hz and a
bandwidth of ~ 16 GHz.  The pump beam radius of ~ 3.5 mm and < 0.5 mrad divergence
was not a $TEM_{00}$ mode.  A 2.5 cm diameter by 7.5 cm long Triad technologies rubidium
vapor cell with Pyrex windows was heated to 175 – 250 $^{o}$C in an aluminum oven.
Similarly, a 2.5 cm diameter by 5.0 cm long Triad technologies cesium vapor cell with
Pyrex windows was heated to 175 – 200 $^{o}$C.  Both were low pressure cells and contained
no buffer gases. For rubidium, the [87]Rb isotope was employed, while for cesium, the
natural isotopic abundance was used.

The transmitted pump and resulting stimulated beams were dispersed through a
readily available BK7 prism and visually recorded with a Canon G9 CCD camera.  A fast

FND-100 photodiode behind a 500 nm short pass filter recorded the temporal nature of the blue beam on a 1 GHz oscilloscope. Alternatively, a large area silicon detector was employed with Boxcar detection to record laser excitation spectra. The spectral content of the blue beam was examined using a 0.5 m Triax monochromator verifying the blue ASE beams were a result of the $(n+1)^2P_{3/2, 1/2}$- $(n)^2S_{1/2}$ transitions. Average power was measured with a Coherent LM-3 HTD or a Newport 818-SL power meter. Time resolved side fluorescence from both the blue and red $^2P$ – ground $^2S$ transitions was also monitored via a Hamamatsu R943-02 PMT. A single pixel InSb detector was employed to detect the infrared beam for the cesium laser. The cesium cell window, InSb detector response, and IR filter provide an effective band pass of 2.0 – 2.5 μm with peak transmission of > 40%, allowing for detection of the IR beam. The longer wavelengths of the rubidium system are blocked by the cell windows.

**Results**

### Blue and Mid IR Beam Observations

A blue beam with divergence angle of $\theta_{1/2}$ = 6 mrad was observed as the pump laser was tuned through the two photon absorption wavelengths in both rubidium and cesium. A visible image of the blue beam and the transmitted far red pump laser spot recorded after the dispersing prism for the Cs cell is illustrated in Figure 38. The blue beam divergence is larger than the pump beam, < 0.5 mrad, but considerably smaller than the fluorescence divergence of 47 mrad. A mid IR beam was also observed in Cs when the pump laser was tuned to the $7\,^2D_{3/2} – 6\,^2P_{1/2}$ and $7\,^2D_{5/2} – 6\,^2P_{3/2}$ transitions.
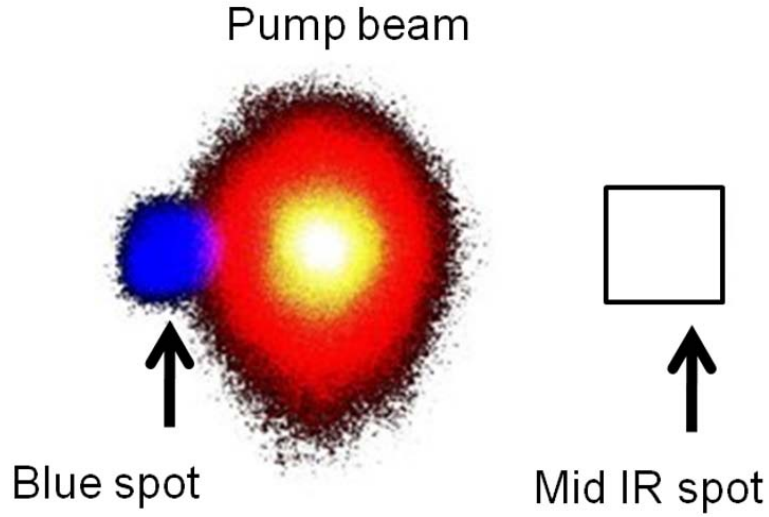
**Figure 38. Dispersed beams for the Cs cell in the forward direction. The pump beam saturates the camera. The mid IR spot was not imaged, but is schematically located by spatially scanning with the point InSb detector.**

The location and extent of the mid IR beam was determined by spatially scanning the InSb detector in the same dispersed image plane. The location of the mid IR beam is schematically overlaid on the image of Figure 38. To ensure the IR beams were near the expected values (2.34 $\mu$m and 2.43 $\mu$m spots for the $7\,^2D3/2 – 6\,^2P_{1/2}$ and $7\,^2D_{5/2} – 6\,^2P_{3/2}$ transitions, respectively) a 2.5 $\mu$m long pass filter was employed and the infrared spot was no longer detected.

To validate that the alkali atoms were pumped by two photon absorption, an excitation spectrum using the blue stimulated emission as the signal was performed. The spectrum for a cesium cell at $200^oC$ is shown in Figure 39.
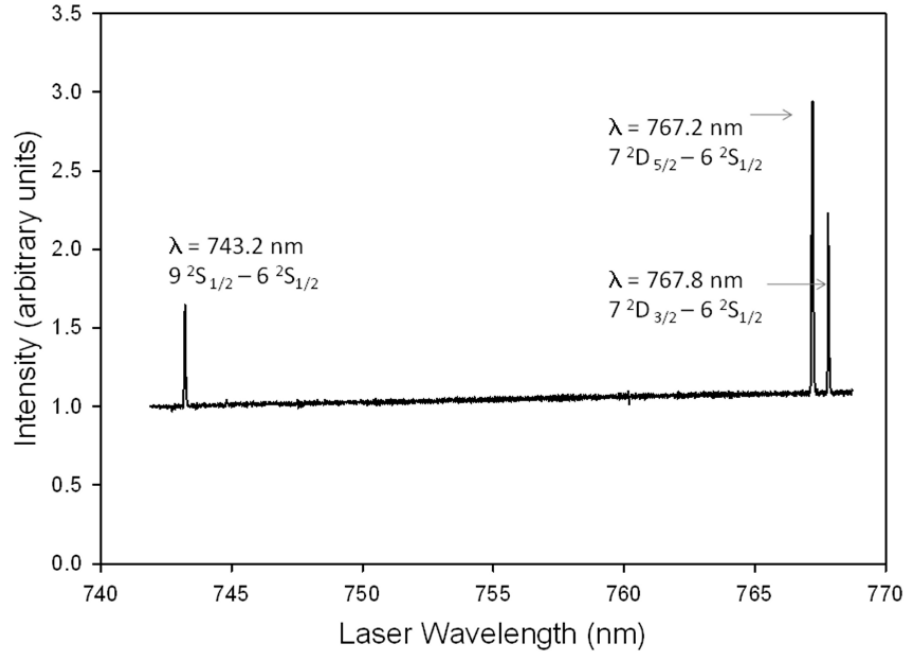
**Figure 39. Cs blue spot intensity as a function of pump laser wavelength.**

The blue spot in cesium occurred when the pump was tuned to 743.2 nm, 767.2 nm, and 767.8 nm, corresponding to the $6\,^2S_{1/2}$-$9\,^2S_{1/2}$, $6\,^2S_{1/2}$-$7\,^2D_{5/2}$, $6\,^2S_{1/2}$-$7\,^2D_{3/2}$ transitions, respectively. A small leakage of the pump beam intensity through the blue band pass filter produces the observed baseline intensity. Similarly, the blue spots for rubidium occurred at pump wavelengths of 778.1, 778.2, and 760.1 nm as illustrated in Figure 40. The Rb spectrum also illustrates increased absorption of the pump beam at the $D_2$ feature. No blue beam was observed when tuned to the $D_1$ or $D_2$ lines and the two photon lines are well outside of the wings of the $D_2$ absorption.
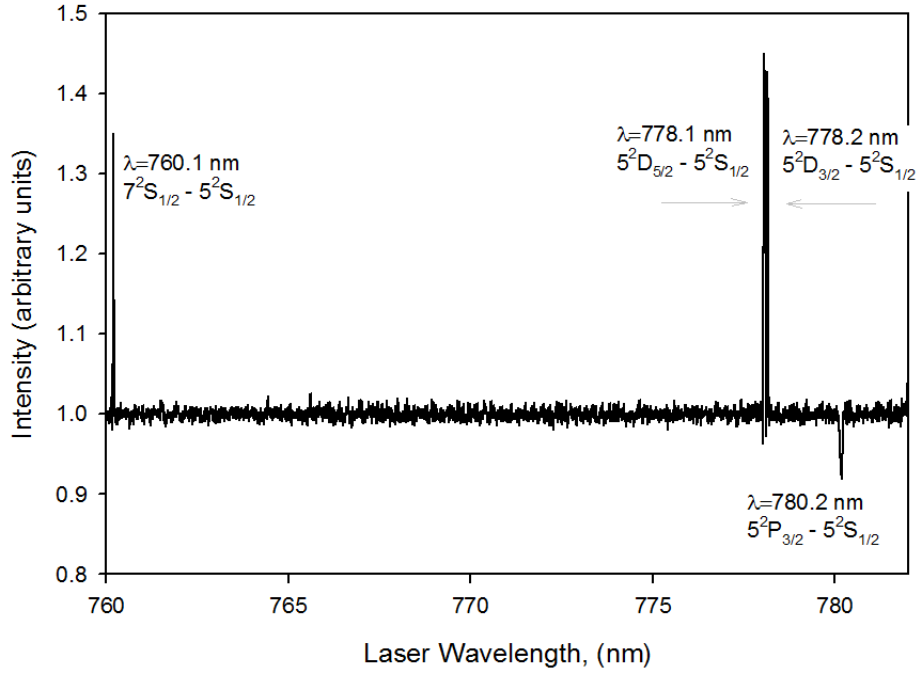
**Figure 40. Rb laser excitation spectrum for a cell at T= 217 °C.**

Attenuation of the pump laser at the $D_2$ resonance is reduced by two factors: (1) much of the pump bandwidth is outside of the absorption lineshape, and (2) the very intense pulsed laser bleaches the sample. At T = 200°C, the Rb concentration is ~ $10^{15}$ atoms/cm$^3$ and the optical density is very high, $\sigma_{D2}$[Rb] $l > 10^4$. However, the attenuation illustrated in Figure 40 is only ~10%. The pump spectral bandwidth of 16 GHz is about 25 times larger than the unsaturated, hyperfine split, Doppler broadened $D_2$ line. Additional broadening or absorption in the near wings may explain additional attenuation. In Figure 39, the pump energy per pulse is 3 mJ, providing a pump intensity of $\cong$ 2 x $10^6$ W/cm$^2$, much higher than the saturation intensity of Isat = (hv/ $\sigma_{D2}$) $A_{21}$ $\cong$ 5 W/cm$^2$. With a saturation parameter of S = $I/I_{sat}$ $\cong$ 5 x $10^5$, the sample is strongly bleached. At 10% absorption and 3 mJ/pulse incident, the number of absorbed photons is

73

1.2 x 10$^{15}$, nearly equal to the number of Rb atoms in the pumped volume.  A discussion

of absorption at the two photon wavelengths is provided below.

By spectrally resolving the stimulated emission for rubidium as in Figure 41,
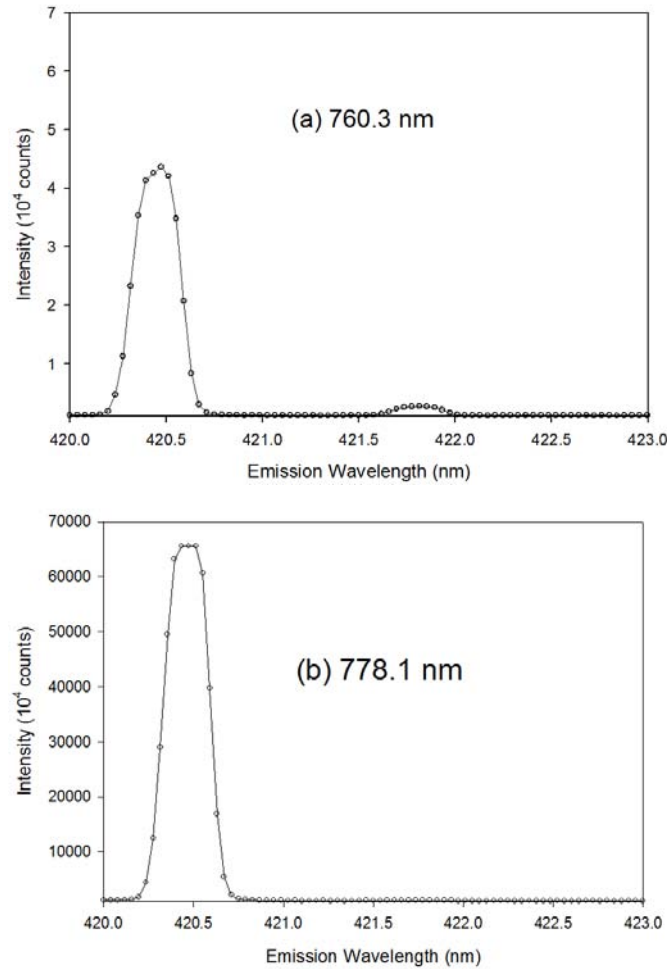


**Figure 41.  Spectrally resolved blue beam intensity from the Rb cell, when pumped on the: (a) 5 $^2$S$_{1/2}$ – 7 $^2$S$_{1/2}$ line at 760.3 nm, and the (b) 5 $^2$S$_{1/2}$ – 5 $^2$D$_{3/2}$ line at 778.1 nm.**

we note that the 6 $^2$P$_{3/2}$ – 5 $^2$S$_{1/2}$ is 16 times more intense than the 6 $^2$P$_{1/2}$ – 5 $^2$S$_{1/2}$

transition when pumping the 7 $^2$S$_{1/2}$ state. When pumping the 5 $^2$D$_{3/2}$ level, lasing was

limited to the $6\,^2P_{1/2} - 5\,^2S_{1/2}$ transition. When pumping the $5\,^2D_{5/2}$ level, lasing was of course limited to the $6\,^2P_{3/2} - 5\,^2S_{1/2}$ transition due to optical selection rules. Collisional relaxation between the spin-orbit split $6\,^2P_{3/2,\,1/2}$ states is minimal at these low pressures and lasing follows the strongest optical transitions between the pumped and upper laser level. Furthermore, collisional excitation of the upper laser level of the blue transition from the pumped level would be slow under the low pressure conditions. The mid IR stimulated emission appears necessary for the blue beam.

The temporal dynamics of the blue spot are illustrated in Figure 42.
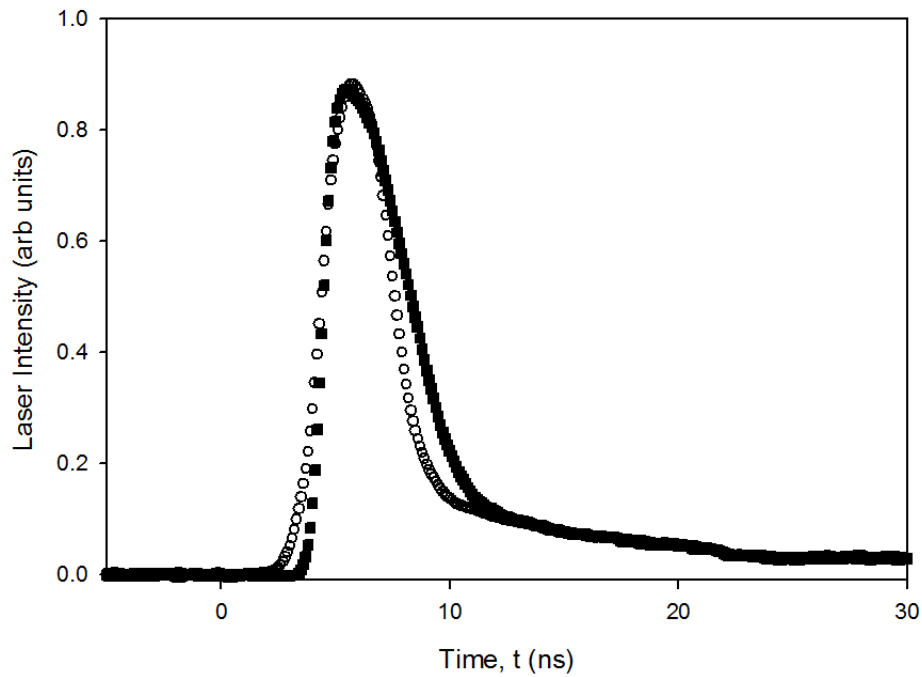


**Figure 42. Temporal profiles of the: (o) pump laser and (■) blue laser for Rb cell at T = 175°C pumped at 778.10 nm.**

The blue pulse is prompt, with minimal discernable delay of ~ 1 ns from the pump pulse indicating a very rapid cascade through the infrared transition. The duration of the blue

75

beam is about 4 ns, closely following the pump pulse temporal profile.  In contrast, the

blue side fluorescence shown in Figure 43 is long lived.
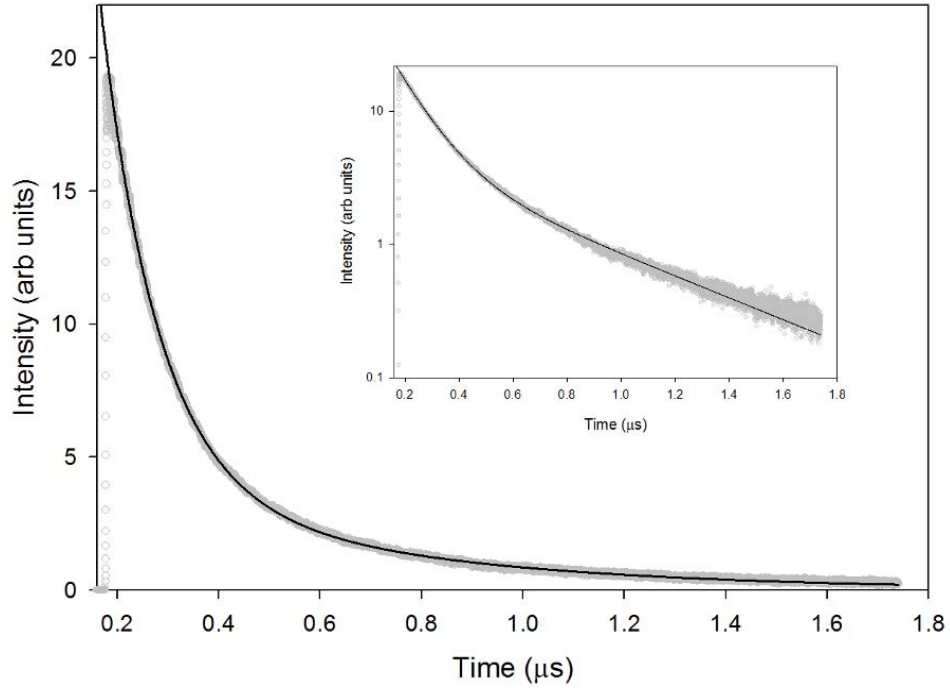


**Figure 43.  Temporal profile for the side fluorescence at 420 nm for the Rb cell at T = 175$^{\circ}$C pumped at 778.2 nm.**

The side fluorescence decay profile is prompt and double-exponential with an initial

decay of 0.11 µs, consistent with the radiative lifetime of 0.12 µs.[31]  A longer tail with

decay rate of 0.53 µs is also evident.  The alkali cells are optically thick and radiation

trapping along the un-pumped, radial direction is clearly evident.

**Threshold and Slope Efficiency in the Blue**

The energy in the blue beam pulse scales with pump energy and alkali

concentration (cell temperature) as illustrated in Figure 44and Figure 45.

76
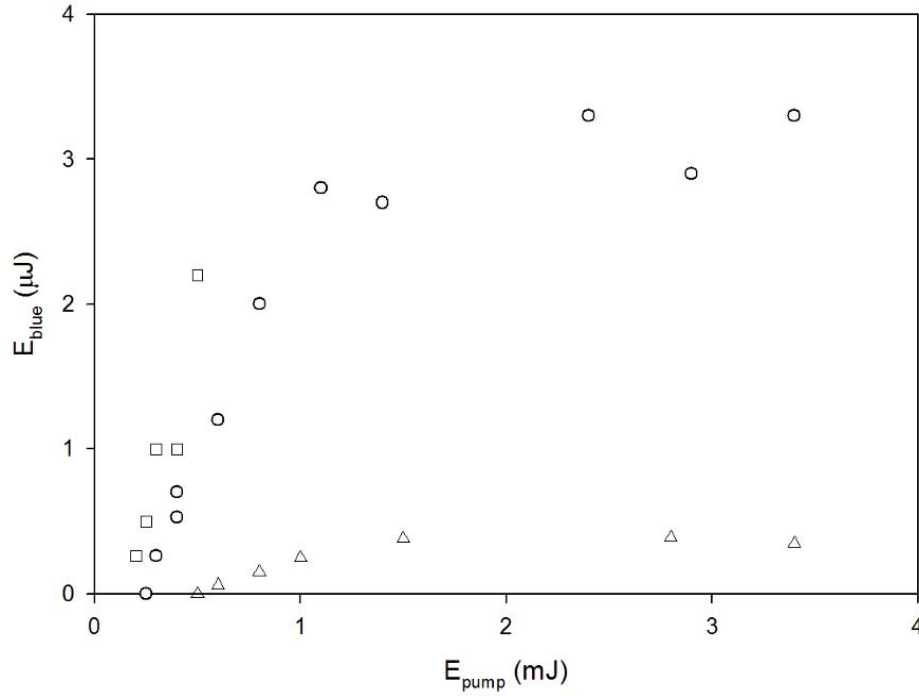
**Figure 44. Blue 6 $^2P_{3/2, 1/2}$ – 5 $^2S_{1/2}$ beam energy after pulsed laser pumping of the Rb 5 $^2S_{1/2}$ – 5 $^2D_{5/2}$ transition at cell temperatures of: (Δ) 175 $^o$C, (o) 200 $^o$C and (⊡) 250 $^o$C.**

The blue beam exhibits a pump threshold for the Rb 5 $^2S_{1/2}$ – 5 $^2D_{5/2}$ transition of ~ 0.3 mJ/pulse (2 x $10^5$ W/cm$^2$) and somewhat higher, ~1.5 mJ/pulse (1 x $10^6$ W/cm$^2$), for the Cs 6 $^2S_{1/2}$ – 7 $^2D_{3/2}$ transition. Surprisingly, the threshold for Rb decreases by a factor of 2.5 as the vapor pressure increases from 0.015 - 0.29 Torr. A similar decrease in threshold at high Cs concentration is also observed.
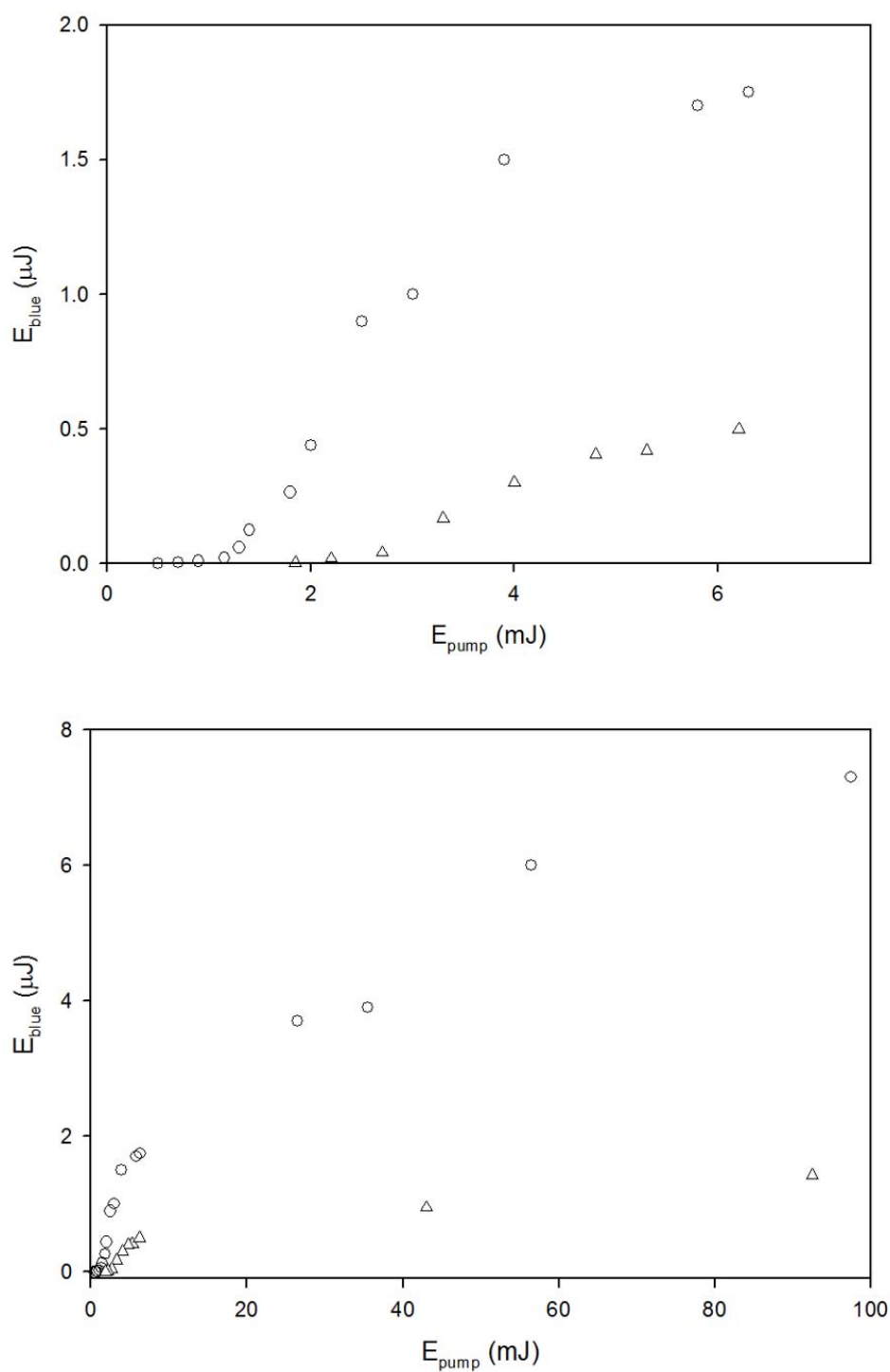
**Figure 45.** **Blue 6 $^2P_{3/2, 1/2}$ – 5 $^2S_{1/2}$ beam energy after pulsed laser pumping of the Cs 6 $^2S_{1/2}$ – 7 $^2D_{3/2}$ transition at cell temperatures of: (Δ) 175 $^oC$ and (o) 200 $^oC$.**

The blue transition slope efficiencies increase dramatically with alkali concentration, increasing from 0.03% to 0.5% for Rb as the cell temperature increases from T= 175 to 250 $^o$C. The peak Rb efficiency of 0.5% is about 5 times larger than reported for the previous two-wavelength pump schemes.[15]  The efficiency for Cs is somewhat less, 0.02 – 0.06 % for T = 175 and 200 $^o$C, despite the higher vapor pressure. Almost 10 μJ per pulse or 0.1 mW average power is achieved for the scaled Cs system.

Both threshold and pump efficiency should depend on the absorption cross-section. Typically two photon absorption cross-sections are quite low.  However, the cross-section for the Rb 5 $^2S_{1/2}$ – 5 $^2D_{5/2}$ has been calculated as 0.57 x $10^{-18}$ cm$^4$/W [13] and measured as 4 x $10^{-20}$ cm$^4$/W and 1.2 $\pm$ 0.5 x $10^{-18}$ cm$^4$/W [39,6].  At the threshold pump energy of 0.3 mJ, the corresponding intensity is ~ 200 kW/cm$^2$, yielding an effective absorption cross-section of 0.08 – 2.4 x $10^{-13}$ cm$^2$, depending on which of the prior two-photon cross-sections is employed.  At T = 200 $^o$C, the Rb concentration is 9.16 x $10^{14}$ atoms/cm$^3$ and the line center, unsaturated optical thickness of the two-photon absorption is high, $\sigma_{2photon}$[Rb] $l$ = 93 - 2792.

Again, the optical density is reduced by both the mismatch between the narrow absorption feature and the broad band pump, and the effects of saturation. Indeed, the 778.2 nm absorption in Rb at T = 200 $^o$C was observed to be about 3%.  Thus, the slope efficiencies based on the number of absorbed photons is higher.  At 3 mJ/pulse (2 x $10^6$ W/cm$^2$) and 200 $^o$C, the Rb blue output energy per pulse is 3 μJ.  For 3% of the incident photons absorbed, the blue energy corresponds to 3% of the absorbed pump energy.  The addition of a buffer gas to spectrally broaden the atomic absorption feature should lead to increased absorption and slope efficiency.  The output energy appears to be limited at

79

higher pump energies particularly when the alkali concentration is low. A full description of bleaching and saturation will require a better determination of the two photon absorption cross-section and lineshapes and a thorough understanding of the kinetic processes. Finally, recall that no optical cavity was used in the present experiment. The high optical loss is probably suboptimal output coupling and efficiency may be increased with an appropriate resonator design.

A comparison of the blue alkali performance relative to the standard DPAL system is illustrative. The standard red DPAL typically exhibits a threshold at 4 $kW/cm^2$,[40,41,5] about 50 times less than the present results. The two-photon absorption cross-section is between 2 and 60 times lower than the value for single photon absorption on the $D_2$ line with broadening associated with 600 Torr of helium. Thus, the relative thresholds appear consistent with the rather uncertain ratio of absorption cross-sections.

**Infrared Lasers**

All of the current experiments were performed at low pressure with no added buffer gas and the transfer of population from the initially pumped $5\ ^2D_{3/2}$, $5\ ^2D_{5/2}$, and $7\ ^2S_{1/2}$ states of rubidium and the $7\ ^2D_{3/2}$, $7\ ^2D_{5/2}$, and $9\ ^2S_{1/2}$ states of cesium to the upper blue laser level n=6 or $7\ ^2P_{3/2,1/2}$ states occurs optically. Given the minimal delay between the pump pulse and the appearance of the blue beam as illustrated in Figure 42, it appears that stimulated emission on the infrared transitions is required. Indeed, the pumped levels would immediately be inverted relative to the upper $^2P_{1/2,\ 3/2}$ levels. In cesium the energies associated with these transitions range between 1.94 $\mu$m and 2.43$\mu$m

and in rubidium 3.85 – 5.2 µm.  Using an InSb detector with two 1.5 µm long pass filters

and a 2.5 µm short pass filter, the 2.34 µm and 2.43 µm spots from the $7\,^2D_{3/2} - 6\,^2P_{1/2}$

and $7\,^2D_{5/2} - 6\,^2P_{3/2}$ transitions were observed.

The intensity of the Cs infrared spot increased linearly with pump energy, with a

very small threshold, as shown in Figure 46.
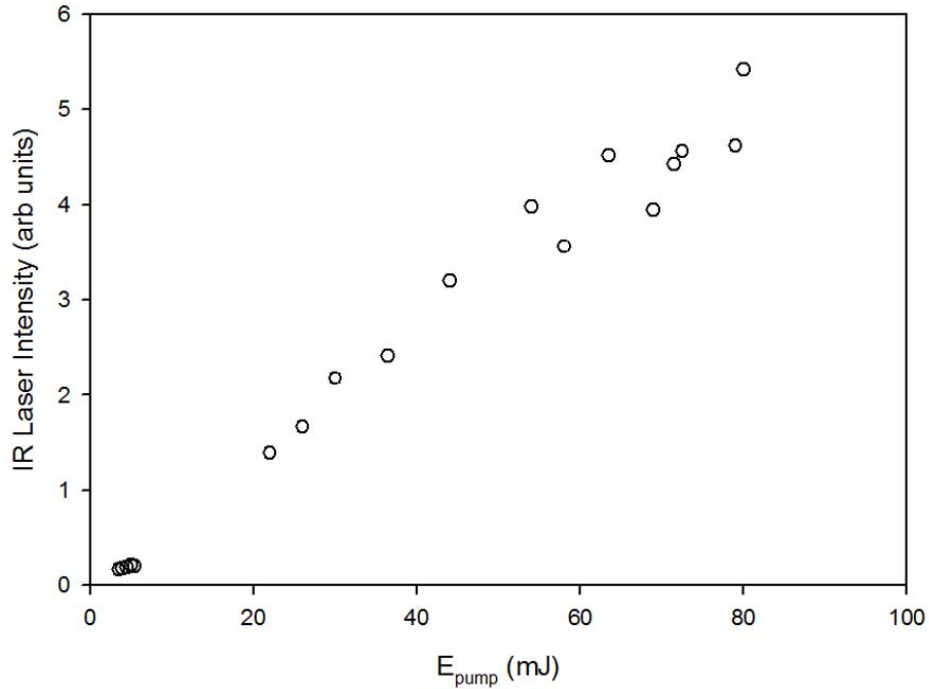


**Figure 46.  Infrared beam energy after pulsed laser pumping of the Cs $6\,^2S_{1/2} - 7$
$^2D_{3/2}$ transition at a cell temperature of (o) 185 $^o$C.**

Since no population initially exists in the n=6 or $7\,^2P_{3/2,1/2}$ states, the inversion would be

prompt.  The radiative lifetime of the Cs $7\,^2D_{5/2}$ state is about 88 ns[6] yielding a Doppler

broadened stimulated emission cross-section of $\sigma_{IR} \cong 3 \times 10^{-10}$ cm$^2$. With a 100% loss per

single pass, threshold is achieved at $[Cs(7\,^2D_{5/2}] \cong 10^9$ atoms/cm$^3$.  Assuming every

absorbed photon leads to an inverted atom and 10% absorption, suggests an IR threshold pump energy of ~ 3 nJ/pulse (2 W/cm$^2$).

In contrast with the energy in the blue beam, the IR energy exhibits linear scaling with pump energy to 100 mJ.  At these highest pump energies, there are more photons incident than atoms in the pumped volume.  Given that the sample must be bleached at the lower threshold for the blue beams, it appears necessary that the atoms undergo a number of pump/IR/blue cycles over the short duration of the pump pulse.  The transit time for a photon along the beam axis in the gain medium is about 0.2 ns and more than 10 cycles might be possible.  However, the rate limiting step in the cycle would seem to be the blue transition that exhibits decreased efficiency at higher pump energies.  A full interpretation of the IR and blue slope efficiencies await a thorough kinetic model of this system.

Several mid-IR laser wavelengths appear achievable under two photon pumping. In rubidium the 5 $^2$D$_{5/2}$ → 6 $^2$P$_{3/2}$ and 5 $^2$D$_{3/2}$ → 6 $^2$P$_{1/2}$ transitions at 5.03 and 5.23 μm and the 7 $^2$S$_{1/2}$ → 6 $^2$P$_{3/2,1/2}$ transitions at 3.85 and 3.97 μm are evident in the present work. Likewise, Cs operates at 2.34 and 2.43 μm for the 7 $^2$D$_{5/2}$ → 7 $^2$P$_{3/2}$ and 7 $^2$D$_{3/2}$ → 7 $^2$P$_{1/2}$ transitions and at 1.94 and 2.01 μm for the 9 $^2$S$_{1/2}$ → 7 $^2$P$_{3/2,1/2}$ transitions.  Additional wavelengths of 1.87 – 12.14 μm may also be available by pumping the 6D and 8S states of Rb and the 8S and 6D states of Cs.

**Conclusions**

Stimulated emission on the blue $^2$P – $^2$S transitions in Rb and Cs has been achieved by pumping at a single wavelength in the red via two photon absorption.  The

slope efficiency of 0.5% in Rb is considerably higher than achieved in the prior sequential double resonance experiments[15] and requires only a single wavelength pump source. Incomplete (10%) absorption of the pump photons is an important contributor to the decreased efficiency and might be improved with narrow band pumping or pressure broadening. Cascade lasing on the infrared transition followed by the blue transition offers no quantum defect and the potential for low heat loads. There would also be no need for a spin orbit coupling gas, such as ethane, which has caused soot buildup problems in traditional DPALs cells at high temperature.[16] It appears that the performance of this system can be enhanced by scaling to higher alkali concentrations, possible in a heat pipe configuration. Threshold pump intensities are high, but the ultimate performance limits of this system have not been assessed. Indeed, a full analysis of the kinetic mechanism is required to evaluate both the scaling and efficiency of this new system. Potential applications for this new laser system include underwater communications and infrared countermeasures such as blinding heat seeking missiles.

**Acknowledgements**

# VI. Conclusions and Recommendations

Prior to this research, very little characterization of a DPALs device had been accomplished. Most researchers were focused on achieving the highest possible slope efficiencies with a maximum amount of output power by selecting the optimum output coupling and temperatures for their cavity design. Only one article considered laser performance with different output couplers and buffer gases, and then only varied the temperature to achieve the maximum output power. Given the high levels of interest in the feasibility of scaling a DPAL to a tactical level kilowatt class device, a thorough understanding of the laser performance under a wide range of conditions is required and is provided through this research.

In addition to a thorough characterization of DPALs, a robust model accurately representing the laser system is required. AFIT, through Dr. Gordon Hager, has developed multiple DPAL models which incorporated all of the physics believed to be relevant in a DPALs three-level system. However, the validation of these models, prior to this work, was accomplished through a comparison of laser output powers for a single set of laser parameters, which allows for the possibility of masking artifacts within the models.

Furthermore, while studying the kinetics of alkali gases, a blue beam was produced in a low pressure alkali vapor under extremely high pump intensities. Although attempts had been made previously to produce blue alkali lasers through sequential pumping in the red, and previous researchers had studied the two photon absorption

process in the alkalis, it is believed that no attempt had been made to produce a blue alkali laser through a two photon absorption.

**DPAL at High Pump Intensity**

During the course of this research, rubidium laser performance data was collected under a wide variety of conditions, varying the output coupler reflectivity, the cell temperature which drove the alkali number density, and the types and amounts of buffer gases in the cell providing spin orbit relaxation and pressure broadening. The explored parameter space as well as the laser data is provided in Appendix A. Analysis of this data in conjunction with the frequency dependent three-level model demonstrated that laser performance degradation at high pump intensities due to thermal effects is a result of a density gradient in both alkali and spin orbit gas concentrations from on axis heating. This is contrary to the previously proposed thermal effects, which suggest the on axis heating results in a thermal lens, degrading laser performance.[40,48] This important distinction in thermal effects, implies that laser performance can easily be recovered by simply increasing the concentration of alkali and buffer gas in the gain volume, while a thermal lensing scenario would require a flowing gas system for cooling to prevent the temperature from becoming elevated and maintaining laser performance, drastically increasing the complexity of an operational system.

In addition to the on axis heating analysis, this work produced a rubidium laser which maintained a linear slope efficiency through pump intensities as high as 32 times the threshold value. The ability to maintain linear performance this far beyond threshold, essentially negates the initial losses that must be overcome to bleach through the alkali

cell and begin the lasing process. Pumping a rubidium laser at 32 times beyond its threshold value results in an overall efficiency of 95% when the quantum efficiency is incorporated, providing further evidence that DPALs should be scalable to highly efficient kilowatt class devices for the Air Force.

**Quasi Two Level Model**

It has routinely been assumed that when using ethane or methane as the spin orbit relaxing gas in a DPAL, the spin orbit rate between the $^2P_{3/2}$ and $^2P_{1/2}$ state is sufficiently fast that the laser operates in the quasi two level limit, where one assumes that the population immediately transfers between the spin orbit split states. This assumption is valid if the spin orbit rate is faster than the pump rate, and holds under typical DPAL conditions. This research has validated the quasi two level analytic model through an analysis of the slope efficiency dependence on output coupler and alkali concentration. Expressing the slope efficiency of a DPAL system as absorbance, creates a value that scales linearly with alkali concentration in the gain volume which can be represented by the quasi-two level analytic model developed by AFIT. Although the model accurately represented the absorbance of the system, the effective cross section required to fit the data with the analytic equations was seven times lower than anticipated. Several efforts are proposed in the future work section to resolve this discrepancy.

**Temporal Dynamics**

During the course of this research, the temporal dynamics of a pulsed alkali laser system have been studied for the first time. Although the pulsed rubidium laser was operating in a quasi steady state regime, the efficiency of the system did change during

the lifecycle of the pulse. This verified for the DPAL community that caution must be used when averaging a pulse to determine efficiency of a system, and in fact it is better to use the instantaneous efficiencies of the system through the pulse lifecycle. The instantaneous efficiency analysis provided confirmation that laser performance degradations were attributable to limitation in the spin orbit coupling rate, easily recovered though an increase in the spin orbit gas concentration. In fact, all laser performance reductions observed were attributed to limitations due to concentrations of buffer gas or alkali and can be reversed, implying no evidence of second order kinetics which would catastrophically limit DPAL performance.

The three-level frequency dependent pulsed DPAL model accurately represented the temporal pulse shape data when only ethane or methane were present as buffer gases. However, the model, using the same fit parameters could not predict the increase in laser performance with the addition of helium into the laser cavity, but indicated an on axis temperature increase of $226^{o}C$ was sufficient to explain the performance increase.

**Blue and Infrared Spots**

This work has demonstrated the production of blue and infrared amplified spontaneous emission beams through a two photon absorption process in both rubidium and cesium. The slope efficiency, 0.5% in rubidium, while low compared to a traditional DPAL, is higher than experiments employing a sequential double resonance absorption. Since all transitions in this three-level system are optical, there is not quantum defect in the system implying the potential for very low heat loading. Additionally, the spin orbit gas required in a DPAL that can lead to soot deposition on the windows is no a factor in

87

this system.  The performance limit attainable through increasing the alkali concentration in a heat pipe configuration has yet to be achieved.

**Proposed Future Work**

To resolve the effective cross section discrepancies in the quasi two level model, measurements of the alkali concentration within the pumped volume as well as the temporal dependence of the bleached wave should be studied.  In addition, the three-level frequency dependent model should be modified to incorporate the effects of on axis heating, as well as the addition of a spatially varying Gaussian pump pulse capable of bleaching the system at different pump intensities.

There is a great deal of future work that should be performed on the two photon absorption blue and IR ASE beams.  A full analysis of the kinetic mechanism is required to evaluate the scaling and the efficiency of this new system.  In addition, the two photon absorption cross sections must be accurately measured, as well as the production mechanism dependence when a pressure broadening gas is added to the system. Following the kinetic study, an attempt should be made to produce a true laser in both the blue and IR simultaneously.

## Appendix A.  Raw Data

During the course of this research effort, a large amount of laser performance data was collected while attempting to characterize DPAL performance and develop an understanding of how alkali number density, output coupler reflectivity and buffer gas types affected output laser performance.  Unfortunately, the data presented in journal articles must be condensed to the minimum absolutely necessary.  Therefore, most of the measured data was not included in the journal submissions nor the previous chapters.  This appendix is an attempt to archive all of the data which was collected should follow on researchers chose to reexamine the parameter space which has been presented here.  First, a table demonstrating the wide range of varied parameters is shown, and is followed by figures documenting the laser power vs. the input pump power for all cases.

**Table 11. Rubidium DPAL data sets collected during the course of this research.**

| Cell Temp (°C) | Output Coupler Reflectivity | SO Gas | Pump Power Range |
|---|---|---|---|
| 106 | 23% | 550 Torr $CH_4$ | 0.1 - 1.8 W |
| 109 | 23% | 550 Torr $CH_4$ | 0.1 - 1.8 W |
| 111 | 23% | 550 Torr $CH_4$ | 0.1 - 1.8 W |
| 109 | 32% | 550 Torr $CH_4$ | 0.1 - 1.8 W |
| 114 | 32% | 550 Torr $CH_4$ | 0.1 - 1.8 W |
| 117 | 32% | 550 Torr $CH_4$ | 0.1 - 1.8 W |
| 120 | 32% | 550 Torr $CH_4$ | 0.1 - 1.8 W |
| 120 | 50% | 450 Torr $C_2H_6$ | 0.1 - 2 W |
| 110 | 50% | 450 Torr $C_2H_6$ | 0.1 - 2 W |
| 100 | 50% | 450 Torr $C_2H_6$ | 0.1 - 2 W |
| 90 | 50% | 450 Torr $C_2H_6$ | 0.1 - 2 W |
| 80 | 50% | 450 Torr $C_2H_6$ | 0.1 - 2 W |
| 120 | 20% | 450 Torr $C_2H_6$ | 0.1 - 2 W |
| 110 | 20% | 450 Torr $C_2H_6$ | 0.1 - 2 W |
| 100 | 20% | 450 Torr $C_2H_6$ | 0.1 - 2 W |
| 90 | 20% | 450 Torr $C_2H_6$ | 0.1 - 2 W |
| 80 | 20% | 450 Torr $C_2H_6$ | 0.1 - 2 W |
| 120 | 70% | 450 Torr $C_2H_6$ | 0.1 - 2 W |
| 100 | 70% | 450 Torr $C_2H_6$ | 0.1 - 2 W |
| 80 | 70% | 450 Torr $C_2H_6$ | 0.1 - 2 W |
| 90 | 20% | 600 Torr $C_2H_6$ | 0.1 - 3 W |
| 100 | 20% | 600 Torr $C_2H_6$ | 0.1 - 3 W |
| 110 | 20% | 600 Torr $C_2H_6$ | 0.1 - 3 W |
| 120 | 20% | 600 Torr $C_2H_6$ | 0.1 - 3.5 W |
| 90 | 20% | 300 Torr $C_2H_6$ / 200 Torr $He_4$ | 0.1 - 3 W |
| 100 | 20% | 300 Torr $C_2H_6$ / 200 Torr $He_4$ | 0.1 - 3 W |
| 120 | 20% | 300 Torr $C_2H_6$ / 200 Torr $He_4$ | 0.1 - 3 W |
| 90 | 20% | 450 Torr $C_2H_6$ / 200 Torr $He_4$ | 0.1 - 3 W |
| 100 | 20% | 450 Torr $C_2H_6$ / 200 Torr $He_4$ | 0.1 - 3 W |
| 120 | 20% | 450 Torr $C_2H_6$ / 200 Torr $He_4$ | 0.1 - 3 W |
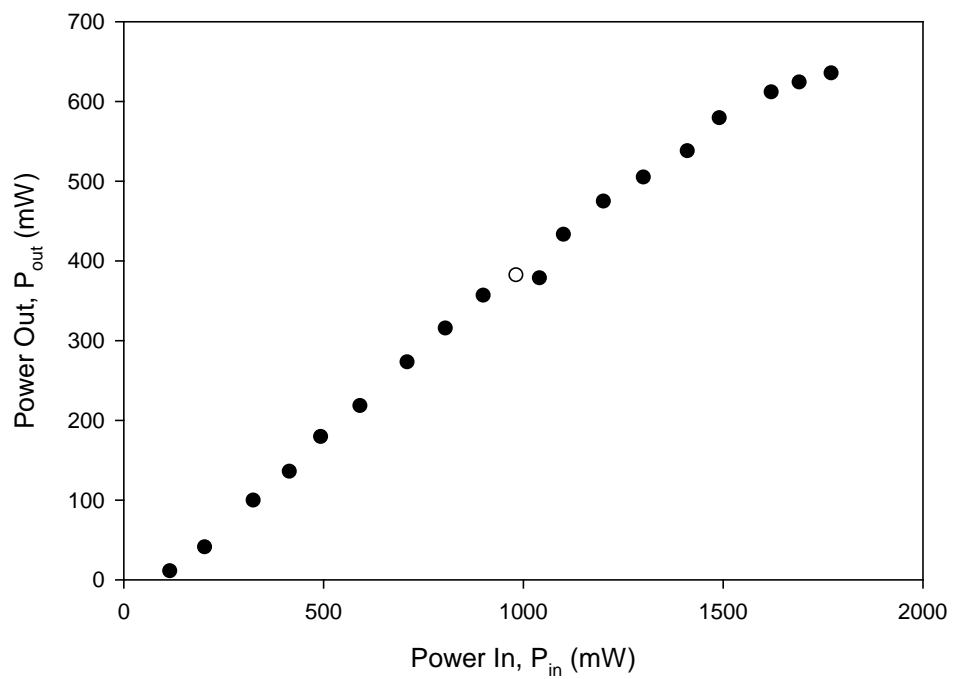
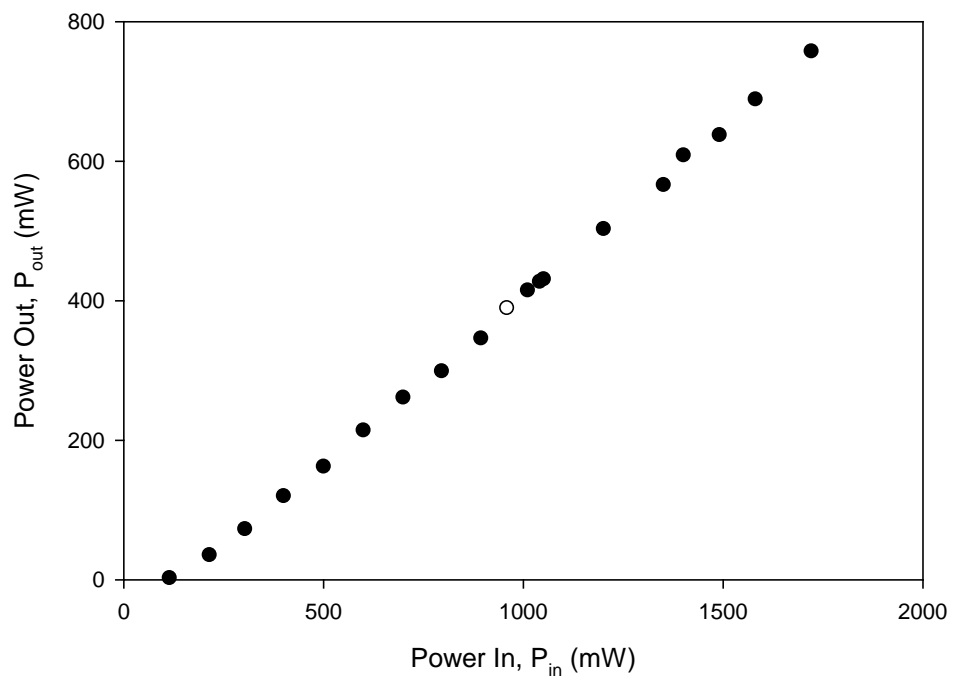**Figure 47.** $P_{methane} = 550$ **Torr,** $R_{OC} = 23\%$, $T = 106^{\text{o}}$**C**
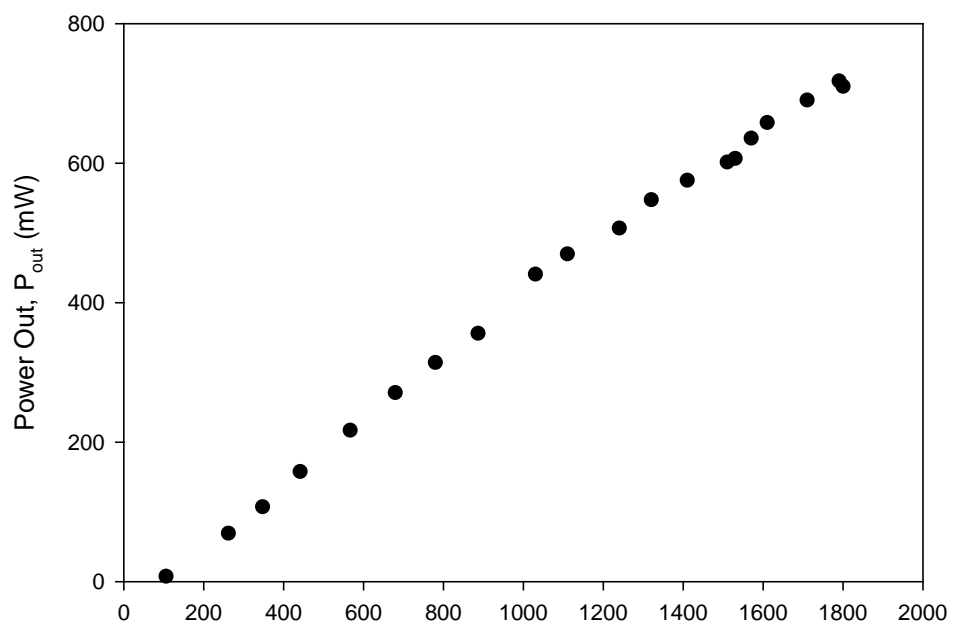


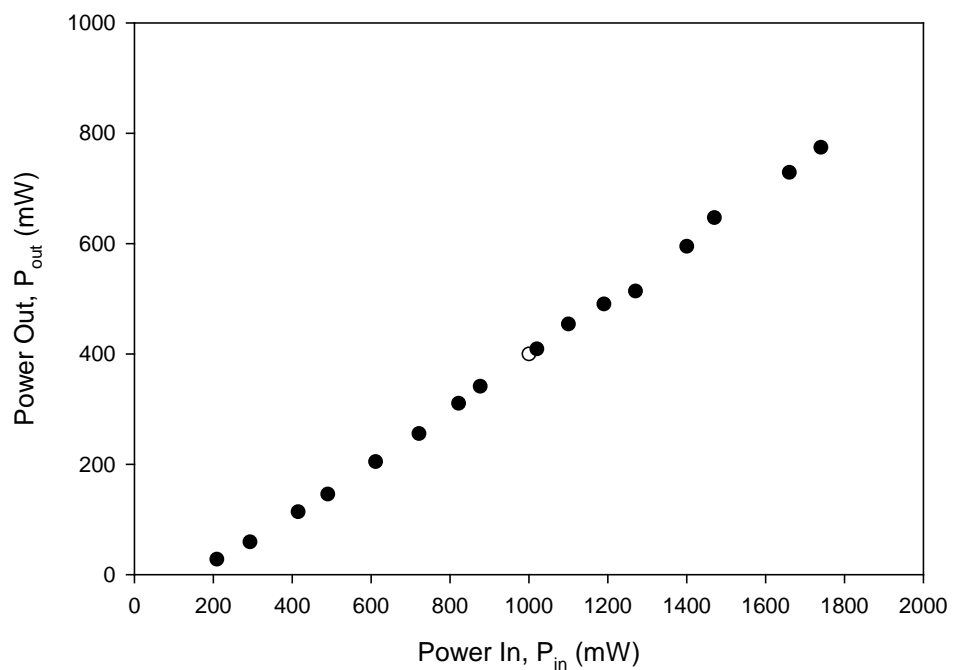**Figure 48.** $P_{methane} = 550$ **Torr,** $R_{OC} = 23\%$, $T = 109^{\text{o}}$**C**
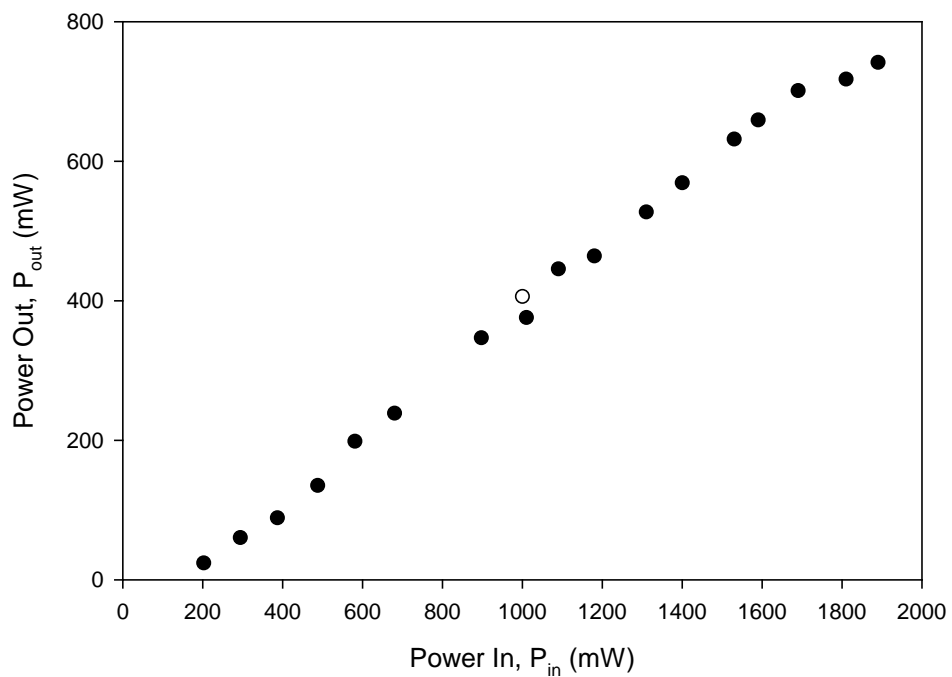
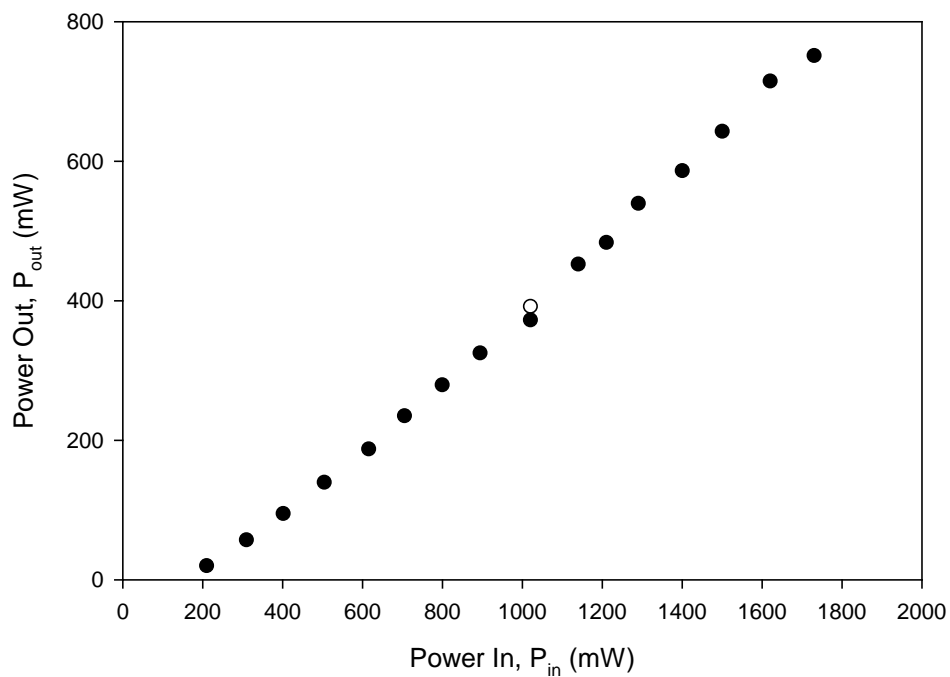**Figure 49.** $P_{methane} = 550$ **Torr,** $R_{OC} = 23\%$, $T = 111^{\circ}$**C**
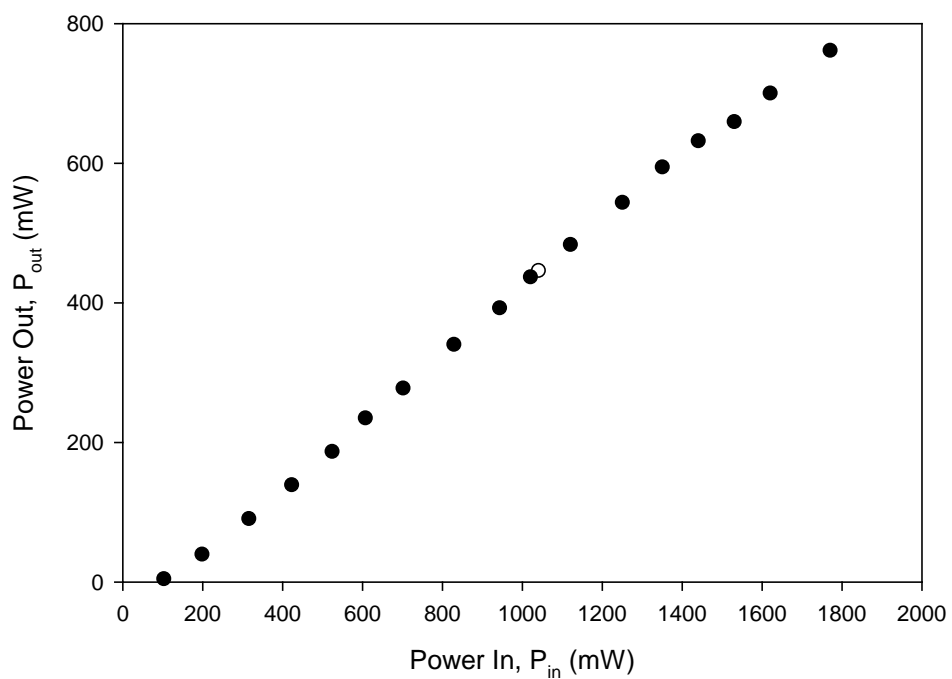


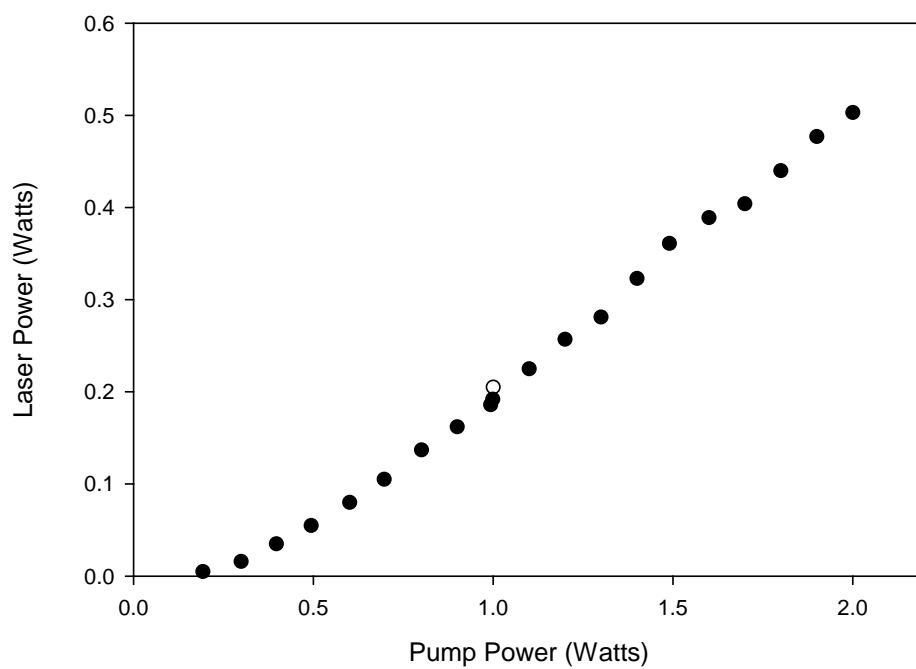**Figure 50.** $P_{methane} = 550$ **Torr,** $R_{OC} = 32\%$, $T = 109^{\circ}$**C**

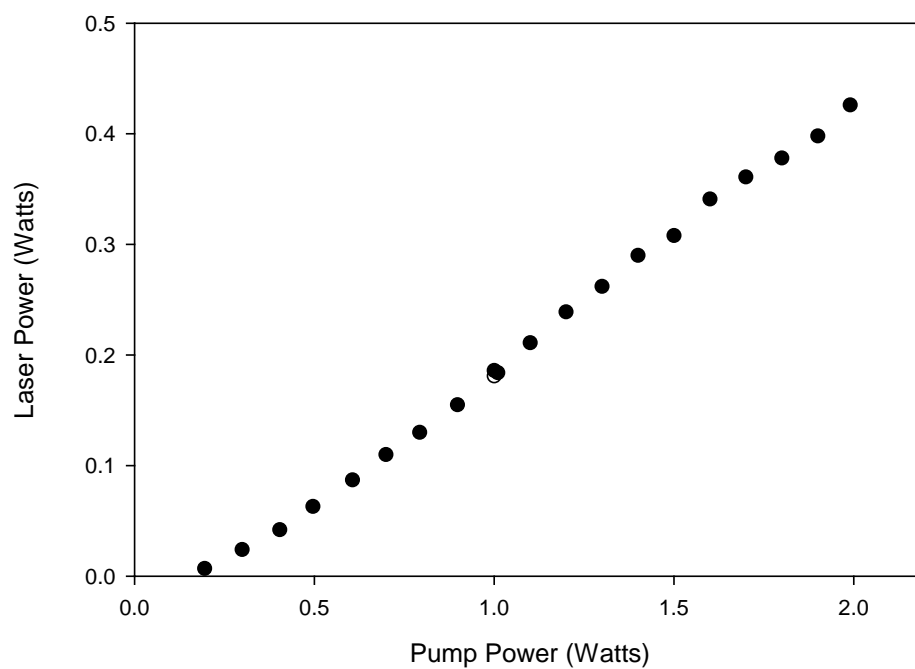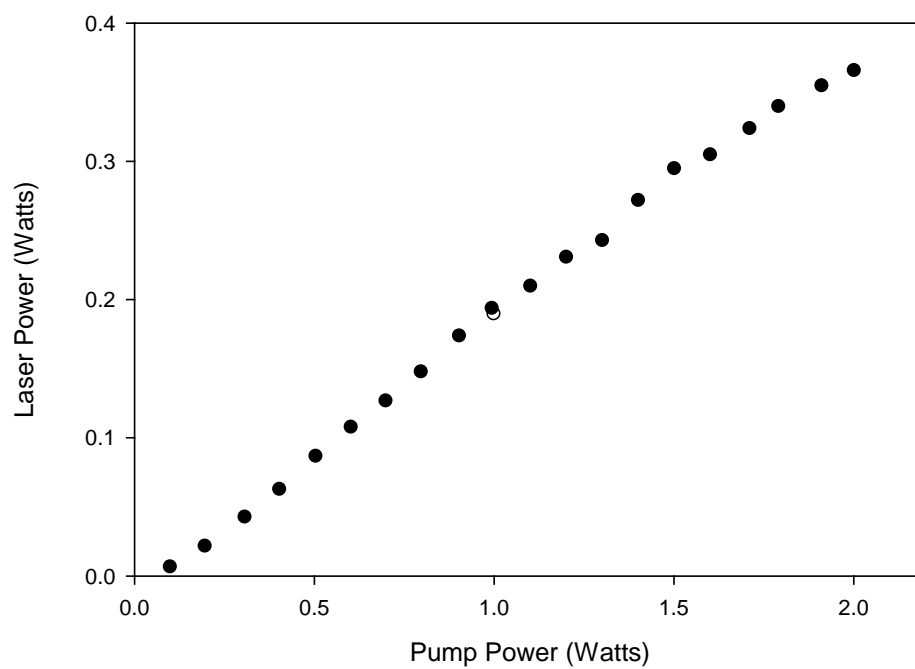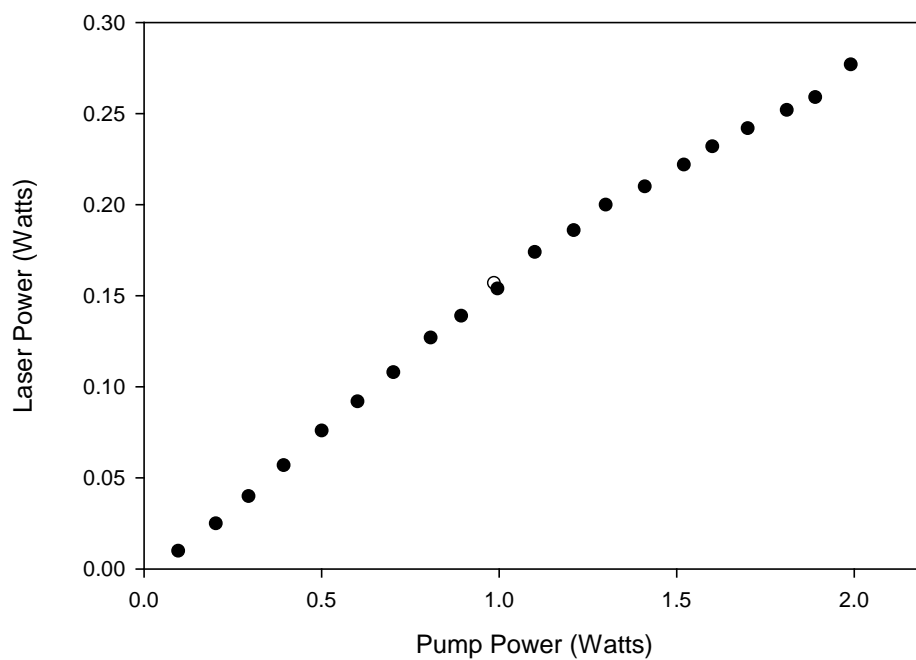**Figure 51.** $P_{methane} = 550$ **Torr,** $R_{OC} = 32\%$, $T = 114^{\circ}$**C**



**Figure 52.** $P_{methane} = 550$ **Torr,** $R_{OC} = 32\%$, $T = 117^{\circ}$**C**

**Figure 53.** $P_{methane}$ = 550 Torr, $R_{OC}$ = 32%, $T$ = 120°C



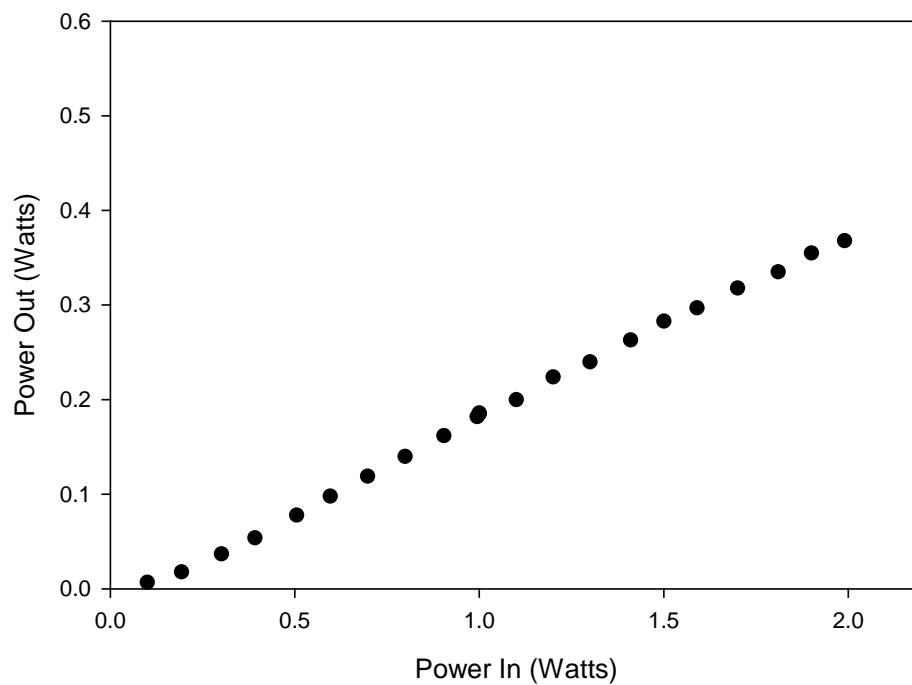**Figure 54.** $P_{ethane}$ = 450 Torr, $R_{OC}$ = 50%, $T$ = 120°C

**Figure 55.** $P_{ethane} = 450$ **Torr,** $R_{OC} = 50\%$, $T = 110^{\circ}$**C**



**Figure 56.** $P_{ethane} = 450$ **Torr,** $R_{OC} = 50\%$, $T = 100^{\circ}$**C**

**Figure 57.** $P_{ethane}$ = 450 Torr, $R_{OC}$ = 50%, $T$ = 90°C
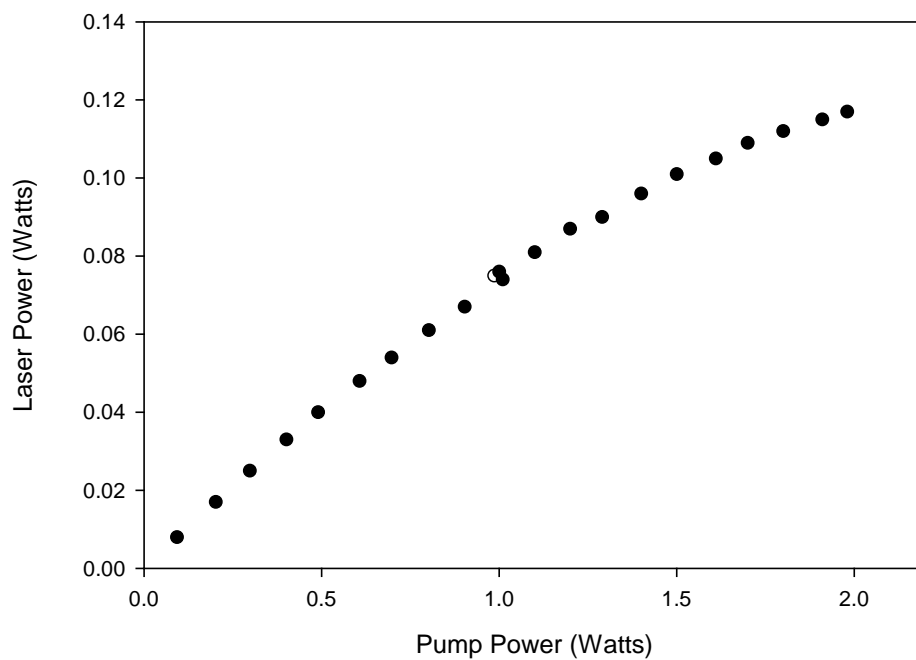


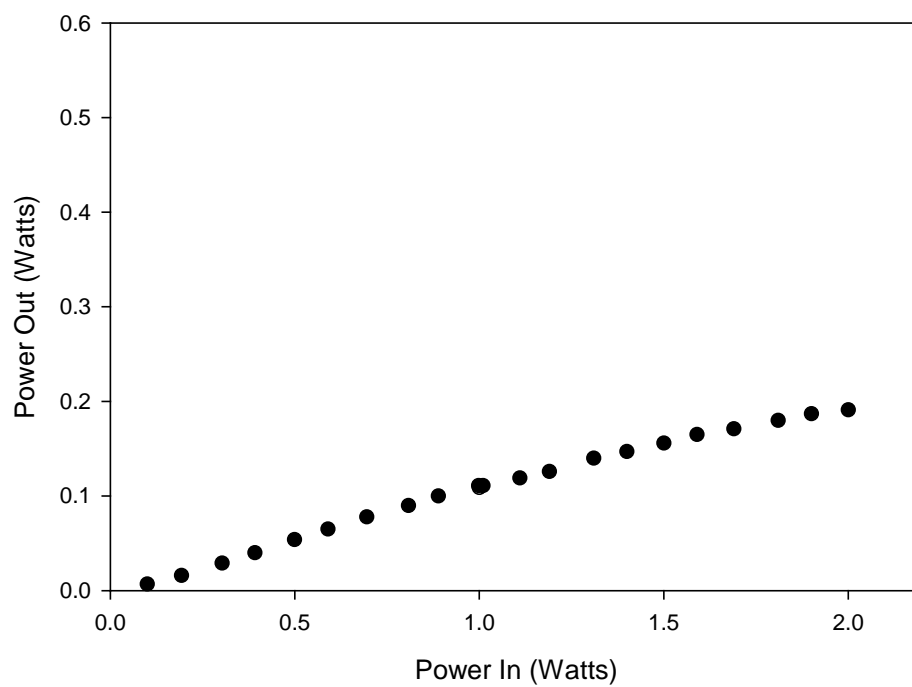**Figure 58.** $P_{ethane}$ = 450 Torr, $R_{OC}$ = 50%, $T$ = 80°C
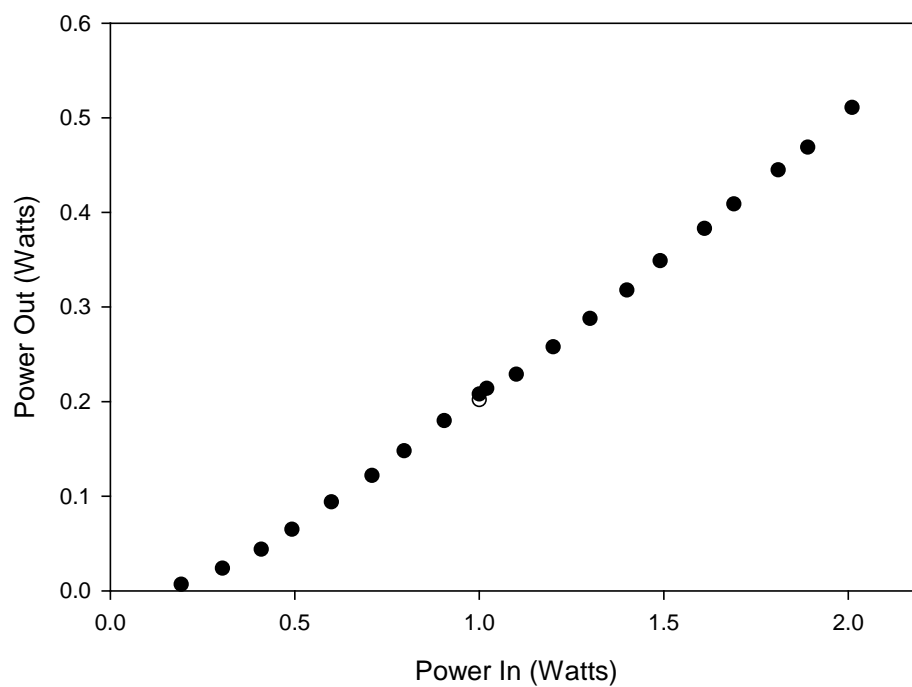
**Figure 59.** $P_{ethane} = 450$ Torr, $R_{OC} = 20\%$, $T = 120^{\circ}$C
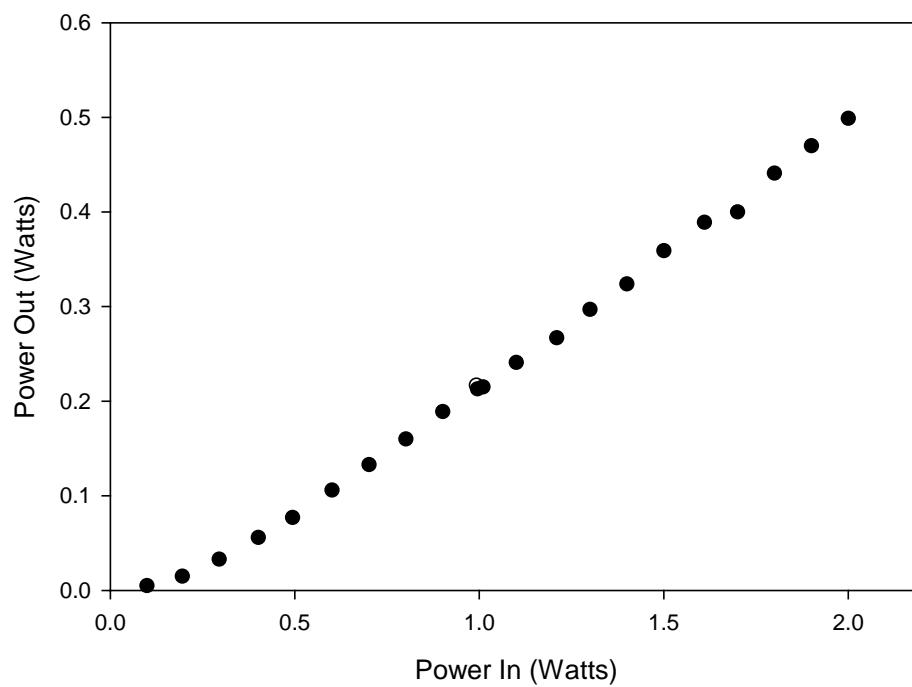


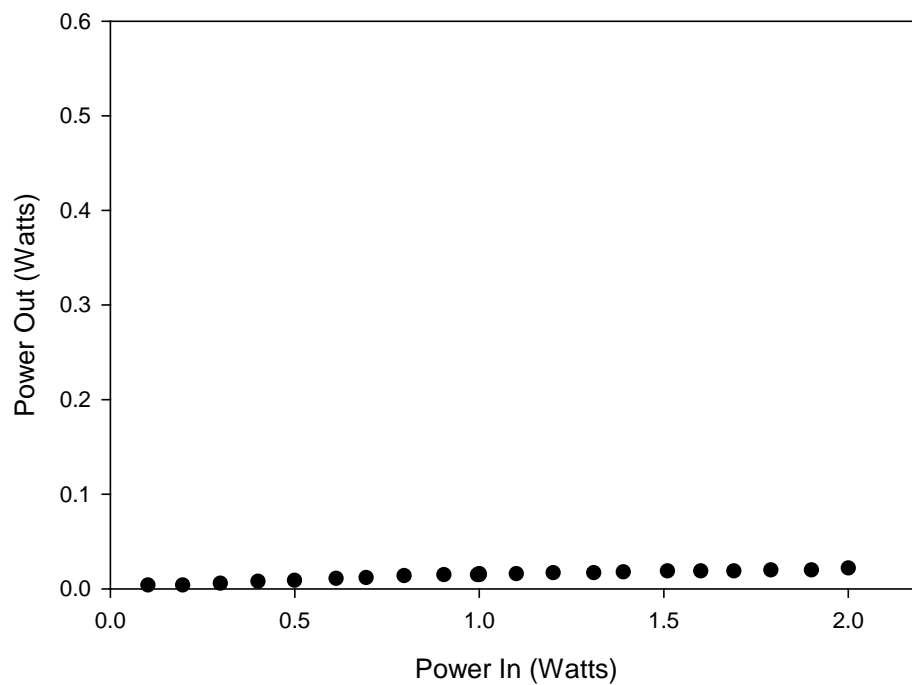**Figure 60.** $P_{ethane} = 450$ Torr, $R_{OC} = 20\%$, $T = 110^{\circ}$C

**Figure 61.** $P_{ethane} = 450$ Torr, $R_{OC} = 20\%$, $T = 100^{o}$C
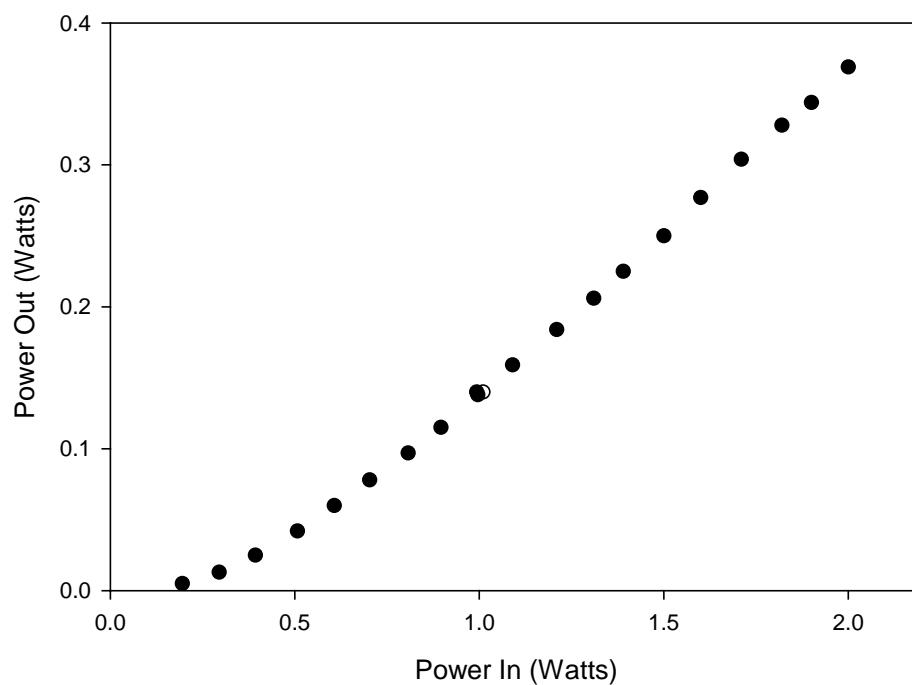


**Figure 62.** $P_{ethane} = 450$ Torr, $R_{OC} = 20\%$, $T = 90^{o}$C

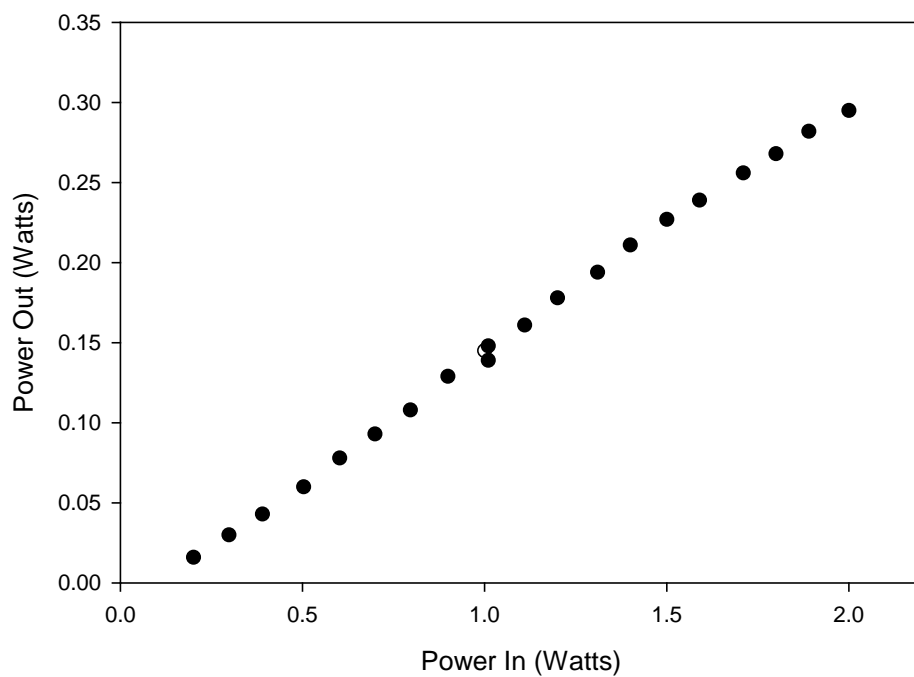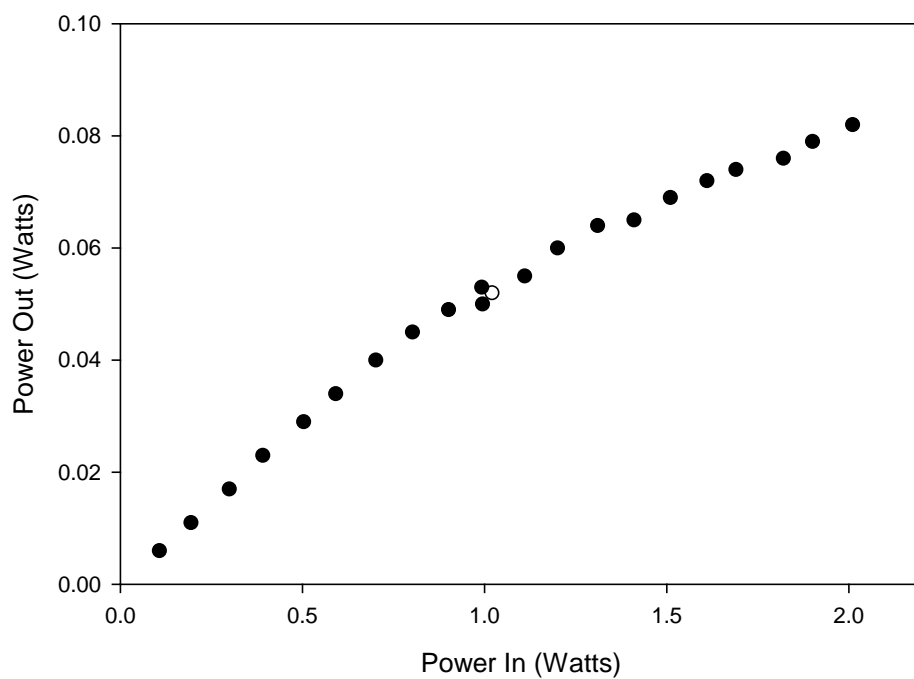**Figure 63.** $P_{ethane}$ = 450 Torr, $R_{OC}$ = 20%, $T$ = 80$^o$C
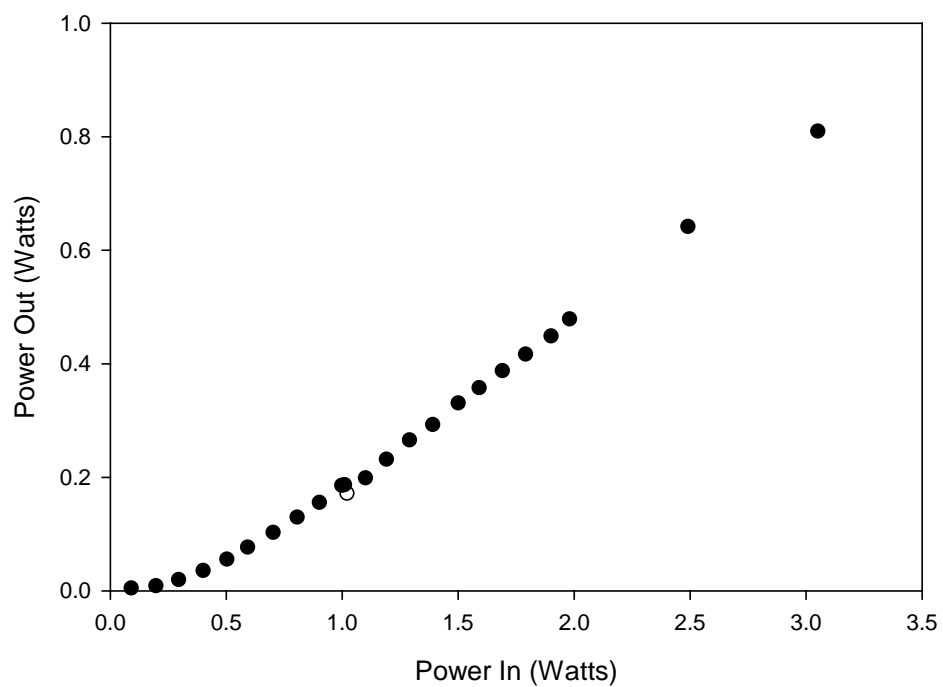


**Figure 64.** $P_{ethane}$ = 450 Torr, $R_{OC}$ = 70%, $T$ = 120$^o$C

**Figure 65.** $P_{ethane} = 450$ **Torr,** $R_{OC} = 70\%$**,** $T = 100^oC$



**Figure 66.** $P_{ethane} = 450$ **Torr,** $R_{OC} = 70\%$**,** $T = 80^oC$

**Figure 67.** $P_{ethane}$ = 600 Torr, $R_{OC}$ = 20%, $T$ = 120$^o$C
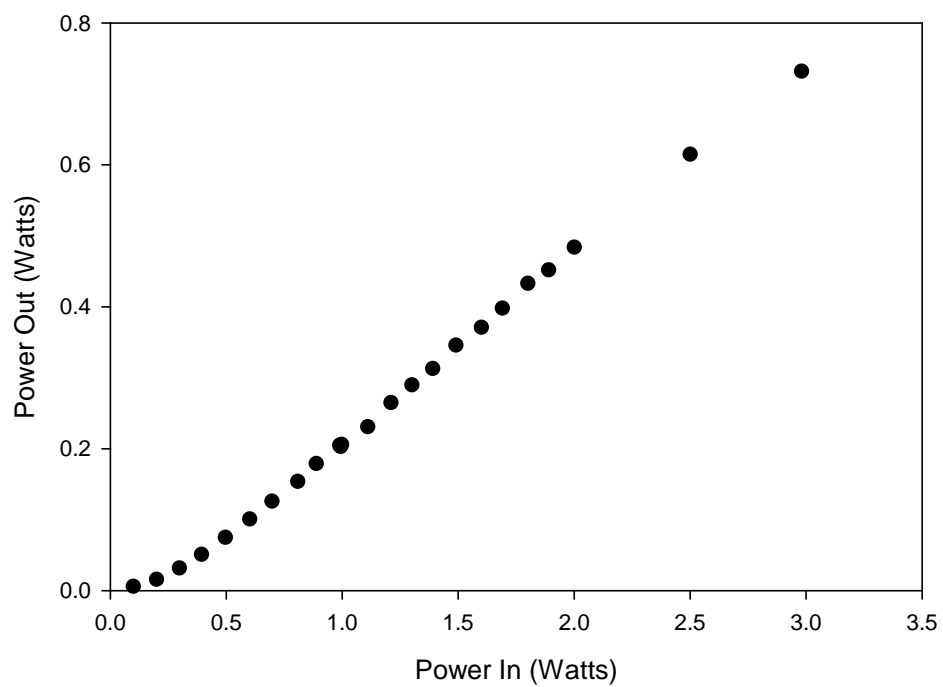


**Figure 68.** $P_{ethane}$ = 600 Torr, $R_{OC}$ = 20%, $T$ = 110$^o$C

101
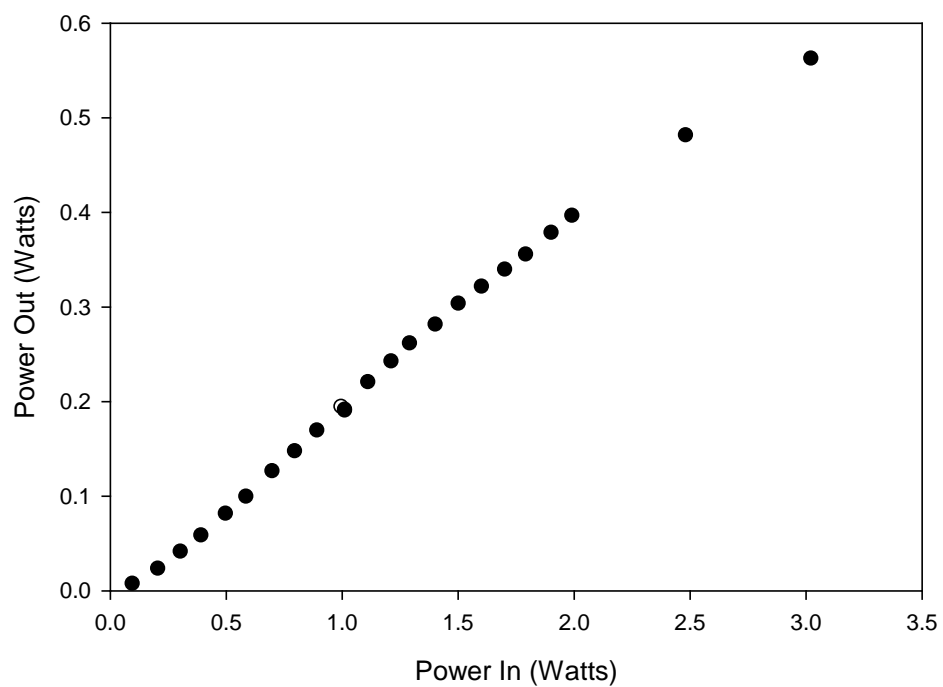
**Figure 69.** $P_{ethane} = 600$ **Torr,** $R_{OC} = 20\%$**,** $T = 100^\text{o}\text{C}$
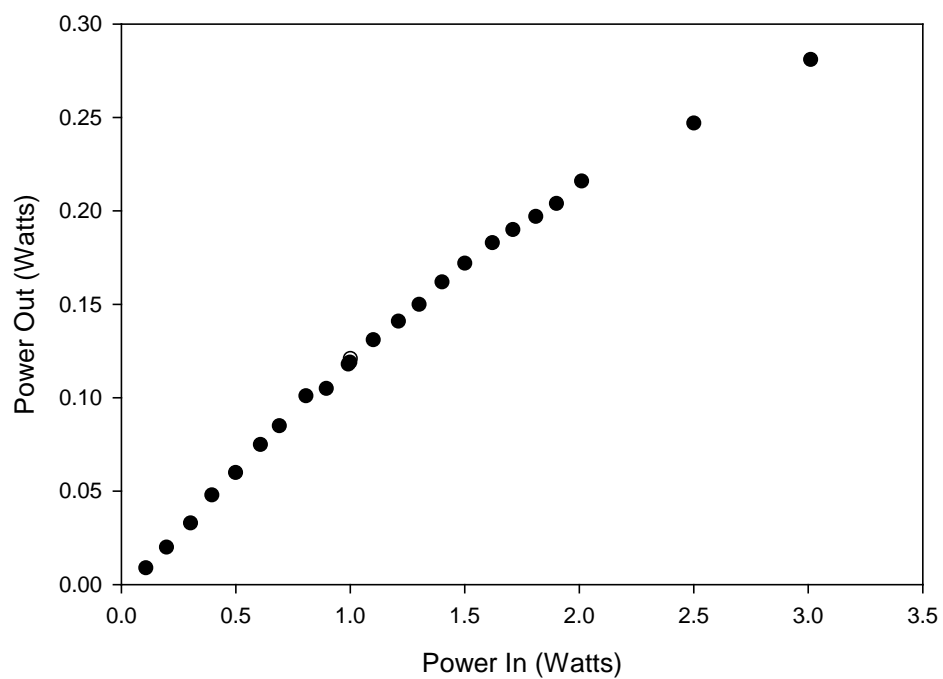


**Figure 70.** $P_{ethane} = 600$ **Torr,** $R_{OC} = 20\%$**,** $T = 90^\text{o}\text{C}$
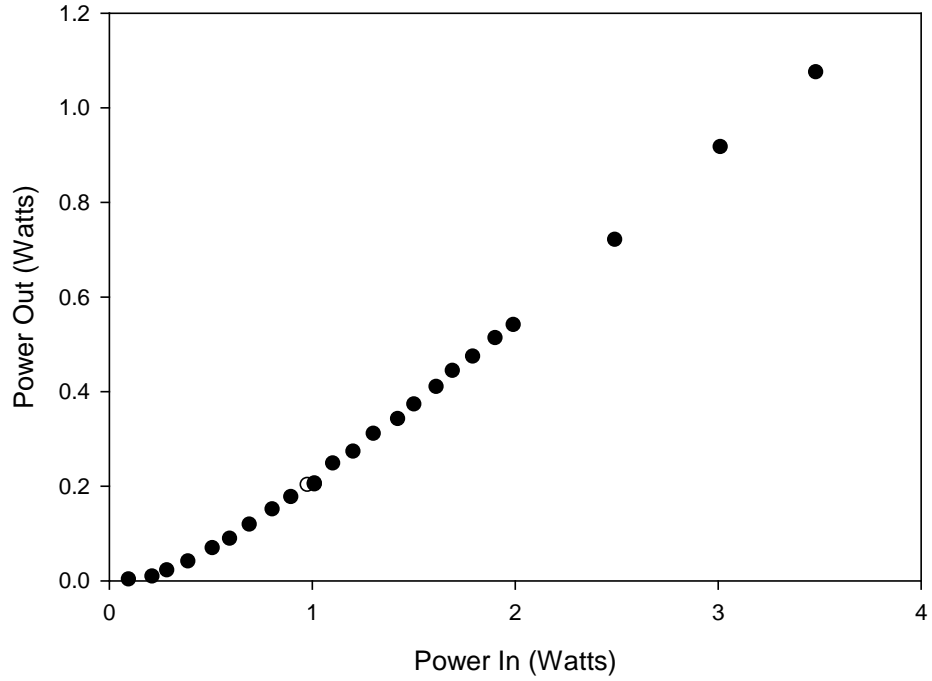
**Figure 71.** $P_{ethane} = 300$ Torr, $P_{He} = 200$ Torr, $R_{OC} = 20\%$, $T = 120^{o}$C
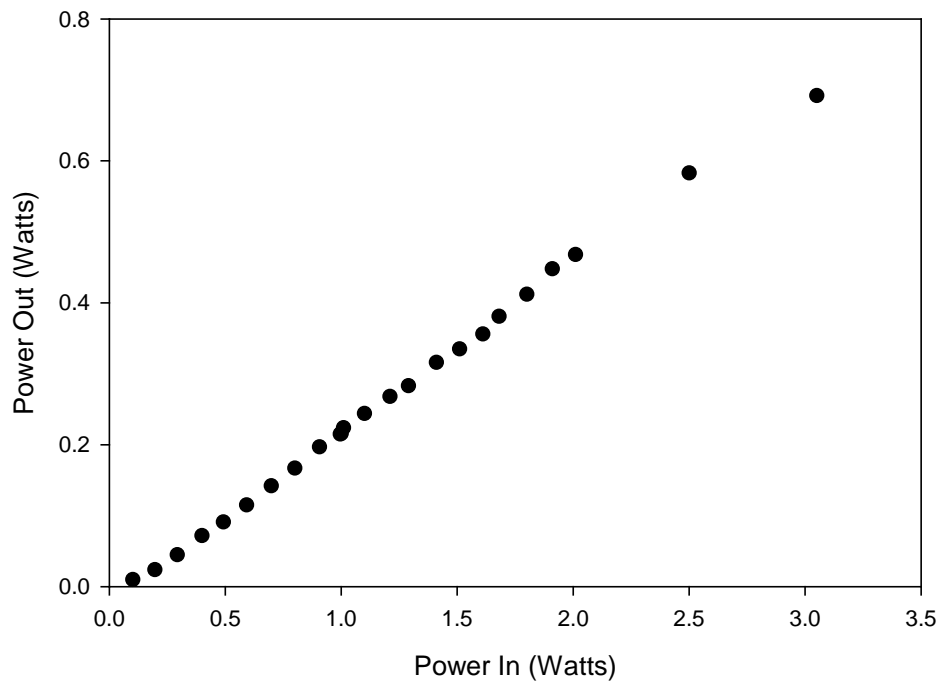


**Figure 72.** $P_{ethane} = 300$ Torr, $P_{He} = 200$ Torr, $R_{OC} = 20\%$, $T = 100^{o}$C

103
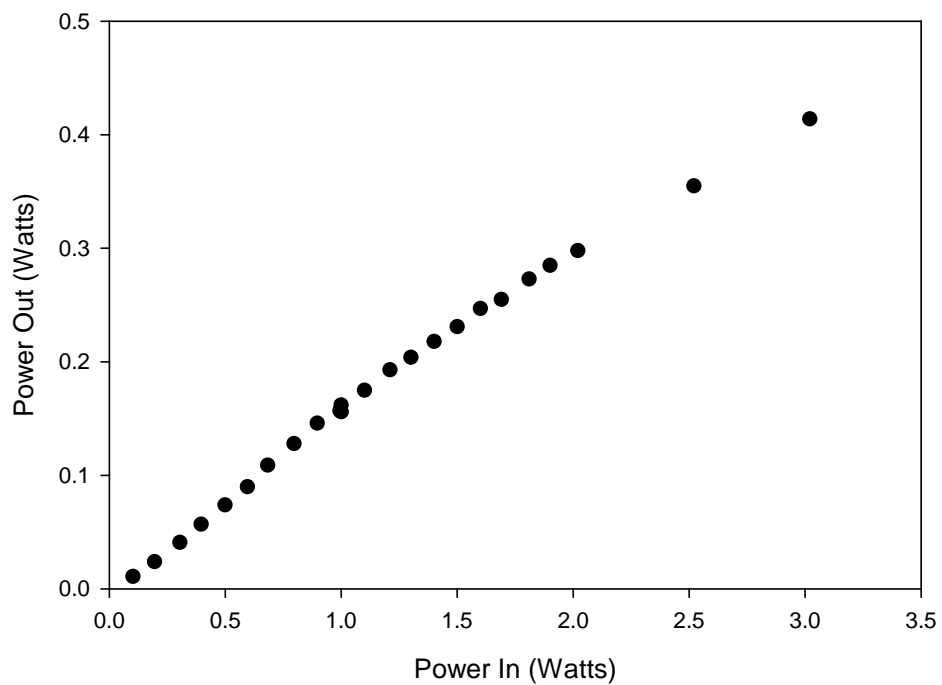
**Figure 73.** $P_{ethane}$ = 300 Torr, $P_{He}$ = 200 Torr, $R_{OC}$ = 20%, $T$ = 90$^{o}$C



**Figure 74.** $P_{ethane}$ = 450 Torr, $P_{He}$ = 200 Torr, $R_{OC}$ = 20%, $T$ = 120$^{o}$C
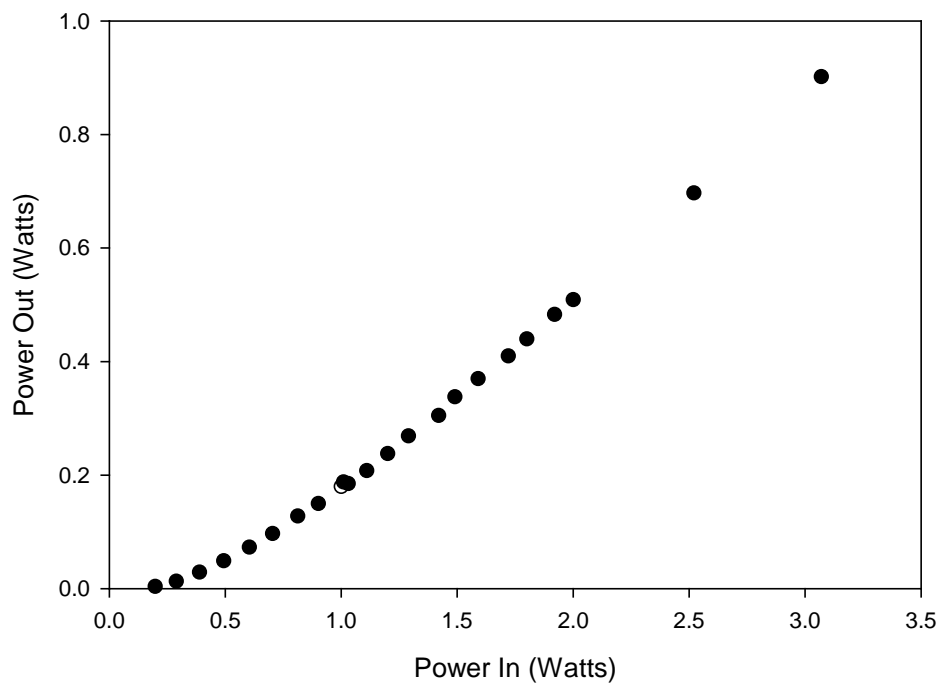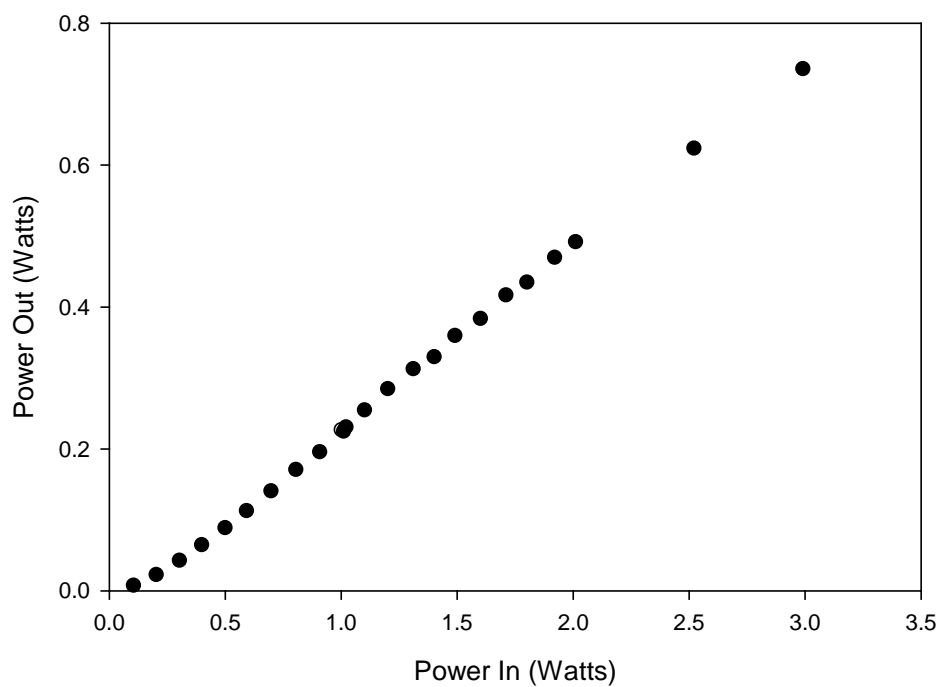
**Figure 75.** $P_{ethane}$ = 450 Torr, $P_{He}$ = 200 Torr, $R_{OC}$ = 20%, $T$ = 100$^o$C
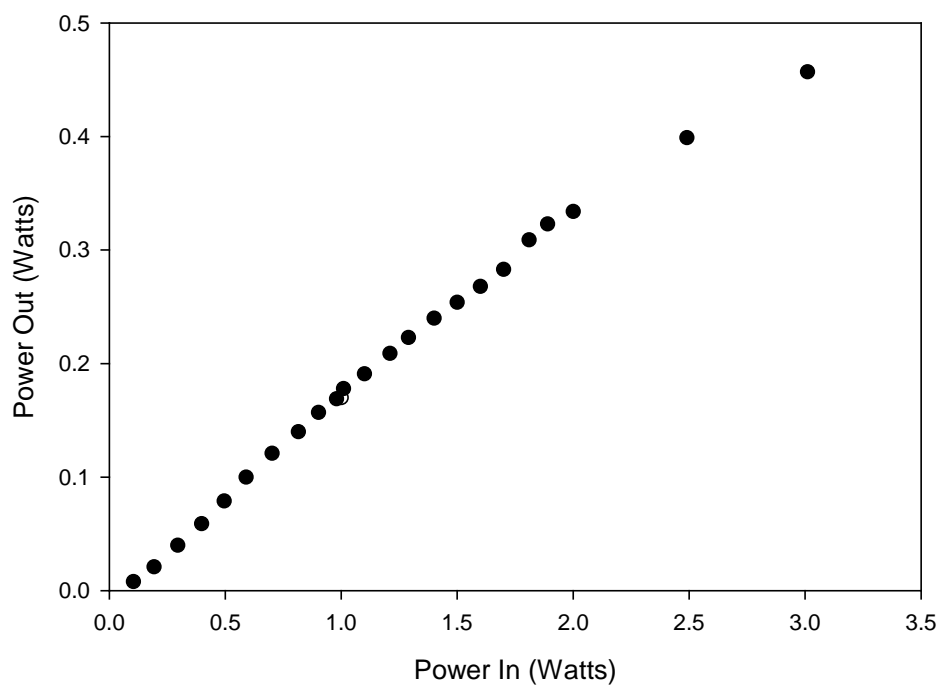


**Figure 76.** $P_{ethane}$ = 450 Torr, $P_{He}$ = 200 Torr, $R_{OC}$ = 20%, $T$ = 90$^o$C

**Appendix B.  Laser Performance Dependence on Pump Repetition Rate**

The repetition rate of the pump laser was varied during the course of this research to explore the possibility that the gain volume was being locally heated during the pump pulse.  While Figure 77 appears to demonstrate a dependence of output pulse energy on the repetition rate, there is not a dependence.  In fact, as the repetition rate is increased, the pump pulses become temporally stretched and grow to as much as 150 ns in time, compared to the initial 100 ns.  And since the energy per pulse remains constant, the peak power achieved during each pulse is less, resulting in a lower energy per pulse out. Essentially, the pulse spends a greater amount of time operating in the wings, where efficiency is lower than at the peak of the pulse.  This deviation must be accounted for in any pulsed system to ensure that accurate slope efficiencies are determined.
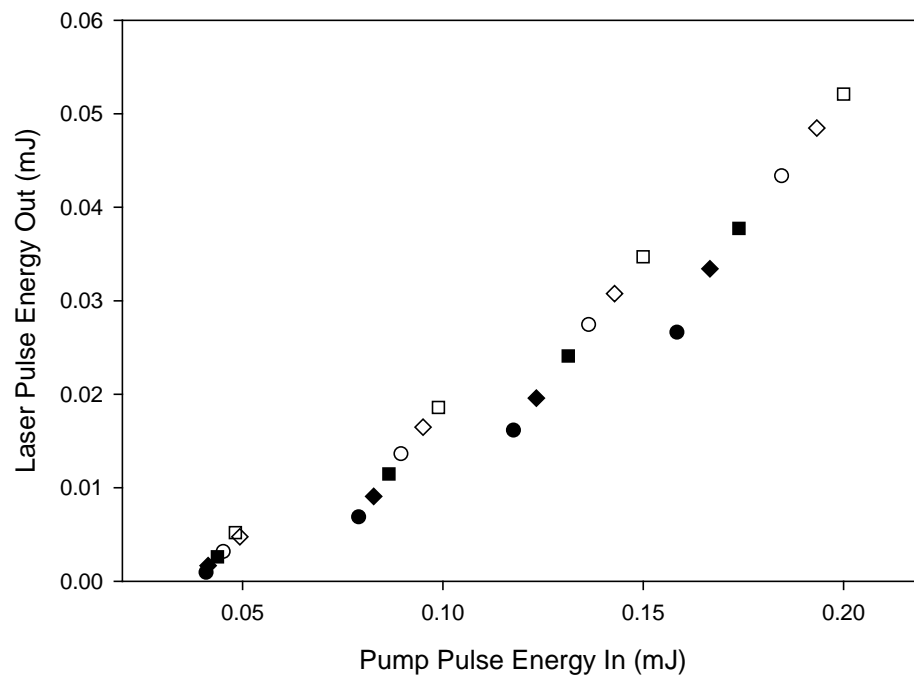
**Figure 77. Rubidium laser performance with repetition rates of (●)12.5 kHz, (♦)12.0 kHz, (⬚)11.5 kHz, (○)11.0 kHz, (⬚)10.5 kHz, and (⬚)10.0 kHz**

# Bibliography

1.  Akulshin, A., R. McLean, A. Sidorov and P. Hannaford, "Coherent and collimated blue light generated by four-wave mixing in Rb vapour," *Optics Express*, 17: 22861 (2009).

2.  Alcock, C.B., V.P. Itkin, and M.K. Horrigan, "Vapour Pressure Equations for the Metallic Elements: 298-2500 K," *Canadian Metallurgical Quarterly*, 23: 309 (1984).

3.  Barbier, L., and M. Cheret, "Energy pooling process in rubidium vapour," *Journal of Applied Physics B, Atomic and Molecular Physics*, 16: 3213 (1983).

4.  Beach, R., W. Krupke, V. Kanz, and S. Payne, "Diode-Pumped Alkali Atom Lasers," *Lawrence Livermore Technical Report*, UCRL-TR-210223 (2005).

5.  Beach, R., W. Krupke, V. Kanz, S. Payne, M. Dubinskii, and L. Merkle, "End-pumped continuous-wave alkali vapor lasers: experiment, model, and power scaling," *Journal of the Optical Society of America B*, 21: 2151 (2004).

6.  Collins, C., K. Bonin, and M. Kadar-Kallen, "*Absolute two-photon cross section of Rb measured by differential absorption*," Optics Letters, 18: 1754 (1993).

7.  Ehrenreich, T., B.V. Zhdanov, T. Takekoshi, S.P. Phipps, and R.J. Knize, "Diode pumped caesium laser," *Electronic Letters*, 41: 415 (2005).

8.  Hager, G.D., and G.P. Perram, "Extended saturation analysis and analytical model of diode-pumped alkali lasers," *SPIE High Energy/Average Power lasers and Intense Beam Applications Conference*, 7581: 75810J-1 (2010).

9.  Hager, G.D., and G.P. Perram, "A three-level analytic model for alkali metal vapor lasers: part I. Narrowband optical pumping," *Applied Physics B*, (2010) DOI 10.1007/s00340-010-4050-6.

10. Jabbour, Z.J., R.K. Namiotka, J. Huennekens, M. Allegrini, S. Milosevic, and F. de Tomasi, "Energy-pooling collisions in cesium: $6P_J + 6PJ \rightarrow 6S + (nl = 7P, 6D, 8S, 4F)$," *Physical Review A*, 54: 1372 (1996).

11. Krupke, W., R. Beach, V. Kanz, and S. Payne, "Resonance transition 795-nm rubidium laser," *Optics Letters*, 28: 2336 (2003).

12. Lane, R.J., A.B. Petersen, and J. Gloyd, "CW 795 nm Rb Vapor Laser Pumped by Volume Transmission Grating-Stabilized Diode Bar," Conference on Lasers and Electro-Optics, Baltimore Maryland, May 6 (2007).

13. Marinescu, M., V. Florescu, and A. Dalgarno, "*Two-photon excitation of the 5 $^2$D states of rubidium*," Physical Review A, 49: 2714 (1993).

14. McGrory, W., "High-Fidelity Physics Based Modeling of Static and Flowing DPAL Gain Media," *2010 Diode Pumped Alkali Laser and Electrically Pumped Gas Phase Laser Workshop*, KAFB, NM (2010).

15. Meijer, T., J. White, B. Smeets, M. Jeppesen, and R. Scholten, "Blue five-level frequency-upconversion system in rubidium," *Optics Letters*, 31: 1002 (2006).

16. Page, R., R. Beach, V. Kanz, and W. Krupke, "*Multimode-diode-pumped gas (alkali-vapor) laser,*" Optics Letters, 31: 353 (2006).

17. Parrington, J.R., H.D. Knox, S.L. Breneman, E.M. Baum, and F. Feiner, *Nuclides and Isotopes fifteenth edition, Chart of the Nuclides*. G.E. Nuclear Energy, California, 1996.

18. Perschbacher, T.A., D.A. Hostutler, and T.M. Shay, "High-efficiency diode-pumped rubidium laser: experimental results," *SPIE International Symposium on Gas Flow, Chemical Lasers, and High-Power Lasers*, 6346 634607-1 (2006).

19. Pitz, G.A., and G.P. Perram, "Pressure Broadening of the D1 and D2 lines in Diode Pumped Alkali Lasers," *Proceedings of SPIE*, 7005: 700526-1 (2008).

20. Pitz, G.A., C.V. Sulham, P. Jones, E.A. Acosta, and G.P. Perram, " Accepted: AIAA Plasmadynamics and Lasers Conference (2010).

21. Risk, W., T. Gosnell, and A. Nurmikko, *Compact Blue-Green Lasers*. Cambridge University Press, Cambridge, 2003.

22. Rotondaro, M.D., and G.P. Perram, "Collisional Broadening and Shift of the Rubidium $D_1$ and $D_2$ Lines ($5^2S_{1/2}$ ⟶ $5^2P_{1/2}$, $5^2P_{3/2}$) by Rare Gases, $H_2$, $D_2$, $N_2$, $CH_4$, and $CF_4$," *Journal of Quantum Spectroscopy and Radiation Transfer*, 57: 497 (1997).

23. Rotondaro, M.D., and G.P. Perram, "Role of rotational-energy defect in collisional transfer between 5 $^2P_{1/2,3/2}$ levels in rubidium" *Physical Review A*, 57: 4045 (1998).

24. Schultz, J., S. Abend, D. Doring, J. Debs, P. Altin, J. White, N. Robins, and J. Close, "Coherent 455 nm beam production in a cesium vapor," *Optics Letters*, 34: 2321 (2009).

25. Sharma, A., N. Bhaskar, Y. Lu, and W. Happer, "Continuous-wave mirrorless lasing in optically pumped atomic Cs and Rb vapors," *Applied Physics Letters*, 39: 209 (1981).

26. Sitnikov, M., N. Znamenskii, E. Manykin, E. Petrenk, and G. Grigoryan, "Stimulated IR emission in an optically pumped cesium vapour," *Quantum Electronics*, 30: 221 (2000).

27. Steck, D.A., "Rubidium 87 D Line Data," available online at http://steck.us/alkalidata (revision 2.0.1, 2 May 2008).

28. Steck, D.A., "Cesium D Line Data," available online at http://steck.us/alkalidata (revision 2.1.2, 12 August 2009).

29. Sulham, C.V., G.A. Pitz, and G.P. Perram, "Blue and infrared stimulated emission from alkali vapors pumped through two-photon absorption," *Applied Physics B*, (2010) DOI 10.1007/s00340-010-4015-9 .

30. Sulham, C.V., G.P. Perram, M.P. Wilkinson, and D.A. Hostutler, "A pulsed, optically-pumped rubidium laser at high pump intensity," *Optics Communications*, (2010) DOI: 10.1016/j.optcom.2010.06.038.

31. Theodosiou, C., " Lifetimes of alkali-metal-atom Rydberg states," *Physical Review A*, 30: 2881 (1984).

32. Wang, Z.-G., L.-J. Qin, L.-S. Ma, Y.-Q. Lin and I.-S. Cheng, "Two-photon hybrid resonance laser and photodissociation laser by two-photon pumping covering a wide wavelength region in the potassium vapor," *Optics Communications*, 51: 155 (1984).

33. Wang, Y., M. Niigaki, H. Fukuoka, Y. Zheng, H. Miyajima, S. Matsuoka, H. Kubomura, T. Hiruma, and H. Kan, "Approaches of output improvement for a cesium vapor laser pumped by a volume-Bragg-grating coupled laser-diode-array," Physics Letters A, 360: 659 (2007).

34. Wang, Y., T. Kasamatsu, Y. Zheng, H. Miyajima, H. Fukuoka, S. Matsuoka, M. Niigaki, H. Kubomura, T. Hiruma, and H. Kan, "Cesium vapor laser pumped by a volume-Bragg-grating coupled quasi-continuous-wave laser-diode array," Applied Physics Letters, 88: 141112 (2006).

35. Webster, J.G., Wiley. *Encyclopedia of Electrical and Electronics Engineering*. John Wiley and Sons, Inc., New York, 1999.

36. Wu, S.S.Q., T.F. Soules, R.H. Page, S.C. Mitchell, V.K. Kanz, and R.J. Beach, "*Resonance transition 795-nm rubidium laser using $^3$He buffer gas*," Optics Communications, 281: 1222 (2008).

37. Wu, S.S.Q., T.F. Soules, R.H. Page, S.C. Mitchell, V.K. Kanz, and R.J. Beach, "*Hydrocarbon-free resonance transition 795-nm rubidium laser*," Optics Letters, 32: 2423 (2007).

38. Zameroski, N.D., G.D. Hager, W. Rudolph, C.J. Erickson, and D.A. Hostutler, "Pressure Broadening and Collisional Shift of the Rb D2 Absorption Line by $CH_4$, $C_2H_6$, $C_3H_8$, $N-C_4H_{10}$, and He," *Submitted to J. Quant. Spectrosc. Radiat. Transfer*, submitted 7 May 2010.

39. Zapka, W., M. Levenson, F. Schellenberg, A. Tam, and G. Bjorklund, "*Continuous-wave Doppler-free two-photon frequency-modulation spectroscopy in Rb vapor*," Optics Letters, 8: 27 (1982).

40. Zhdanov, B., J. Sell, and R. Knize, "Multiple laser diode array pumped Cs laser with 48W output power," *Electronic Letters*, 44: 582 (2008).

41. Zhdanov, B., A. Stooke, G. Boyadjian, A. Voci, and R. Knize, "Rubidium vapor laser pumped by two laser diode arrays," *Optics Letters*, 33: 414 (2008).

42. Zhdanov, B.V., T. Ehrenreich, R.J. Knize, "Highly efficient optically pumped cesium vapor laser," *Optics Communications*, 260: 696 (2006).

43. Zhdanov, B.V., C. Maes, T. Ehrenreich, A. Havko, N. Koval, T. Meeker, B. Worker, B. Flusche, R.J. Knize, "Optically pumped potassium laser," *Optics Communications*, 270: 353 (2007).

44. Zhdanov, B.V., and R.J. Knize, "Hydrocarbon-Free Potassium Laser," *Electronic Letters*, 43: 1024 (2007).

45. Zhdanov, B.V., and R.J. Knize, "Diode-pumped 10 W continuous wave cesium laser," *Optics Letters*, 32: 2167 (2007).

46. Zhdanov, B.V., A. Stooke, G. Boyadjian, A. Voci, and R.J. Knize, "Laser diode array pumped continuous wave Rubidium vapor laser," *Optics Express*, 16: 748 (2008).

47. Zheng, Y., M. Niigaki, H. Miyajima, T. Hiruma, and H. Kan, "Hight-Efficiency 894-nm Laser Emission of Laser-Diode-Bar-Pumped Cesium-Vapor-Laser," *Applied Physics Express*, 2: 032501 (2009).

48. Zhu, Q., B. Pan, L. Chen, Y. Wang, and X. Zhang, "Analysis of temperature distributions in diode-pumped alkali vapor lasers," *Optics Communications*, 283: 2406 (2010).

49. Zhu, Q., J. Yu, W. Zheng, and H. Quan, "Operating Temperatue of Diode-pumped Alkali Vapor Laser," *Proceedings of SPIE*, 6823: 68230O-1 (2007).

50. Zibrov, A., M. Lukin, L. Hollberg, and M. Scully, "Efficient frequency up-conversion in resonant coherent media," *Physical Review A*, 65: 051801 (2002).

51. Zibrov, A., M. Lukin, D. Nikonov, L. Hollberg, M. Scully, V. Velichansky, and H. Robinson, " Experimental Demonstration of Laser Oscillation without Population Inversion via Quantum Interference in Rb," *Physical Review Letters*, 75: 1499 (1995).

52. Zweiback, J., and W.F. Krupke, "28W Average Power Hydrocarbon-Free Diode Pumped Alkali Laser," *Optics Express*, 18: 1444 (2010).

53. Zweiback, J., A. Komashko, and W.F. Krupke, "Alkali Vapor Lasers," *SPIE High Energy/Average Power Lasers and Intense Beam Applications Conference*," 7581: 75810G-1(2010).

54. Zweiback, J., G.D. Hager, and W.F. Krupke, "High efficiency hydrocarbon-free resonance transition potassium laser," *Optics Communications*, 282: 1871 (2009).

# REPORT DOCUMENTATION PAGE

| 1. REPORT DATE *(DD-MM-YYYY)*<br>10-09-2010 | 2. REPORT TYPE<br>Doctoral Dissertation | 3. DATES COVERED *(From – To)*<br>Sept 2007 – Sept 2010 |
|---|---|---|

| TITLE AND SUBTITLE<br><br>Laser Demonstration and Performance Characterization of an Optically Pumped Alkali Laser System | 5a. CONTRACT NUMBER |
|---|---|
| | 5b. GRANT NUMBER |
| | 5c. PROGRAM ELEMENT NUMBER |

| 6. AUTHOR(S)<br><br>Sulham, Clifford V., Major, USAF | 5d. PROJECT NUMBER |
|---|---|
| | 5e. TASK NUMBER |
| | 5f. WORK UNIT NUMBER |

| 7. PERFORMING ORGANIZATION NAMES(S) AND ADDRESS(S)<br>Air Force Institute of Technology<br>Graduate School of Engineering and Management (AFIT/ENP)<br>2950 Hobson Way, Building 640<br>WPAFB OH 45433-8865 | 8. PERFORMING ORGANIZATION REPORT NUMBER<br><br>AFIT/DS/ENP/10-S06 |
|---|---|

| 9. SPONSORING/MONITORING AGENCY NAME(S) AND ADDRESS(ES)<br>High Energy Laser – Joint Technology Office / Ackermann, H.<br>901 University Blvd S.E. Suite 100<br>Albuquerque, NM 87106 | 10. SPONSOR/MONITOR'S ACRONYM(S)<br>HEL-JTO |
|---|---|
| | 11. SPONSOR/MONITOR'S REPORT NUMBER(S) |

**12. DISTRIBUTION/AVAILABILITY STATEMENT**
APPROVED FOR PUBLIC RELEASE; DISTRIBUTION UNLIMITED.

**13. SUPPLEMENTARY NOTES**

**14. ABSTRACT**
Diode Pumped Alkali Lasers (DPALs) offer a promising approach for high power lasers in military applications that won't suffer from the long logistical trails of chemical lasers or the thermal management issues of diode pumped solid state lasers. This research focuses on characterizing a DPAL type system to gain a better understanding of using this type of laser as a directed energy weapon. A rubidium laser operating at 795nm is optically pumped by a pulsed titanium sapphire laser to investigate the dynamics of DPALs at pump intensities between 1.3 and 45 kW/cm$^2$. Linear scaling as high as 32 times threshold is observed, with no evidence of second order kinetics. Comparison of laser characteristics with a quasi-two level analytic model suggests performance near the ideal steady-state limit, with the exception of mode matching. Additionally, the peak power has scaled linearly as high as 1 kW, suggesting aperature scaling to a few cm$^2$ is sufficient to achieve tactical level laser powers. The temporal dynamics of the 100ns pump and rubidium laser pulses are presented, and the continually evolving laser efficiency provides insight into the bottlenecking of the rubidium atoms in the $^2P_{3/2}$ state. Lastly, multiple excited states of rubidium and cesium were accessed through two photon absorption in the red, and yielded a blue and an IR photon through amplified stimulated emission. Threshold is modest at 0.3mJ/pulse, and slope efficiencies increase dramatically with alkali concentrations and peak at 0.4%, with considerable opportunity for improvement. This versatile system might find applications for IR countermeasures or underwater communications.

**15. SUBJECT TERMS**
Diode pumped alkali laser, rubidium laser, two photon absorption

| 16. SECURITY CLASSIFICATION OF: | | | 17. LIMITATION OF ABSTRACT | 18. NUMBER OF PAGES | 19a. NAME OF RESPONSIBLE PERSON<br>Perram, Glen P., Professor, ADVISOR |
|---|---|---|---|---|---|
| a. REPORT | b. ABSTRACT | c. THIS PAGE | UU | 127 | 19b. TELEPHONE NUMBER *(Include area code)*<br>(937) 255-6565, ext 4504<br>(glen.perram@afit.edu) |
| U | U | U | | | |